Mon. Not. R. Astron. Soc. **000**, 000–000 (0000) Printed 16 March 2010 (MN LATEX style file v2.2)

A joint analysis of BLAST 250–500 μm and LABOCA 870 μm observations in the Extended Chandra Deep Field South

Edward L. Chapin[1⋆], Scott C. Chapman[2], Kristen E. Coppin[3], Mark J. Devlin[4], James S. Dunlop[5], Thomas R. Greve[6,7], Mark Halpern[1], Matthew F. Hasselfied[1], David H. Hughes[8], Rob J. Ivison[9,5], Gaelen Marsden[1], Lorenzo Moncelsi[10], Calvin B. Netterfield[11,12], Enzo Pascale[10], Douglas Scott[1], Ian Smail[3], Marco Viero[11], Fabian Walter[6], Axel Weiss[13], Paul van der Werf[14]

[1] *Dept. of Physics & Astronomy, University of British Columbia, 6224 Agricultural Road, Vancouver, B.C. V6T 1Z1, Canada*
[2] *Institute of Astronomy, University of Cambridge, Madingley Road, Cambridge CB3 0HA, UK*
[3] *Institute for Computational Cosmology, Durham University, South Road, Durham DH1 3LE, UK*
[4] *Department of Physics and Astronomy, University of Pennsylvania, 209 South 33rd Street, Philadelphia, PA 19104, USA*
[5] *SUPA† Institute for Astronomy, University of Edinburgh, Royal Observatory, Blackford Hill, Edinburgh, EH9 3HJ, UK*
[6] *Max-Planck Institute für Astronomie, Königstuhl 17 D-69117, Heidelberg, Germany*
[7] *Dark Cosmology Centre, Niels Bohr Institute, University of Copenhagen, Juliane Maries Vej 30, DK-2100 Copenhagen, Denmark*
[8] *Instituto Nacional de Astrofísica, Óptica y Electrónica (INAOE), Aptdo. Postal 51 y 216, Puebla, Mexico*
[9] *UK Astronomy Technology Centre, Royal Observatory, Blackford Hill, Edinburgh, EH9 3HJ, UK*
[10] *School of Physics & Astronomy, Cardiff University, 5 The Parade, Cardiff, CF24 3AA, UK*
[11] *Department of Astronomy & Astrophysics, University of Toronto, 50 St. George Street Toronto, ON M5S 3H4, Canada*
[12] *Department of Physics, University of Toronto, 60 St. George Street, Toronto, ON M5S 1A7, Canada*
[13] *Max-Planck-Institut für Radioastronomie, Auf dem Hügel 69, Bonn, D-53121, Germany*
[14] *Leiden Observatory, Leiden University, PO Box 9513, NL-2300 RA Leiden, the Netherlands*

16 March 2010

ABSTRACT

We present a joint analysis of the overlapping BLAST 250, 350, 500 μm, and LABOCA 870 μm observations (from the LESS survey) of the Extended Chandra Deep Field South. Out to $z \sim 3$, the BLAST filters sample near the peak wavelength of thermal far-infrared (FIR) emission from galaxies (rest-frame wavelengths $\sim$ 60–200 μm), primarily produced by dust heated through absorption in star-forming clouds. However, identifying counterparts to individual BLAST sources is very challenging, given the large beams (FWHM 36–60 arcsec). In contrast, the ground-based 870 μm observations have a significantly smaller 19 arcsec FWHM beam, and are sensitive to higher-redshifts ($z \sim$ 1–5, and potentially beyond) due to the more favourable negative K-correction. In this study we use the LESS data, as well as deep *Spitzer* and VLA imaging, to identify 125 individual sources that produce significant emission in the BLAST bands. We characterize the temperatures and FIR luminosities for a subset of 73 sources with well-measured submm SEDs and redshift measurements out to $z \sim 3$. Considering flux-limited sub-samples in each BLAST band, and a dust emissivity index $\beta = 2.0$, we find a median temperature $T = 30$ K (all bands) as well as median redshifts: $z = 1.1$ (interquartile range 0.2–1.9) for $S_{250} > 40$ mJy; $z = 1.3$ (interquartile range 0.6–2.1) for $S_{350} > 30$ mJy; and $z = 1.6$ (interquartile range 1.2–2.3) for $S_{500} > 20$ mJy. Taking into account the selection effects for our survey (a bias toward detecting lower-temperature galaxies), we find no evidence for evolution in the local FIR-temperature correlation out to $z \sim 2.5$. Comparing with star-forming galaxy SED templates, about 8% of our sample appears to exhibit significant excesses in the radio and/or mid-IR, consistent with those sources harbouring an AGN. Since our statistical approach differs from most previous studies of submm galaxies, we describe the following techniques in two appendices: our 'matched filter' for identifying sources in the presence of point-source confusion; and our approach for identifying counterparts using likelihood ratios. This study is a direct precursor to future joint far-infrared/submm surveys, for which we outline a potential identification and SED measurement strategy.

1 INTRODUCTION

Observations in the submillimetre (submm) wavelength band (defined here to be 200–1000 μm) are ideal for detecting light from massive star-forming galaxies out to cosmological distances. It has been known since the all-sky *Infrared Astronomical Satellite (IRAS)* survey of the 1980's that such sources contain significant amounts of dust, so that the ultra-violet (UV) light of newly-formed stars is absorbed by the galaxies' interstellar medium (ISM) (Sanders & Mirabel 1996). The dust is typically heated to tens of Kelvin, and most of the light is then thermally re-radiated at far-infrared (FIR) wavelengths (∼60–200 μm). In the submm, the thermal spectral energy distribution (SED) drops off steeply, so that there is a progressively stronger negative K-correction with increasing observing wavelength. The correction is so strong that near ∼1 mm the observed flux density for a galaxy of fixed luminosity is approximately constant from $1 \lesssim z \lesssim 10$ (Blain et al. 2002).

Even though much of the submm band is obscured to ground-based observations by atmospheric water vapour, a number of surveys over the last decade have exploited transparency in several spectral windows to successfully locate high-redshift ($z > 1$) dusty star-forming galaxies solely through their submm emission (submillimetre galaxies, or SMGs henceforth). Their discovery was first made with the Submillimetre Common User Bolometer Array (SCUBA Holland et al. 1999) at 850 μm (e.g., Smail et al. 1997; Hughes et al. 1998; Barger et al. 1998; Cowie et al. 2002; Scott et al. 2002; Borys et al. 2003; Webb et al. 2003; Coppin et al. 2006). Several other instruments confirmed their existence in the slightly more transparent 1.1–1.2 mm band (e.g., Greve et al. 2004; Laurent et al. 2005; Scott et al. 2008; Perera et al. 2008; Austermann et al. 2010). Existing ground-based surveys at 850–1200 μm typically cover $\ll 1\,\mathrm{deg}^2$, and detect several tens of sources per field. The typical angular resolution of these surveys is in the range ∼9–20 arcsec full-width at half-maximum (FWHM). It is worth noting that observations at 350 and 450 μm have also been attempted from the ground (e.g., Smail et al. 1997; Hughes et al. 1998; Fox et al. 2002; Kovács et al. 2006; Khan et al. 2007; Coppin et al. 2008). However, this wavelength range is much more difficult, due to increased atmospheric opacity, so that these first surveys have only detected a handful of sources.

While the first generation surveys successfully demonstrated the existence of these ultra-luminous infrared galaxies (ULIRGs) at $z \sim 1.5$–4 (e.g Chapman et al. 2003; Aretxaga et al. 2003; Chapman et al. 2005), sample sizes have been modest (typically $\ll 100$ sources in a given field), making more detailed studies difficult. Most of what is known about SMGs is based on cross-identifications with sources in higher-resolution data, particularly in the radio (primarily 1.4 GHz Very Large Array maps, e.g., Smail et al. 2000; Ivison et al. 2007) and in the mid-IR (such as 24 μm *Spitzer* maps, e.g., Ivison et al. 2004; Pope et al. 2006). While these counterpart identification strategies could be biased toward lower-redshifts due to the *positive* K-corrections in the radio/mid-IR, more observationally time-consuming mm-wavelength interferometric observations (e.g., Lutz et al. 2001; Dannerbauer et al. 2004; Iono et al. 2006; Younger et al. 2007) demonstrate reasonable correspondence with proposed radio/mid-IR counterparts for a handful of sources. With accurate positions it is then possible to identify optical counterparts, although they are usually extremely faint due to obscuration by the same dust that makes them bright in the submm–FIR, and the fact that stellar light from the most distant objects gets red-shifted out of the optical bands into the near-IR. For these reasons, even the deepest *HST* imaging does not always detect the counterparts to SMGs. Obviously, ground-based optical spectroscopy is even more challenging given the difficulty in imaging the counterparts.

Recent observations by the 1.8-m Balloon-borne Large Aperture Submillimeter Telescope (BLAST) at 250, 350, 500 μm (a pathfinder for *Herschel*/SPIRE, Pascale et al. 2008) toward the Extended Chandra Deep Field South (ECDF-S) have provided the first confusion-limited submm maps at these wavelengths which cover areas larger than $1\,\mathrm{deg}^2$. These bands were chosen to bracket the peak rest-frame FIR emission from the SMG population at $z \sim 1$–4. However, given the size of its primary mirror, the BLAST diffraction-limited angular resolution of 36–60 arcsec FWHM at 250–500 μm has made associations between submm emission peaks and individual sources at other wavelengths even more challenging than with the ground-based surveys. Regardless, initial comparisons with mid-IR and radio data have yielded useful preliminary results. A joint analysis of bright BLAST sources detected in any of the 3 bands (including identifications and SEDs) is described in Dye et al. (2009). Pushing to fainter flux densities in GOODS-S, Dunlop et al. (2009) identified counterparts and measured the redshift distribution of sources in the deepest 250 μm data. A slightly shallower 250 μm catalogue covering the entire ECDF-S was used to measure evolution in the FIR-radio correlation in Ivison et al. (2009). In broad terms, these studies demonstrate that the sources detected at 250–500 μm by BLAST are a much more heterogeneous collection than galaxy samples selected in most ground-based submm surveys, ranging from local L_* galaxies up to $z \sim 3$ ULIRGs. In addition, the FIR-radio correlation appears to hold for the 250 μm sample, consistent with the luminosity in these galaxies being dominated by star-formation rather than buried AGN.

Despite the difficulty in finding *individual* sources that produce the submm emission detected with BLAST, the bulk properties of other galaxy populations have been successfully studied using stacking analyses (Devlin et al. 2009; Marsden et al. 2009; Pascale et al. 2009; Ivison et al. 2009). In particular, a precise measurement of how the redshift distribution of sources contributing to the total CIB varies at wavelengths across its peak has now been made: within the *COBE* uncertainties, the bulk of Cosmic Infrared Background (CIB Puget et al. 1996; Fixsen et al. 1998) at 250–500 μm is produced by galaxies already detected at 24 μm, with a clear trend toward higher redshifts at longer wavelengths. These results are consistent with the general trend observed in shorter-wavelength *Spitzer* (e.g., Dole et al. 2006) and longer-wavelength SCUBA (e.g., Pope 2007; Serjeant et al. 2008; Marsden et al. 2009) CIB measurements.

In addition to deep BLAST observations of the ECDF-S, there also exists the deepest and wide-area submm map at ∼1 mm to date: the LABOCA ECDFS Submm Sur-

vey (LESS) at 870 μm (Weiss et al. 2009), taken with the 12 m APEX telescope (Güsten et al. 2006). Like SCUBA, LABOCA (Siringo et al. 2009) is more sensitive to $z > 1$ sources than BLAST, and the most distant sources ($z > 4$, e.g., Coppin et al. 2009) are expected to be LABOCA-detected BLAST-dropouts. In addition, the LABOCA beam has a 19 arcsec FWHM (roughly half that of the 250 μm BLAST beam). In this paper we combine the LESS and BLAST data to achieve the best possible astrometry, and hence increase the multi-wavelength identification rate, and to constrain the Rayleigh-Jeans spectrum. This enables us to push to the faintest flux densities in all three BLAST bands. LESS-detected BLAST-dropouts are examined in a companion paper, Coppin et al. (submitted). These combined BLAST and LABOCA studies may be thought of as a precursor to future *Herschel*, SCUBA-2, and Large Millimeter Telescope (LMT) overlapping surveys that will cover considerably larger areas with superior angular resolution (although their success will depend on radio and mid-IR data of comparable areas and depths that do not presently exist). While not discussed here, we also note that another continuum map of GOODS-S was recently made at 1.1 mm (Scott et al. 2010).

The submm data, as well as the radio and infrared catalogues with which we identify counterparts, are presented in Section 2. We draw the reader's attention to the detailed Appendix A that describes our new method for identifying submm sources in the noisy / point-source confused maps. The results of cross-matching the submm sources with the external catalogues using Likelihood Ratios (LR) are summarized in Section 3. The full derivation of our LR expression and measurements of priors are presented in Appendix B. The observed-frame spectral energy distributions (SEDs) for our sample are presented in Section 4. Combining these observations with redshifts from the literature, we conduct the most complete measurements of the rest-frame luminosities and dust temperatures of BLAST-selected galaxies to date in Section 5.

2 DATA

2.1 Submillimetre Data

2.1.1 BLAST

In 2006 BLAST conducted a two-tiered nested survey centred over the Great Observatories Origins Deep Surveys South (GOODS-S): BLAST GOODS-South Wide (BGS-Wide) over 10 $\deg^2$ to instrumental RMS depths 36, 31 and 20 mJy, at 250, 350 and 500 μm, respectively; and BLAST GOODS-South Deep (BGS-Deep) over 0.9 $\deg^2$ to RMS depths 11, 9 and 6 mJy. It is important to note that a significant additional contribution to the noise in these maps is produced by point source confusion, estimated to be 21, 17 and 15 mJy in the three bands (Marsden et al. 2009). The ECDF-S is completely encompassed by the BGS-Deep coverage. The BLAST maps were produced using SANEPIC (Patanchon et al. 2008), and were filtered to suppress residual noise on scales larger than approximately 10 arcmin (the array footprint). The BLAST beams have FWHM 36, 42, and 60 arcsec at 250, 350, and 500 μm.

Sources were identified in the maps by cross-correlating with the effective point spread functions (PSFs; combining the diffraction pattern with the large-scale noise suppression filter) and identifying peaks. This procedure improves the signal-to-noise ratio (SNR), but degrades the resolution by approximately $\sqrt{2}$ with respect to the diffraction limit. The maps and data reduction are discussed in detail in Devlin et al. (2009). Details on instrument performance and calibration are provided in Pascale et al. (2008); Truch et al. (2009).

2.1.2 LESS

The LABOCA Survey of the Extended Chandra Deep Field South (LESS, Weiss et al. 2009) provides deep 870 μm data, with an RMS better than 1.2 mJy across the full 30 arcmin × 30 arcmin ECDFS. A combination of time-domain filtering of the raw bolometer data, as well as the suppression of residual noise on scales $\gtrsim$ 90 arcsec were incorporated as part of the reduction procedure. Similar to the BLAST data, this map was then smoothed with the 19 arcsec FWHM diffraction-limited PSF to identify 125 point sources in Weiss et al. (2009) above a significance of 3.72σ (equivalent to a false detection rate of $< 5\%$).

2.1.3 Submm Catalogues

It is standard practice in the submm community to find sources in maps by cross-correlating with the PSF, as noted in the previous sections. This operation is optimal for the case of an isolated point source in a field of statistically uncorrelated noise: the cross-correlation gives the maximum-likelihood flux density of a point source fit to every position in the map.[1]

The BLAST data lie in a regime where the approximately white instrumental noise, $N_{\rm w}$, is about a factor of two smaller than confusion noise, $N_{\rm c}$. The LESS data are not as confused, with the two noise components being roughly equal.[2] Since this confusion is a source of noise that is *correlated on the scale of the PSF*, we have investigated a modified filter for identifying sources. If one imagines the extreme opposite case of that used to motivate cross-correlation with the PSF – that there is no instrumental noise in the image whatsoever, and so the only signal is the confused pattern of many overlapping sources, clearly any additional smoothing will only make matters worse. In this extreme case, one must clearly bin the data into a finely-sampled grid and simply identify peaks without any filtering that might further degrade the resolution — or alternatively attempt to *de*-convolve the PSF.

We approach this problem by developing a 'matched filter' that maximizes the SNR of individual point sources in the presence of noise. The resulting filter in each band can be thought of as an optimal balance between smoothing and de-convolving the PSF, depending on the relative strengths of the white and confusion noise components. We

[1] This procedure has long been understood in astronomical data analysis in other wavebands, e.g., Stetson (1987).

[2] For BLAST the ratios of confusion RMS to instrumental noise in the PSF-smoothed maps are 1.9, 1.9, and 2.4 at 250, 350, and 500 μm. For the LESS PSF-smoothed map the ratio is 1.15.

cross-correlate the raw submm maps with these new filters, and produce source lists from peaks in the resulting SNR maps. A detailed description of our matched filter is given in Appendix A, with Fig. A1 comparing the matched filter with the PSF at 500 micron.

How much does this filter improve the SNR at each wavelength? To address this question we turn to simulations, drawing point source flux densities from the best-fit number counts in each band (from Patanchon et al. (2009) and Weiss et al. (2009) for BLAST and LESS respectively), distributing them uniformly in maps, smoothing the maps with the respective PSFs, adding instrumental white noise to match the levels reported for the real observations, and finally subtracting the map means. We then compare the relative sizes of confusion ($\sigma_{\rm c}$), white ($\sigma_{\rm w}$) and combined ($\sigma_{\rm t} \equiv \sqrt{\sigma_{\rm c}^2 + \sigma_{\rm w}^2}$) noise components in: (i) the raw unsmoothed maps; (ii) maps smoothed by the PSFs; and (iii) maps smoothed by the matched filters. The results are summarized in Table 1, and in Fig. 1 a sample portion of the ECDF-S is compared in all four submm bands with no filtering, matched filtering, and PSF filtering.

We find that the point-source sensitivities in the match-filtered BLAST maps improve by ∼15–20% over those reported for the PSF smoothed maps in Devlin et al. (2009) (comparing the bold-face $\sigma_{\rm t}$ columns for the PSF and Matched Filter in Table 1). However, the increase in the LESS point-source sensitivities, ∼ 5%, is not as significant due to the relatively smaller contribution of confusion. Given this marginal improvement, and for the sake of simplicity, we do not produce a new 870 μm source list for our analysis.

We use the full 870 μm LESS source list from Weiss et al. (2009) (down to a SNR of 3.72σ), and then construct new 3.75σ source lists for BLAST (relative to instrumental noise) from the match-filtered maps (all submm catalogues are provided in Appendix C).[3] Thresholds in this range typically result in false-identification rates of order 5% (e.g., Coppin et al. 2006; Perera et al. 2008; Weiss et al. 2009) for other submm surveys. However, since the BLAST data are considerably more confused than these aforementioned surveys, we have used the simulated maps described above to determine whether this threshold is reasonable.

First, we identify individual sources in the simulated maps above 3.75σ using the same matched filter. Given the sizes of the BLAST beams, and the surface density of the sources, *every* location in the filtered maps has a contribution from multiple submm galaxies (even if they are extremely faint). For each 3.75σ peak we therefore identified *the single* source that makes the *largest* contribution to the observed flux density from the input catalogue at that location — considering the PSFs in each band, input source brightnesses and their distances from the peaks in the filtered maps. We find that these brightest sources statistically contribute fractions $0.73^{+0.57}_{-0.57}$, $0.57^{+0.56}_{-0.22}$, and $0.58^{+0.65}_{-0.25}$ (means and 95% confidence intervals) of the flux densities in the filtered maps at 250, 350 and 500 μm. Note that the fraction can be greater than one since the simulation is noisy (the source may have landed on a large positive noise excursion). This test shows us that, using a 3.75σ cut, *most* of the observed flux density in a submm peak is probably produced by a single source, and the *smallest* contribution by a single bright source is about 25%.

Finally, we investigate the completeness using this simple simulation, counting the number of sources above different flux limits in the input catalogue that are recovered in the match-filtered source list (again, considering only the single brightest submm galaxies that contribute to the observed brightness). The recovered percentages are: 50% above 30 mJy, and 90% above 60 mJy at 250 μm; 50% above 15 mJy, and 90% above 45 mJy at 350 μm; and 50% above 10 mJy, and 90% above 25 mJy at 500 μm.

[3] The new BLAST GOODS-S match-filtered maps and source lists are available at `http://blastexperiment.info/`.

2.2 Matching Catalogue

We have produced a matching catalogue that is a subset of the IRAC data from SIMPLE (*Spitzer* IRAC/MUSYC Public Legacy in ECDF-S Gawiser et al. 2006), containing only the sources that exhibit either mid-IR or radio emission (two wavelength regimes that have typically been used to identify submm sources in the past). The coverage of this catalogue in relation to the submm maps is shown in Fig. 2. There are a total of 9216 entries covering 703 arcmin^2, a surface density of 13.1 arcmin^{-2}. There are 8833 sources detected at 24 μm, 1659 at 1.4 GHz, and 1276 at both 24 μm and 1.4 GHz. The next two sections describe the mid-IR and radio data in more detail.

2.2.1 FIDEL

A deep MIPS 24 and 70 μm catalogue was produced by Magnelli et al. (2009), combining *Spitzer* data from GOODS-S with the Far-Infrared Deep Extragalactic Legacy survey (FIDEL, P.I. Mark Dickinson). The PSFs have FWHM 5.5 arcsec and 16 arcsec, in each band respectively. The catalogue uses SIMPLE as a positional prior enabling de-blending of sources down to separations as small as 0.5 times the MIPS FWHM. This catalogue is the same that was used for other recent BLAST studies in ECDF-S (Devlin et al. 2009; Dye et al. 2009; Marsden et al. 2009; Pascale et al. 2009), as well as in the LESS identification paper (Biggs et al. submitted).

2.2.2 Radio

The VLA 1.4 GHz data are from the survey of Miller et al. (2008). Given the low elevation of this southern field, and observing from the VLA in the north, the synthesized beam is significantly elongated with dimensions 2.8 arcsec × 1.7 arcsec. We use a new radio catalogue produced by Biggs et al. (submitted) that was developed to identify counterparts to LESS sources. An initial catalogue of 3σ peaks in the map is produced, and then Gaussians are fit at each of those positions, allowing the sizes to vary. Since this fit is particularly noisy at the faint end, we cull sources with integrated flux densities that are less significant than 2σ. Finally, we only include sources that lie within 2 arcsec of the IRAC positions. This strategy enables us to go significantly deeper than the published 7σ catalogue from Miller et al. (2008), or the 5σ catalogue from Dye et al. (2009), at the expense of

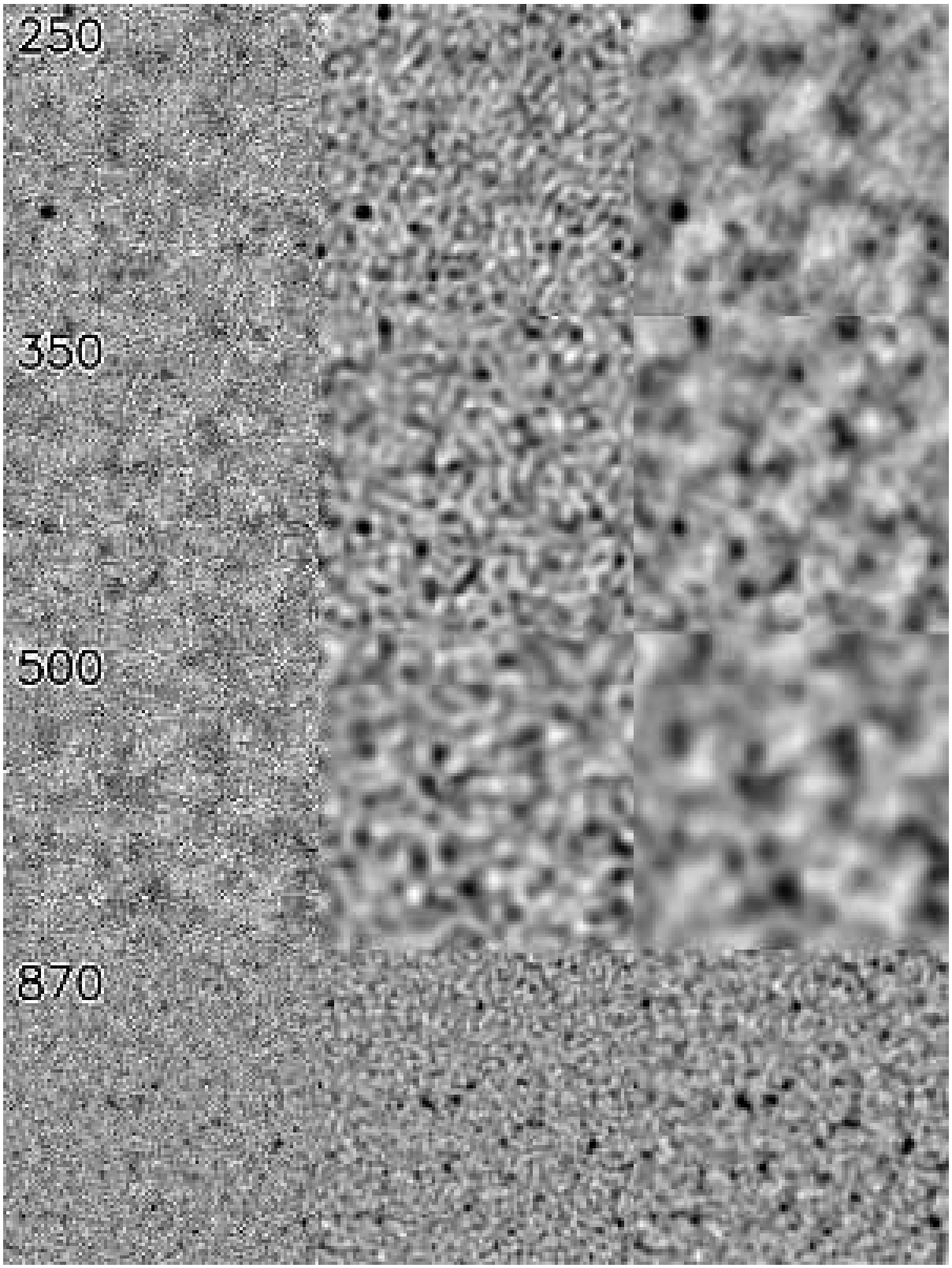

Figure 1. Comparison of maps at all four wavelengths (rows), and smoothing scales in a 0.3 deg × 0.3 deg patch of the ECDF-S. The first column shows un-smoothed maps (noisy, but diffraction-limited resolution), the second column maps smoothed by the matched filter (greatly improved SNR at the expense of a slight degradation in the resolution), and the last column maps smoothed by the PSF (less improvement in the SNR, and resolution degraded by $\sqrt{2}$). The greyscales indicate the significance of point-source flux densities in the maps, ranging from $-3\,\sigma$ (white) to $+4\,\sigma$ (black), considering both the instrumental and confusion noise contributions to each pixel (estimated from simulations – see boldface values in Table 1).

Table 1. Comparison of confusion (σ_c), white (σ_w) and total (σ_t) noise contributions in the raw submm maps, maps cross-correlated with the full PSF, and maps cross-correlated with the matched filter which compensates for confusion. Each quantity was estimated using simulations based on un-clustered realizations of sources drawn from the measured number counts distributions of Patanchon et al. (2009) and Weiss et al. (2009), for BLAST and LESS respectively. All noise values are standard deviations in mJy. Note that our definition of confusion noise here is simply the RMS of a noise-free map containing point sources only. This calculation shows that white noise is more effectively suppressed by PSF filtering than matched filtering. However, the confusion noise is significantly larger in the PSF filtered map than the match filtered map. For this reason the *total* noise in the match filtered maps is smaller.

λ	Raw			PSF			Matched Filter		
(μm)	σ_c	σ_w	σ_t	σ_c	σ_w	σ_t	σ_c	σ_w	σ_t
250	14.5	31.2	**34.4**	21.9	11.5	**24.7**	14.6	13.8	**20.1**
350	12.5	28.5	**31.1**	17.3	8.90	**19.5**	13.0	10.7	**16.8**
500	11.6	27.4	**29.8**	16.1	6.70	**17.4**	11.7	8.30	**14.3**
870	0.70	2.00	**2.12**	0.97	0.84	**1.28**	0.82	0.90	**1.22**

missing a handful of brighter radio sources that do not appear to have IRAC associations. Since Monte Carlo simulations based on the submm data and matching catalogue are used in the following section to calculate the probability that individual counterparts are real, any spurious radio sources near the detection threshold will simply reduce the identification efficiency (see also Fig. B3). Finally, we note that Biggs et al. (submitted) also find identifications for LESS sources using a combination of the radio, MIPS, and IRAC catalogues, although the IRAC data are not explicitly used as a prior for the radio positions.

3 CROSS-IDENTIFICATIONS

Given the poor positional uncertainties inherent to the current generation of submillimetre waveband surveys (typically several arcsec), there are usually many potential optical counterparts for each SMG. Hence it has usually been necessary to search for identifications in lower surface density catalogues at radio and mid-IR wavelengths. The method usually adopted is to estimate 'P' chance alignment probabilities (Downes et al. 1986) in order to exclude the least likely candidates (although this does not provide a probability that a given source 'is *the* counterpart'). This calculation only uses the source counts of the matching catalogue and an empirically derived maximum search radius. The expected distribution of offsets for true matches is *not* used, except perhaps to set the search radius.

In this paper we take a different approach, using a 'likelihood ratio' (LR) formalism. The basic idea attempts to answer the following question: given a potential counterpart to the submm source, what is the relative likelihood that it could be a real counterpart given its measured properties (e.g., radial offset, flux density, colour etc.), versus the probability that it is a chance interloper (given the background source counts as a function of measured properties)? Versions of this technique have been used in a variety of contexts (e.g., Sutherland & Saunders 1992; Mann et al. 1997; Rutledge et al. 2000). Clearly the LR can explicitly use information such as the expected positional uncertainties, whereas the P calculation does not (although the maximum search radius implicitly incorporates some of this information). It should be noted that in the past colour-based priors have also been used to cull matching catalogues, and hence reduce the surface density of spurious sources, before finding counterparts using P statistics (e.g Pope et al. 2006; Yun et al. 2008, Biggs et al. submitted). By itself the LR can still only be used to *rank* potential counterparts (similar to the problem with P statistics), but we develop a technique to establish both the false identification rates, and identification completeness rates for given absolute LR thresholds in each band.

It appears that the reason the LR formalism has not been used for submm identification work in the past is due to its reliance on prior information which historically has been extremely difficult to estimate (see discussion in Serjeant et al. 2003; Clements et al. 2004). With individual surveys covering $\ll 1\,\mathrm{deg}^2$ and having typically fewer than several tens of sources per field, and very low SNR, the precise positional uncertainty distribution is unknown. However, the BLAST and LESS data, combined with the deep radio and *Spitzer* mid-IR data covering the ECDF-S, enable estimates of priors (such as the radial offset distribution of counterparts) with sufficient precision to produce useful results. Forthcoming *Herschel*, SCUBA-2, and LMT surveys will have better angular resolution, depth, and cover substantially larger areas, so that the methods employed here will also be fruitful (although these future surveys will depend on radio and mid/near-IR data of comparable area and depth for identifying counterparts, and they do not presently exist).

As described in Section 2 we have produced a matching catalogue based on sources from SIMPLE (IRAC) that exhibit either mid-infrared (*Spitzer* MIPS photometry from FIDEL), or VLA 1.4 GHz emission. For the purpose of identifying counterparts we have focussed on three features of this catalogue in addition to positions: 24 μm and 1.4 GHz flux densities (when available) — both of which have commonly been used in the calculation of P values; and the $c \equiv [3.6]-[4.5]$ IRAC colour (all sources), which is sensitive to redshift (e.g., Simpson & Eisenhardt 1999; Sawicki 2002; Pope et al. 2006; Yun et al. 2008; Devlin et al. 2009) as it traces the peak of the rest-frame stellar bump.

We fully develop the LR formulae and priors in Appendix B, but provide the main results here. Given the flux densities s (at 24 μm and 1.4 GHz in this case), the IRAC colour c, and the distance r to the jth matching catalogue source from the ith submm source for which we are searching

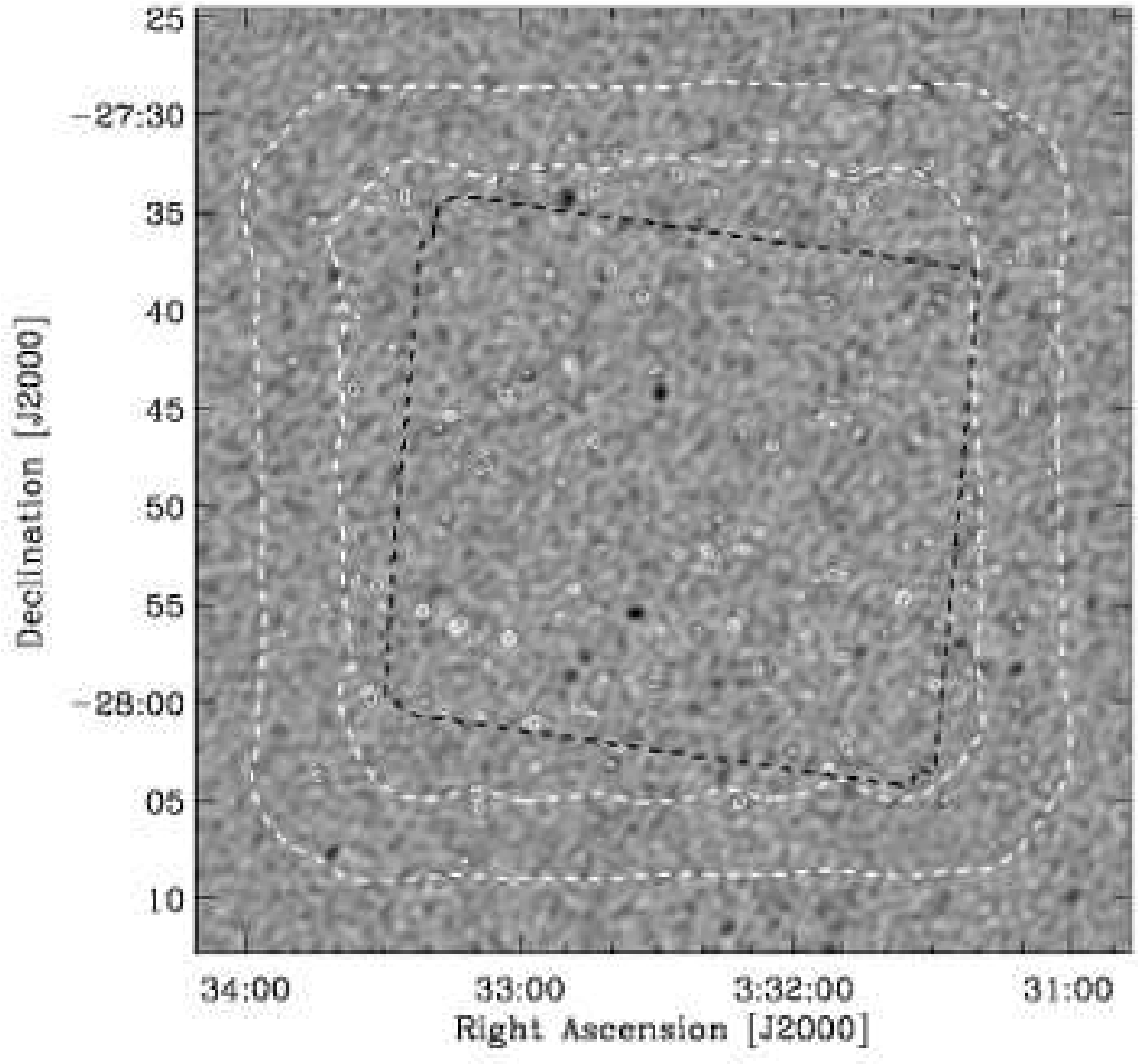

Figure 2. Relative coverage of data sets in ECDF-S. The background greyscale image shows the BLAST 250 μm match-filtered SNR map (this field is completely encompassed by the BGS-deep region described in Devlin et al. 2009), scaled between $-10\,\sigma$ (white) and $+13\,\sigma$ (black). The solid white contours show the LESS SNR map at levels 3, 6 and $10\,\sigma$. The white dashed lines show the LESS 1.3 and 2.2 mJy instrumental noise contours. The dashed black line indicates the 708 arcmin^2 region common to the VLA and FIDEL survey coverage within which we perform out counterpart search. The ECDF-S presently has the best (widest and deepest) submm coverage from 250–870 μm on the sky, with the mid/far-IR and radio data of matching quality required to identify counterparts.

for a counterpart, we calculate the LR:

$$L_{i,j} = \frac{q(s_j, c_j) e^{-r_{i,j}^2/2\sigma^2}}{2\pi\sigma^2 \rho(s_j, c_j)}. \quad (1)$$

Here σ characterizes a radially-symmetric Gaussian positional uncertainty, $q(s, c)$ is the prior distribution for flux densities and colours of matches to submm sources, and $\rho(s, c)$ is the background source distribution.

All of the priors, σ, $q(s, c)$ and $\rho(s, c)$, have been estimated directly from the data by counting sources in the matching catalogue as a function of each property around submm source positions (of order ∼60 in each submm band), and comparing to the counts for the entire matching catalogue over the full survey area. We believe this procedure yields a high-SNR measurement of the positional uncertainties, since we need only bin measurements for the submm sources (in each band) along one coordinate, r, which we then fit with a simple one-parameter model. However, there is an implicit assumption that the sources (both in the submm and matching catalogues) are spatially un-clustered.

Ideally we would bin $q(s, c)$ and $\rho(s, c)$ along all three axes simultaneously (two flux densities and a colour), but in practice this is not feasible given the numbers of submm sources that we have to work with. We therefore handle the priors *independently*, e.g., estimating $q(s, c) \simeq q(s_{24})q(s_{\rm r})q(c)$, and $\rho(s, c) \simeq \rho(s_{24})\rho(s_{\rm r})\rho(c)$. This assump-

tion certainly introduces a bias, since in practice these properties are correlated (for example, see Fig. 7 in Dye et al. 2009, showing the correlation between 24 μm and 1.4 GHz flux densities for counterparts to bright BLAST sources). We have chosen to compensate for this bias by using Monte Carlo simulations to estimate a threshold in the LR that produces a false identification rate of 10%. We establish this level by choosing 10,000 random positions in the field, and calculating the LR of matching catalogue sources around those positions. In each submm band we choose a threshold in LR that rejects 90% of the matched sources from this random sample. We then calculate normalized LRs for counterparts to submm sources in each band by dividing the LR from Eq. 1 by these thresholds. Potential counterparts to submm sources are considered to be those objects in the matching catalogue for which the normalized LR is greater than 1.

In summary, while our assumption that the flux densities and colour are independent of one another is probably incorrect, we have established a cut on LR that will restrict the number of false positive identifications in the matching catalogue to around 10% (with respect to the number of submm sources). This idea of setting a threshold to reject background sources is similar to adopting a cut on P, although here we have included more prior information to improve the efficiency. However, we warn the reader that the calibration of the LR and P are both tied to our assumption that clustering in the matching catalogue around submm positions is a negligible effect.

3.1 Potential Counterparts

The main results of our identification statistics are given in Table 2. A striking feature of our analysis is that we have found that, on average, each submm position appears to be associated with *several* sources in the matching catalogue (see details in Section B1, in which we fit both an amplitude and radial uncertainty distribution for the offsets of counterparts). This excess could either be interpreted as evidence for source confusion, or simply that many sources from the matching catalogue tend to cluster around the submm sources. We prefer the former explanation since the excess is correlated with beam size, increasing from 2.2 at 870 μm (19 arcsec FWHM beam) to 3.7 at 500 μm (60 arcsec FWHM beam). If the excess were purely produced by extra (non-submm–emitting) galaxies clustered around the submm sources, we would expect the same total excess regardless of the resolution of the observations (although with poorer resolution the excess sources would of course be more spread-out).

For comparison, we have also identified potential counterparts using P statistics based on the 24 μm and 1.4 GHz flux densities. We counted the numbers of IDs with $P < 0.1$ using both of these sub-catalogues around random positions (as a control, similar to the method employed to normalize the LR), and around submm positions (similar to Fig. 3 in Chapin et al. 2009). We discovered that, while the radio catalogue was well-behaved (a 10% false ID rate was obtained for random positions), we obtained too many false IDs with the 24 μm catalogue. This result is probably demonstrating that the 24 μm catalogue is slightly clustered. We therefore tuned the cut on P_{24} to 0.08 to obtain the desired 10% rate using random positions. The search radii that we used were $1.5\sigma_{\rm r}$ (from Table 2); these search radii are roughly comparable to those adopted in previous studies of BLAST sources (Dye et al. 2009; Ivison et al. 2009; Dunlop et al. 2009), and encompass approximately 68% of the true counterparts inferred from the excess counting statistics. Using $P_{24} < 0.08$ we would find 45, 31, 12 and 33 potential counterparts, and using $P_{\rm r} < 0.10$ we would find 51, 35, 17 and 44, at 250, 350, 500, and 870 μm, respectively. Comparing with the 'Found IDs' column for Table 2 we see that there is a significant (although modest) improvement using our LR calculation over P statistics, particularly at the longer wavelengths where the $[3.6]-[4.5]$ IRAC colour is a good discriminator of redshift.

As our goal is to study the properties of BLAST-selected sources, we identify all of the unique sources from our matching catalogue that potentially produce the observed 250, 350 and 500 μm emission. We then search the LESS catalogue for extra sources that are within the 3σ search radius of *any* 3.75σ BLAST (combining both the BLAST and LABOCA positional uncertainties in quadrature). Any additional identifications from the matching catalogue to these improved LESS positions are added to the master list. In total, 125 sources from the matching catalogue are identified as potential sources of the BLAST emission.

A list of all the matching catalogue entries and the submm sources to which they were matched is given in Table C5 and postage stamps showing the locations of the matches in relation to the submm positions are shown in Fig. D1. For each ID, in addition to the LR, we also provide P values for matches to the 24 μm and 1.4 GHz radio catalogues, using search radii $1.5\sigma_{\rm r}$ (see Table 2). Note that Tables C1–C4, which provide the source submm positions in each band, also give the identifications from the matching catalogue, counting all sources within a 3σ search radius around the submm positions matched to *any* band. Unlike Table 2, which gives identification statistics considering each band independently, we now see how the simultaneous observations in the four submm bands have helped one another: 78%, 78%, 82%, and 83% of the 250, 350, 500, and 870 μm sources have at least one potential counterpart identified. In many cases the same source appears in several bands, and the higher-resolution observations have enabled counterpart identifications where the lower-resolution observations failed.

4 SUBMILLIMETRE SPECTRAL ENERGY DISTRIBUTIONS

In this section we re-measure the submm flux densities from the combined list (i.e., selected in *any* BLAST band) at the positions of their proposed counterparts. We then fit these observed-frame SEDs with simple isothermal models, and measure the observed number counts in our catalogue as a function of limiting flux density. Together, these calculations allow us to explore bias and completeness effects for our sample.

Table 2. Excess count and ID statistics. The detected number of sources are from the BLAST and LESS catalogues, using 3.75σ and 3.72σ thresholds, respectively. The excess counts per source and σ_r are the best-fit positional uncertainty model parameters (with χ^2_r giving the reduced chi-squared in each case) – see Section B1. The fact that the excesses are greater than 1 is an indication of how confused the data are, and a warning that finding single counterparts is challenging. Expected numbers of IDs are calculated from the product of the number of submm sources with the average excesses per source. 'Found IDs' are the total number of potential counterparts with false-identification rates of 10% in the matching catalogue. The 'Real ID' rate subtracts the expected number of false IDs for the list (10% of the number of submm sources; see discussion of threshold LR values in Section 3), and also expresses that quantity as a percentage of the total expected.

λ (μm)	Sources (#)	Excess (per source)	σ_r (arcsec)	χ^2_r	Expected IDs (#)	Found IDs (#)	Real IDs (#)
250	64	3.2	10.4	1.8	204.8	52	45.6 (22%)
350	67	3.4	10.4	1.5	227.8	50	43.3 (19%)
500	55	3.7	15.4	1.0	203.5	31	25.5 (13%)
870	81†	2.2	6.9	1.8	178.2	66	57.9 (32%)

†There are 81 sources from LESS that land in the region of coverage considered here, but only 48 sources are cross-matched to the BLAST source lists. The full list of 81 sources is used to estimate priors even though we only discuss the properties of the smaller subset of cross-matched sources in this paper. See Coppin et al. (submitted) for the properties of LESS-detected BLAST-dropouts.

4.1 Submm photometry

Under the assumption that the potential counterparts identified in the previous section produce the observed submm emission (and are not simply other galaxies clustered around the submm sources), we return to the four submm maps and perform simultaneous fits of point sources at all 125 locations to measure their flux densities. This procedure is expected to reduce the Eddington-like bias, or *flux-boosting*, inherent to low-SNR submm surveys (Coppin et al. 2005) in two ways. First, since sources are initially selected in three different bands, the component of bias introduced by instrumental noise is reduced (as it is independent in each map) — submm sources preferentially detected on positive noise peaks in one map will not necessarily also land on positive noise peaks in other maps. Second, since we allow for the possibility of *multiple* counterparts to each submm source (a hypothesis confirmed by the excess counting statistics described in Section B1), the simultaneous fit can, to some extent, de-blend some of the brighter confused sources (confusion itself also contributes to Eddington bias, and unlike the instrumental noise, is correlated between the submm bands).

The fit is performed by modeling the emission of the counterparts as the submm PSFs scaled by their unknown submm flux densities S_i at the locations from the matching catalogue. Under the assumption that the instrumental noise in our submm maps is un-correlated from one map pixel to the next (a reasonable assumption for the raw, un-smoothed maps on the scale of the PSF), there is a simple maximum-likelihood solution for the S_i that takes into account the correlations that arise in cases where multiple sources overlap within a PSF footprint — we follow the derivation provided in Appendix A of Scott et al. (2002). However, this approach ignores the additional component of confusion noise from un-resolved sources that is correlated on the scale of the PSF. We therefore add the confusion noise for the simulated raw maps from Table 1 to the variances for each source flux density, $\sigma_i^2 = \mathrm{Cov}(S_i, S_i)$. This operation results in the correct uncertainties for isolated sources, but we warn that it produces an under-estimate of the variances for the most confused sources.

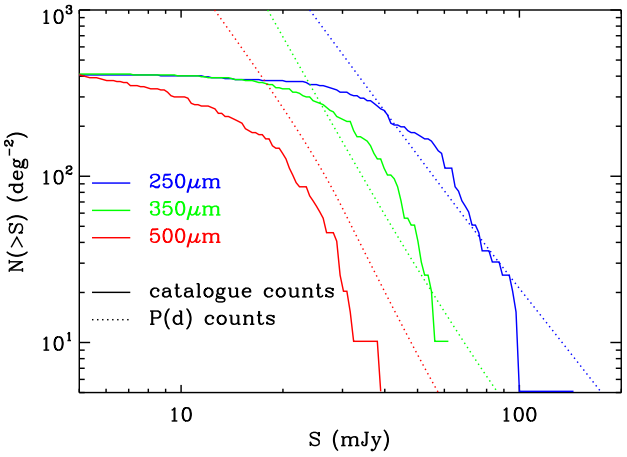

Figure 3. The integral number counts for our sample (solid lines), compared with the total counts inferred from the $P(D)$ analysis of Patanchon et al. (2009) (dotted lines), at 250 (blue), 350 (green) and 500 μm (red).

For isolated sources, the recovered flux density is identical to that obtained from the PSF-smoothed map at the location of its counterpart, and its value is un-correlated with the measured flux densities for all other sources in the map. However, for blended sources, the total flux density in the map is divided among the multiple counterparts, and there are non-negligible covariances $\mathrm{Cov}(S_i, S_j)$ for all sources i, j that lie roughly within a FWHM of each other. We therefore evaluate the full expression for the covariances between measured flux densities, i.e., using the off-diagonals of Eq. A11 in Scott et al. (2002).

The individual observed-frame submm SEDs based on these measurements are given in Table C6. We also display the submm SEDs in Fig. E1, along with the 1.4 GHz, MIPS 24 and 70 μm flux densities (when available), and the photometry from the 3.6, 4.5, 5.8 and 8.0 μm IRAC bands (all sources) from the matching catalogue.

Many of the submm sources appear to be produced by compact clumps of sources from the matching catalogue. We have flagged 42/125 of the most extreme cases with the letter 'C' in Fig. E1 indicating that they are confused to the point that the submm photometry cannot be used reliably, particularly in the BLAST channels. For example, sources 2, 3, 4 and 5 comprise one of the most confused regions of BLAST emission in the entire ECDF-S, as can clearly be seen in the postage stamps (Fig. D1). By comparison, the superior LESS resolution can nearly resolve the entire feature into a string of individual peaks. The inferred flux densities at 250–500 µm therefore have strong *anti-correlations*, since the emission from those four sources must sum to the total integrated flux density of the feature. In fact, the maximum-likelihood solution can even allow negative values, a problem which occurs in a number of the most confused examples. The low SNR of the submm maps combined with confusion from fainter submm sources, and the close proximity of the counterparts, has resulted in flux densities with drastically under-estimated error bars in cases such as sources 2–5. In contrast, sources 64 and 65 are an example where the joint-fit at the positions of two nearby counterparts has recovered plausible flux densities in all the submm bands (this is a low-redshift interacting pair first discussed in Dunlop et al. 2009). In this case, the BLAST SNR is much higher, and the two potential counterparts have sufficient separation to disentangle them.

4.2 Isothermal SED models and number counts

We fit optically-thin isothermal modified blackbody functions (modified blackbodies henceforth), $S_\nu \propto \nu^\beta B_\nu(T)$, to the new submm photometry, and use Monte Carlo simulations to characterize the uncertainties (as described in Section 4 of Chapin et al. 2008). Following the work of Wiebe et al. (2009), who examined the detailed spatially-resolved SEDs of several nearby resolved galaxies observed with BLAST, as well as an earlier study by Klaas et al. (2001) who combined ground-based submm photometry with far-IR measurements of ULIRGs, we choose to model the submm emission using an emissivity index of $\beta = 2.0$. The only free parameters are the amplitudes and temperatures (see Table C6 and Fig. E1).

To test the completeness of our catalogue, and also to gauge the degree to which our procedure has dealt with flux boosting in the submm source catalogues, we compare the integral source counts from our sample (summing the number of sources in the catalogue above a given flux density limit, and dividing by the survey area of 708 arcmin^2) to the total counts inferred from $P(D)$ analysis in Patanchon et al. (2009). Rather than using the submm photometry directly, we use the flux densities from the fitted SED models evaluated in each band. The results of this comparison are shown in Fig. 3. In the 250 and 350 µm channels the catalogue counts slightly exceed the $P(D)$ counts above approximately 30 and 40 mJy, respectively. While this excess shows there is still some influence from boosting, its effect has been drastically reduced when compared with the individual flux-limited BLAST catalogues (see Fig. 11 in Patanchon et al. 2009). Below these levels the catalogue is clearly incomplete at 250 and 350 µm as the counts rapidly flatten. At 500 µm the catalogue counts have a similar qualitative shape, but lie below the $P(D)$ counts at all flux densities; the completeness is about 66% above 20 mJy. This result is expected given the more limited success we have had in identifying counterparts at 500 µm (see Table 2). Note that these approximate completeness estimates are consistent with the simulations described at the end of Section 2.1.3.

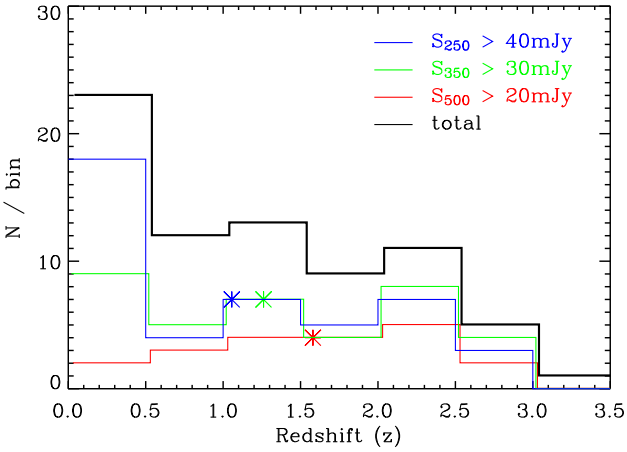

Figure 4. The redshift distribution for the 73 non-confused sources with redshift estimates. Also shown are the redshift distributions for flux-limited sub-samples, $S_{250} > 40$ mJy, $S_{350} > 30$ mJy, and $S_{500} > 20$ mJy, chosen to correspond approximately to where the counts in our catalogues flatten significantly compared to the total population – see Fig. 3. The asterisks indicate the medians of these sub-samples.

5 DISCUSSION

5.1 Redshifts

Many of the proposed counterparts have either optical spectroscopic or photometric redshifts in previously published catalogues (Wolf et al. 2004, 2008; Grazian et al. 2006; Brammer et al. 2008; Rowan-Robinson et al. 2008; Taylor et al. 2009). For those counterparts that do not, the IRAC colours may be used as a crude redshift estimator. We use the redshift catalogue from Pascale et al. (2009) which combines the various photometric and spectroscopic redshfts in the literature with the BLAST redshift survey of Eales et al. (2009), and then we add additional redshifts identified in more recent BLAST follow-up studies (Ivison et al. 2009; Dunlop et al. 2009, Casey et al. in prep). In Fig. E1, the redshifts are indicated with 's', 'p' or 'i', indicating spectroscopic, optical photometric, or IRAC-based photometric redshift measurements, respectively. In total, there are 83/125 sources with usable submm photometry. Of those, 74 have redshift estimates: 23 are optical spectroscopic redshifts; 37 are optical photometric redshifts; and 14 are IRAC photometric redshifts. The full list of redshifts that we have adopted is given in Table C6. We warn that the IRAC-based photometric redshifts are highly uncertain on an object-by-object basis, and are biased low for the higher-redshift ($z > 2$) sources (see Fig. 4 in Pascale et al. 2009).

In Fig. 4 we show the redshift distribution for these 73 sources, as well as sub-samples using flux density-limits in each of the BLAST bands corresponding roughly to the

flux densities at which the counts begin to turn over significantly in Fig. 3 (as a rough proxy for the point at which completeness begins to drop). The median of the entire distribution is $z = 1.1$ with an interquartile range 0.4–1.9. This distribution is qualitatively similar to the deep 250 µm survey of Dunlop et al. (2009) in GOODS-S at the center of the ECDF-S, but shows a significantly greater tail of sources beyond $z = 2$ compared to the shallower survey of Dye et al. (2009). This latter discrepancy is probably due to a combination of increased depth in our submm catalogue, and better completeness in the high-redshift counterpart identifications. Note that if we exclude the the IRAC-based photometric redshifts the median of the entire sample increases slightly to $z = 1.3$.

The flux-limited distributions clearly show a trend from low- to high-redshift with increasing wavelength in Fig. 4: a median $z = 1.1$ with an interquartile range 0.2–1.9 at 250 µm; a median $z = 1.3$ with an interquartile range 0.6–2.1 at 350 µm; and a median $z = 1.6$ with an interquartile range 1.2–2.3 at 500 µm. This trend is consistent with the results from BLAST stacking analyses (Devlin et al. 2009; Marsden et al. 2009; Pascale et al. 2009) which show that the CIB is produced by higher-redshift galaxies with increasing wavelength.

5.2 Rest-frame SEDs

The SEDs for all 125 sources are shown in Fig. E1. For the 73 sources with redshift estimates, we convert the observed temperatures from the modified blackbody fits of Section 4 to rest-frame temperatures, allowing us to probe the cold dust SEDs of the sample. The distributions of these temperatures for the entire sample, and flux-limited sub-samples in each BLAST band are shown in Fig. 5. The total distribution has a median $T = 29$ K and interquartile range 23–36 K. There is almost no variation in the temperatures of the different flux-limited sub-samples: a median $T = 30$ K with an interquartile range 25–40 K at 250 µm; a median $T = 30$ K with an interquartile range 23–38 K at 350 µm; and a median $T = 30$ K with an interquartile range 22–38 K at 500 µm. The reason for this can be seen in the bottom panel of Fig. 5: even though the longer-wavelength channels tend to be biased to selecting higher-redshift (and hence more luminous and warmer) galaxies, the extra galaxies picked up at low-redshift (and hence lower luminosity) by the short-wavelength channels are biased toward warmer temperatures in those volumes. We have also checked for biases in the total temperature distribution due to the IRAC-based photometric redshifts, but do not find a significant difference for the $z > 1.5$ galaxy temperatures when sources with these photometric redshifts are excluded.

We infer cold-dust temperatures that are generally *warmer* than those in Dye et al. (2009), despite using a larger value of $\beta = 2.0$ (compared with 1.5) which might be expected to bias the temperature to *lower* values (for reference, re-running the analysis in this paper with $\beta = 1.5$ increases the temperatures by about 5 K). The reason for this discrepancy is that the 870 µm data have placed a firm constraint on the Rayleigh-Jeans part of the SED. Since the longer-wavelength BLAST data are more confused (and hence more biased), there is a systematic preference for shallower spectra, or cooler apparent temperatures. However,

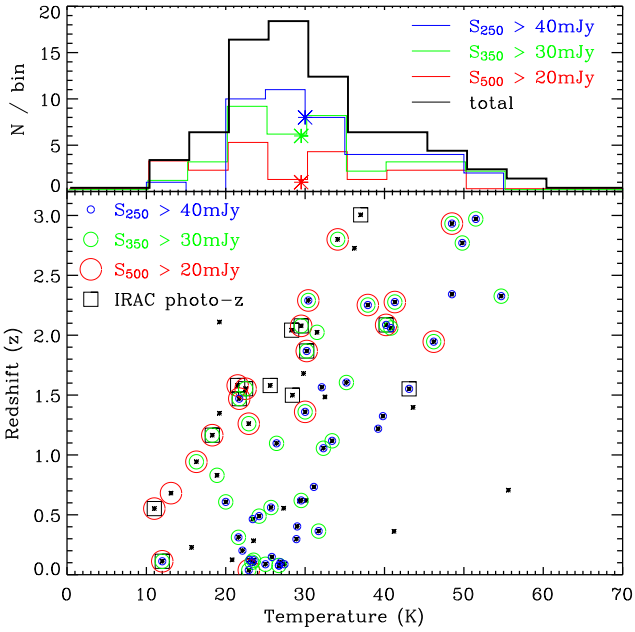

Figure 5. The dust temperature distribution, assuming $S_\nu \propto \nu^{2.0} B_\nu(T)$, for the 73 non-confused sources with redshift estimates. The bottom panel shows redshifts plotted against temperature, and the top panel collapses the redshift axis into a histogram. Similar to Fig. 4 we indicate the distributions for flux-limited sub-samples in each BLAST band, and indicate the medians with asterisks. We indicate the sources with IRAC-based photometric redshifts, as they are highly uncertain, and may be biased low. If these sources are at higher redshifts, they will move up and right in the lower panel. There is a negligible trend in rest-frame temperature for sources selected in different BLAST bands.

the higher-resolution LESS data are less prone to this problem, and therefore greatly improve the fits (if a smooth SED model such as the modified blackbody is assumed). Sources 6, 23, 25, 34, 40, 47, 51, 70, 109, 118, and 125 in Fig. E1 are more extreme examples that show this effect clearly. In all these cases, the SED model is a reasonable fit to the 250, 350, and 870 µm data points, but the 500 µm data lie above the model. Also, we find a median temperature of 36 K for the 26 galaxies at $z \geqslant 1.5$ with usable submm photometry from our sample. This is in good agreement with Fig. 9 from Dunlop et al. (2009) which shows that their S_{250}/S_{870} data are consistent with a $\beta = 1.5$, $T = 40$ K modified blackbody at these same redshifts (remembering that if we had chosen $\beta = 1.5$ instead of 2.0 our temperatures would be larger by about 5 K).

We also fit the star-forming galaxy SED templates of Dale et al. (2001) to the submm and FIR photometry (870–70 µm). Since these provide a fairly restricted range of SED shapes, they are only used to illustrate several basic features in the radio and mid/near-IR SEDs of our sample with respect to the rest-frame FIR peak (i.e., they should not be considered accurate fits beyond the 870–70 µm data). First, they give an indication of the location of the ~ 1.6 µm stellar bump that is redshifted into the IRAC bands for many of our sources (i.e., if the wavelength of the bump in the model corresponds to a local maximum in the IRAC data the redshift estimate is plausible). Also, since these are templates

for star-forming galaxies, sources from our sample with large excesses in either the mid-IR or radio may harbour AGN. Of the 73 sources with usable submm photometry and redshifts, 6 clear examples (8%) seem to exhibit such excesses: source 6 (mid-IR excess); source 34 (radio excess); 52 (radio and mid-IR excess); 54 (mid-IR excess); and 55 (radio excess); and 70 (mid-IR excess). For the remaining 42 submm confused sources, we fit the Dale et al. (2001) SED templates to all of non-confused data (VLA and *Spitzer*) to illustrate what plausible values in the submm might be. Finally, we note that some of the sources with IRAC-based photometric redshifts have particularly poor SED fits in the near-IR when compared to these templates, such as sources 33, 49, 53, and 124, as well as particularly cool inferred rest-frame temperatures (< 20 K). It is quite likely that these photometric redshifts are biased low, resulting in under-estimates of the inferred temperatures, and luminosities.

Next, we normalize each of the full radio–submm–IR SEDs by their total IR (TIR) 10–1000 μm luminosities using the modified blackbody fits. The sample is then plotted in bins of $L_{\rm TIR}$ in Fig. 6. This strategy minimizes scatter in the region of the SEDs probed by the submm photometry, and enables us to examine trends in the relative radio and mid/near-IR scatter as a function of luminosity. For reference, the same TIR-normalized SED from Dale et al. (2001) (with $\log_{10}(S_{60}/S_{100}) = -0.2$) is also plotted over each luminosity range to highlight differences. In the first instance this figure demonstrates that the vast majority of our proposed multi-wavelength counterparts are plausible: while there are a handful of significant outliers, the relative intensities of the radio and IR emission to the rest-frame FIR peak show reasonable consistency with each other, and with the models. It is clear that the radio–FIR correlation holds for most of the sample since the reference FIR-normalized star-forming galaxy SED has a radio spectrum that passes through most of the VLA data in each luminosity bin, regardless of the wavelength of the FIR peak (consistent with the findings of Ivison et al. 2009). On the other hand, the mid/near-IR SEDs exhibit significantly larger scatter; particularly in the range $11.5 < \log(L) < 12.8$ (a factor of ~ 100 peak-to-peak). Most of the sources mentioned previously with mid-IR excesses land in the two luminosity bins that span this range. While a correlation between AGN activity and FIR luminosity has been observed before (e.g. Takeuchi et al. 2003, 2004; Valiante et al. 2009), it is curious that our most luminous $12.8 < \log(L) < 13.5$ bin exhibits a more compact spread in SED properties consistent with pure star-formation. This result may not be significant, however, since this last luminosity bin has only 10 sources (whereas the next two faintest bins have 26 and 20 sources respectively). Fig. 6 also shows a strong correlation between luminosity and temperature: the least luminous sources peak at wavelengths $\lambda > 100$ μm, while the most luminous sources peak at wavelengths $\lambda < 100$ μm. Finally, this plot shows that the more luminous sources have a greater ratio of FIR luminosity to starlight (the 1.6 μm bump); the lowest-luminosity sources have SEDs more closely resembling normal star-forming galaxies than ULIRGs.

To explore the correlation between luminosity and temperature more fully, and the potential for its redshift evolution, we compare our sample with the local Universe. We use as our reference the distribution in integrated 42.5–122.5 μm FIR luminosity, and $C \equiv \log_{10}(S_{60}/S_{100})$ colour as measured by Chapin et al. (2009) based on *IRAS* data (an updated version of the analysis in Chapman et al. 2003). At redshift ~ 2.5 the entire BLAST 250–500 μm bandpass closely matches the 42.5–122.5 μm coverage from the *IRAS* 60 and 100 μm channels (see Fig. 6 in Chapin et al. 2009), so that tests for evolution at that redshift have only a min-

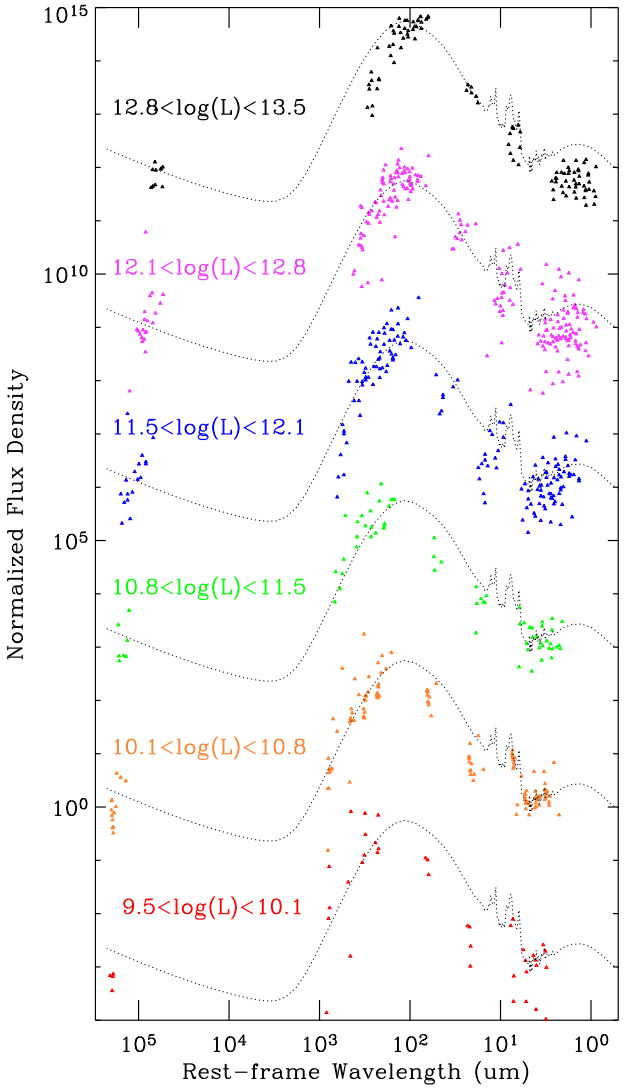

Figure 6. SEDs of the 73 galaxies with non-confused submm photometry and redshift estimates, normalized by the total infrared (TIR) 10–1000 μm luminosities of their modified blackbody fits. The SEDs are plotted in bins of $L_{\rm TIR}$ and offset by multiples of 10^3 for clarity. The SEDs of individual galaxies are shown in Fig. E1. A single $L_{\rm TIR}$-normalized SED template from Dale et al. (2001), for which $\log_{10}(S_{60}/S_{100}) = -0.2$, is shown as a dotted black line for reference in each bin. This comparison highlights several features: more luminous sources peak at shorter wavelengths (they are warmer); the radio-FIR correlation (the normalized model passes through the radio data irrespective of the FIR peak wavelength); the spread in the near/mid-IR SEDs (largest in the bins spanning $11.5 < \log(L) < 12.8$); and an increase in the size of the FIR peak with respect to stellar light (the 1.6 μm bump) with increasing luminosity.

imal dependence on the SED model used to fit the data. However, at lower redshifts, the BLAST bandpass samples significantly longer wavelengths in the rest-frame. Since the modified blackbody models used to fit the submm data fall-off much faster in the mid/far-IR than for real galaxies (since the shorter wavelengths sample warmer and/or optically-thick dust), we have fit the submm and FIR data for our sample using the more realistic star-forming galaxy SED templates of Dale et al. (2001). In Fig. 7 we plot the colours and luminosities for our sample using these SED fits. We colour-code the sources by redshift bin: $z < 0.5$ (blue crosses); $0.5 < z < 1.5$ (grey asterisks); $1.5 < z < 2.0$ (green triangles); and $2 < z < 42$ (red squares). Note that there is some quantization along the vertical axis for the sample since there are only 64 SED templates in the library, with colours ranging from about -0.55 to 0.26. Since this range is not quite as broad as that observed for the real sources, there is also some clipping (mostly problematic for the coolest sources at the bottom of the plot which are simply assigned the template SED with the most negative colour). We then compare this distribution with the local-Universe measurement of Chapin et al. (2009), including the 1σ envelope (solid and dotted black lines respectively).

We find that the temperatures for our sample lie systematically toward cooler (more negative) values than in the local Universe. At low redshifts, the lower temperatures are expected, since the submm bands sample the Rayleigh-Jeans tail of the thermal emission and are therefore biased toward the detection of cooler sources for a given flux-density–limit. Similarly, observations on the shorter-wavelength side of the thermal emission peak (such as with *IRAS*) are biased toward the detection of warmer sources — an effect which was accounted for in Chapin et al. (2009) in order to infer the properties of the entire population. Selection effects alone may therefore explain much of the discrepancy in temperatures seen here, and for 850 μm (e.g., Kovács et al. 2006; Coppin et al. 2008) selected galaxy populations (see also the discussion in Section 4.3 of Dye et al. 2009).

To test this theory, we have used a simple simulation to explore the effects of our selection function on the temperatures and luminosities of galaxies in different redshift slices. We take the local FIR colour-luminosity distribution, $\Phi(L, C)$, from Chapin et al. (2009) and assume that it does not evolve with redshift. We then calculate the total number of objects as a function of L and C in a redshift slice $z_0 < z < z_1$ as $\int_{z_0}^{z_1} \Phi(L, C)(dV/dz)dz$, where dV/dz is the differential volume element, and then use the Dale et al. (2001) SED templates to extrapolate to the BLAST wavelengths, and hence estimate observed flux densities. While the relative numbers of galaxies in different redshift slices will be incorrect, since it is known that significant luminosity and/or density evolution in the local luminosity function is required to fit observed submm number counts (e.g., Rowan-Robinson 2001; Scott et al. 2002; Lagache et al. 2003; Valiante et al. 2009; Rowan-Robinson 2009; Wilman et al. 2010), this calculation should give a good idea of the selection function *within* a redshift slice (provided that evolution across the slice is negligible). We then apply flux density cuts of 40, 30 and 20 mJy at 250, 350, and 500 μm respectively to mimic our observational selection function. We show 90% confidence intervals for these model distributions in the $z < 0.5$ and $2.0 < z < 4.0$ redshift bins with solid blue and red contours in Fig. 7, showing that they extend significantly below the rest-frame colour-luminosity correlation. To illustrate how this selection happens, we show the effect of the BLAST flux limits in the colour-luminosity plane at a single fixed redshift $z = 0.5$ as a thick dashed line (sources at that redshift should only be observable to the right of the limit). The detected galaxies tend to pile-up against this limit, since there are many more galaxies at fainter luminosities than at brighter luminosities in a given volume. If this limit were a vertical line in the plot, we would then expect the observed luminosities and colours to cluster around the rest-frame correlation (solid and dotted lines). However, since the limit is *inclined*, a dis-proportionate number of objects are detected toward the lower-left (lower luminosities, and cooler temperatures). Despite the simplicity of the model, the large noise in the observed sample, and potential for incorrect redshifts, the general trends in the data are clearly reproduced. This result suggests that there is no significant evolution in the correlation between FIR luminosity and temperature at high-redshifts, at least for the most luminous ($L_{\rm FIR} \gtrsim 10^{12}\,{\rm L}_{\odot}$) galaxies probed by our sample at $z \gtrsim 1$.

While the lack of evolution in our sample appears to be at odds with the evolution observed in the *stacked* SEDs with redshift described in Pascale et al. (2009), we note that our sample contains only ULIRGs at $z > 1.5$, whereas the stacked SEDs are dominated by significantly fainter galaxies. It is possible that 'normal' star-forming galaxies are generally warmer in the early Universe than in the present-day, while massive starburst galaxies do not differ appreciably. Another possible explanation is simply that the completeness to less luminous (and presumably cooler) galaxies drops off faster at high-redshift than it does for the more luminous (and warmer) galaxies in Pascale et al. (2009) — resulting in a bias to warmer stacked temperatures.

Our finding may also have interesting consequences for recent studies which indicate that SMGs are generally more extended and cooler than local ULIRGs. These claims have been made based on a variety of observations, including resolved MERLIN radio morphologies (e.g. Chapman et al. 2004), *Spitzer* MIPS and IRAC SEDs (e.g. Hainline et al. 2009), and *Spitzer* IRS spectra (e.g. Menéndez-Delmestre et al. 2009). Such observations point to a systematic difference in the physical conditions of major-mergers which produce SMGs (e.g., see resolved molecular gas observations and discussion in Tacconi et al. 2008), compared to ULIRGs in the local Universe. We note that Chanial et al. (2007) found a positive FIR luminosity-size correlation with a similar form to the temperature-luminosity correlation that we have used here. It may therefore be the case that the low-temperature bias for submm samples has picked out galaxies that are also more extended.

5.3 Source Blending

Counting the excess number of sources from the matching catalogue around submm source positions, with respect to random positions, was shown to be significantly larger than one in all 4 submm bands (Table 2). These excesses beg the obvious question: is the submm emission typically a blend of several matching catalogue sources, or is there, on average, a single submm bright source surrounded by other

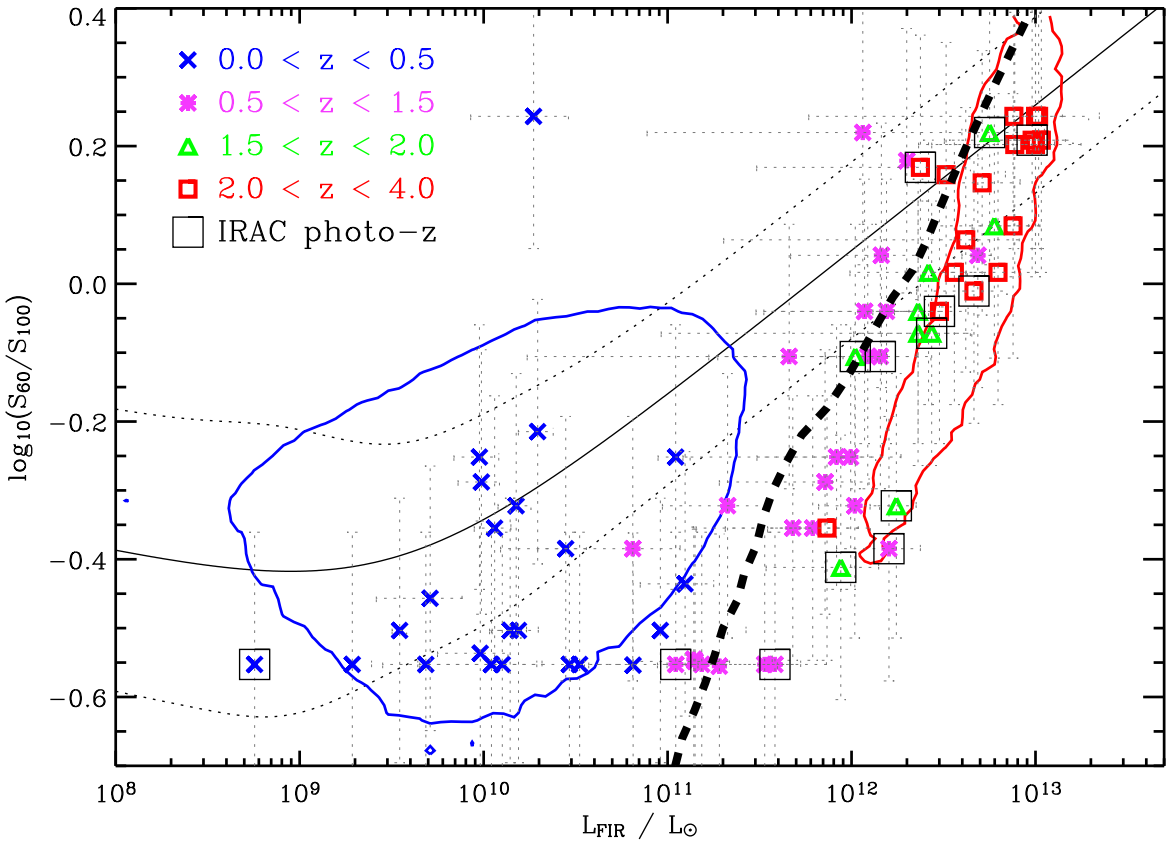

Figure 7. Rest-frame $\log_{10}(S_{60}/S_{100})$ colours vs. integrated 42.5–122.5 μm far-infrared (FIR) luminosities inferred from fits of Dale et al. (2001) SED templates to the submm and FIR photometry for our sample. The solid black line shows the local correlation derived from *IRAS* galaxies in Chapin et al. (2009), with the dotted black line its 68% confidence interval. The symbols are data points from our survey, divided into sources at $z < 0.5$, $0.5 < z < 1.5$, $1.5 < z < 2.0$, and $2.0 < z < 4.02$. We indicate the sources with IRAC-based photometric redshifts as they are highly uncertain, and may be biased low. If these sources are at higher redshifts, they will move up and right in this plot. For comparison, we generated a realization of sources from a non-evolving FIR colour-luminosity distribution (Chapin et al. 2009), extrapolating to the BLAST wavelengths using the Dale et al. (2001) SED templates, and applying flux density cuts 40, 30, and 20 mJy at 250, 350, and 500 μm respectively. Sub-samples were then made for the $0.0 < z < 0.5$ and $2.0 < z < 4.0$ redshifts bins, and their 90% confidence intervals are shown as solid blue and red contours respectively. For further illustration we also show the BLAST selection function at $z = 0.5$ with a thick black dashed line. The reasonable agreement between the model contours and the sample demonstrates that the generally cooler (more negative) colours for our sample can be explained by selection effects, rather than evolution in the colour-luminosity correlation at high-redshift.

faint sources? We consider three distinct cases, the first two of which would produce submm blends, and the third would not.

(i) The low-resolution submm source could be resolved into multiple components at the higher matching catalogue resolution. This is plausible, since it is known that about 10% of SCUBA sources are associated with double radio sources (e.g., Ivison et al. 2002; Chapman et al. 2005; Pope et al. 2006; Ivison et al. 2007). We also note that a significant clustering signal on angular scales < 1 arcmin has been measured for the LESS catalogue (Weiss et al. 2009).

(ii) Submm-bright matching catalogue sources could be Poisson distributed on the sky, and the broad submm beams tend to blend chance line-of-sight superpositions of such sources (the 'classical' source confusion problem, unrelated to physical clustering).

(iii) The submm sources could indeed be dominated by single matching catalogue sources, in which case the extra sources may be spatially correlated, but are not otherwise directly associated with the submm emitter (e.g., galaxies with lower star-formation rates in the same structures, or a foreground structure lensing background submm sources).

We believe that our data primarily exhibit examples of case (ii) (and it is the assumption used throughout this paper to identify counterparts), using a simple test based on the simulated maps of un-clustered source populations described in Section 2.1.3. Submm source lists were created using match-filtered images and culled at the same 3.75σ threshold as for the real data. We then created mock matching catalogues by choosing the N brightest sources from the known input catalogue, where N resulted in the same surface density as the real matching catalogue (Section 2.2). This matching catalogue is therefore also un-clustered. We then used the radial excess-counting procedure to calculate the average number of matches per source, and the radial positional uncertainties as described in Appendix B. We were

able to closely reproduce both the amplitudes of the excesses *and* the radial positional uncertainties in all bands without introducing any physical clustering, suggesting that it has a negligible impact on our analysis in this 708 arcmin^2 field. Further support for this scenario is also mentioned in Section 3.1: the excess matching catalogue counts around submm positions is correlated with the angular resolution. The same excess would be measured, regardless of PSF, if the submm emission were produced by single galaxies.

For individual submm sources, there are cases of what appear to be groups of proposed counterparts at different redshifts. See, for example, sources 2–5 in Fig. D1. In this particular case there also appears to be a fifth significant source of emission in most of the submm maps that is not identified, this being west and slightly south of the main clump, perhaps coincident with a faint radio source that lies within the saturated source apparent in the 3.6 μm map. The clump of sources 13–15 is a similar example. Sources 55 and 56 form a more well-separated example, with the former peaking in the 250 μm map, the latter in the 500 μm map, and with a double peak in the 350 μm map. The two optical photometric redshifts appear to be significantly different (0.1 and 0.6, respectively). Some of these sources could also be examples of foreground galaxies lensing background sources, although this effect is more difficult to quantify without accurate spectroscopic redshifts for most of the sample, and lensing models for each case.

There are also some examples of sources that could plausibly be interacting pairs at the same redshift (case (i)), more along the lines of radio-doubles detected in SCUBA surveys. The clearest example is the low-redshift interacting pair of sources 64 and 65 (also noted in Dunlop et al. 2009). Some more possible examples are: 77 and 78; 79 and 80; 86 and 88; and 120 and 121.

Based on our experiences with this survey, we expect confusion to have an impact on *Herschel*/SPIRE surveys as well, although at a lower significance given that the angular resolution has been improved by a factor of ~ 2 over BLAST. Since confusion clearly remains a problem in the highest-resolution 250 μm BLAST channel (36 arcsec FWHM), we can expect confusion to have a similar effect on the SPIRE 500 μm channel (same resolution). However, the highest-resolution SPIRE 250 μm channel has an angular resolution comparable to the 19 arcsec FWHM LESS data, which we have shown to lie in a regime where confusion plays a smaller role, given the surface density of submm sources under discussion. The radial excess counting prescription described in Appendix B will be an invaluable tool for characterizing the effects of confusion in these, and future submm surveys.

We note that source blending could have a serious impact on follow-up studies. If a large fraction of the brightest sources are blends, what is the best strategy for targeting 'clean' sources? We suggest that comparison of the submm source list with the local density of sources in the matching catalogue could offer a simple procedure for answering this question. Under the assumption that most of the confusion is caused by chance superpositions of sources in the matching catalogue (case (ii)), and assuming the matching catalogue itself is un-clustered, one would expect the surface density of the catalogue in the vicinity of an isolated submm source to be the same as at a random location, with one extra source added.

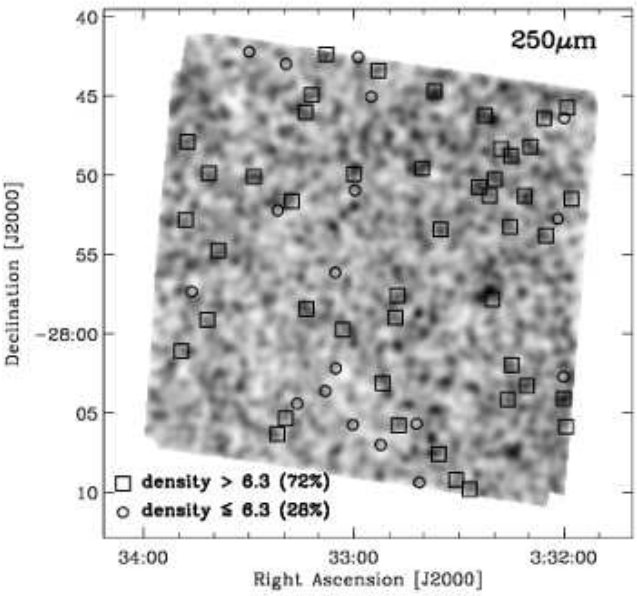

Figure 8. A density field created by convolving a map with the positions of all the matching catalogue sources, with the RMS positional uncertainty distributions from Table 2 at 250 μm (Gaussian with standard deviation σ_r). Over-plotted are the submm source positions in the 250 μm band. The expected value for this convolution if submm sources were produced by single sources from the matching catalogue would be the average catalogue source density across the whole map (5.3), plus 1, or 6.3. Submm positions with more than this number of matching catalogue sources nearby are indicated with squares, and those with fewer sources nearby with circles (i.e., squares are more likely to be blends than isolated sources — about 72% of the sample).

We have produced a density field for the matching catalogue convolved with the 250 μm positional uncertainty distribution in Fig. 8 to illustrate this point. The squares indicate locations in the density field where 250 μm-selected sources land on over-densities (more than expected background value of 5.3, the average value for the entire smoothed map, plus 1 submm source), and circles denote sources in regions below this threshold. In total, 73% of the 250 μm sources land on such over-densities, whereas we would expect the fraction to be evenly-distributed above and below this threshold if confusion were not an issue. Therefore the remaining 27% are likely the easiest to study with follow-up observations: there is less chance that they will be resolved into multiple components with interferometric measurements, and there may also be less ambiguity regarding their counterparts.

Finally, what would the effect be on our analysis if there *were* significant clustering in the matching catalogue around the submm sources (case iii)? In this case the radial excess distributions (Fig. B1), and our measurements of $q(s, c)$ (Figs. B2–B4) would trace the properties of the clustered objects (e.g., spatial extent, colours and brightnesses), rather than the properties submm sources, and we would end up with many more false positives than the target 10% rate. While we do not believe this is the most likely scenario based on the arguments made in this section, and the fact that the SEDs for the counterparts seem to match models for star-

forming galaxies, only higher-resolution studies will be able to settle this issue unambiguously.

6 CONCLUSIONS

We have performed a deep multi-wavelength study of individual sources from the BLAST 250, 350, and 500 μm survey within the Extended Chandra Deep Field South (ECDFS). By comparing the BLAST data with LABOCA ECDFS Submm Survey (LESS) maps at 870 μm we have been able to greatly improve the positional uncertainties and longer-wavelength (Rayleigh-Jeans tail) SEDs for our sample. Compared to the earlier BLAST studies of Dye et al. (2009), Ivison et al. (2009) and Dunlop et al. (2009), our methodology for identifying counterparts and measuring flux densities differ in several key respects:

- We have developed a new 'matched filter' that compensates for source confusion when identifying submm sources. For the BLAST bands, in which the contribution to the total noise by source confusion is roughly a factor of two larger than the instrumental noise, there is a significant improvement in SNR of approximately 15–20% in all bands. In contrast, there is only a minimal improvement of about 5% for the LESS data since the confusion and instrumental noise components are approximately the same.
- Identifications in our combined radio/IR matching catalogue have been made using Likelihood Ratios that incorporate more prior information than traditional 'P' statistics. With a threshold spurious ID rate set at 10%, we find 52, 50, and 31 matches to 64, 67, and 55 submm source positions at 250, 350, and 500 μm, respectively. This is a significant improvement compared to the match rates obtained using 10% cuts on P giving 45, 31, and 12 matches in the 24 μm catalogue, and 51, 35, and 17 matches in 1.4 GHz catalogue. Most of the gain is at 500 μm where the beam is so large that any additional information to help the process clearly makes a large difference. Combining the identifications made independently in each band, approximately 80% of the BLAST selected sources have at least one potential counterpart.
- We obtain submm photometry for the 125 unique identifications in the matching catalogue by performing a simultaneous fit of the submm PSFs at the precise ID locations in each of the four original (un-smoothed) submm maps. This procedure results in useful measurements for 83 sources; the remaining 42 sources are too close to one another to reliably disentangle the flux densities produced by each of the contributing objects. In order to make further progress in such cases, prior information for the SEDs will likely be needed (see, for example, the work of Roseboom et al. 2009).
- Our procedure for identifying and measuring the flux densities has compensated for much of the 'flux-boosting' present in the original flux-limited submm source lists. Comparing the number counts of our final catalogue in the BLAST bands with the $P(D)$ counts from Patanchon et al. (2009) we find good agreement above 40 mJy at 250 μm, 30 mJy at 350 μm and with somewhat lower completeness reaching a maximum of $\sim 66\%$ above 20 mJy at 500 μm.

We then proceeded to identify redshifts for the counterparts, and hence probe the rest-frame properties of our sample:

- Of the 83 sources with usable submm photometry, 73 counterparts have redshifts: 23 are optical spectroscopic redshifts; 37 are optical photometric redshifts; and 14 are IRAC photometric redshifts. The median of the entire distribution is $z = 1.1$ with an interquartile range 0.4–1.9. Restricting ourselves to sub-samples above the flux-density limits mentioned previously shows a clear trend in increasing redshift with observed wavelength: a median $z = 1.1$ with an interquartile range 0.2–1.9 at 250 μm; a median $z = 1.3$ with an interquartile range 0.6–2.1 at 350 μm; and a median $z = 1.6$ with an interquartile range 1.2–2.3 at 500 μm.
- Fitting modified blackbody SEDs of the form $S_\nu \propto \nu^{2.0} B_\nu(T)$ to the 73 sources with useable submm photometry and redshifts, we establish rest-frame cold-dust temperatures. The total distribution as a median $T = 29$ K and interquartile range 23–36 K. There is almost no variation in the temperatures of the different flux-limited sub-samples: a median $T = 30$ K with an interquartile range 25–40 K at 250 μm; a median $T = 30$ K with an interquartile range 23–38 K at 350 μm; and a median $T = 30$ K with an interquartile range 22–38 K at 500 μm.
- We have also fit star-forming galaxy SED templates from the library of Dale et al. (2001) (which span the radio–near-IR) to the submm and FIR photometry of our sample. Generally speaking there is good correspondance between these models and the photometry in the radio and near/mid-IR, confirming that most of the emission is probably powered by star-formation. However, about 8% of the sample exhibits a significant excess in either (or both) of these wavelength regimes, which could indicate AGN activity. We note that these features are restricted to sources with luminosities primarily in the range $11.5 < \log(L_{\rm FIR}) < 12.8$, near the bright end of our sample.
- Finally, we compare the distribution of luminosity and cold dust temperature in our sample with the local-Universe measurement of Chapin et al. (2009). While the submm colours of our sources appear systematically cooler at all luminosities compared to the local distribution, we have determined that the distribution is consistent with selection effects in our survey. We therefore find no evidence for evolution in the temperature-luminosity correlation out to $z \sim 2.5$.

7 ACKNOWLEDGEMENTS

BLAST acknowledges the support of NASA through grant numbers NAG5-12785, NAG5-13301, and NNGO-6GI11G, the NSF Office of Polar Programs, the Canadian Space Agency, the Natural Sciences and Engineering Research Council (NSERC) of Canada, and STFC. This paper contains data obtained by APEX, which is operated by the Max-Planck-Institut für Radioastronomie, the European Southern Observatory, and the Onsala Space Observatory. LESS is a joint MPI-ESO collaboration and the data were obtained during the following ESO observing runs: 078.F-9028(A), 079.F-9500(A), 080.A-3023(A), and 081.F-9500(A). This work is based in part on observations made with the Spitzer Space Telescope, which is operated by the Jet Propulsion Laboratory, California Institute of Technology under a contract with NASA. IRS and KEKC acknowledge support from STFC. JSD acknowledges the support of

the Royal Society through a Wolfson Research Merit Award. EC thanks John Peacock and Seb Oliver for useful discussions regarding Likelihood Ratios.

REFERENCES

Aretxaga I., Hughes D. H., Chapin E. L., Gaztañaga E., Dunlop J. S., Ivison R. J., 2003, MNRAS, 342, 759

Austermann J. E., Dunlop J. S., Perera T. A., Scott K. S., Wilson G. W., Aretxaga I., Hughes D. H., Almaini O., Chapin E. L., Chapman S. C., Cirasuolo M., Clements D. L., Coppin K. E. K., Dunne L., 2010, MNRAS, 401, 160

Barger A. J., Cowie L. L., Sanders D. B., Fulton E., Taniguchi Y., Sato Y., Kawara K., Okuda H., 1998, Nature, 394, 248

Barnard V. E., Vielva P., Pierce-Price D. P. I., Blain A. W., Barreiro R. B., Richer J. S., Qualtrough C., 2004, MNRAS, 352, 961

Barreiro R. B., Sanz J. L., Herranz D., Martínez-González E., 2003, MNRAS, 342, 119

Blain A. W., Smail I., Ivison R. J., Kneib J.-P., Frayer D. T., 2002, PhR, 369, 111

Borys C., Chapman S., Halpern M., Scott D., 2003, MNRAS, 344, 385

Brammer G. B., van Dokkum P. G., Coppi P., 2008, ApJ, 686, 1503

Chanial P., Flores H., Guiderdoni B., Elbaz D., Hammer F., Vigroux L., 2007, A&A, 462, 81

Chapin E. L., Ade P. A. R., Bock J. J., Brunt C., Devlin M. J., Dicker S., Griffin M., Gundersen J. O., Halpern M., Hargrave P. C., Hughes D. H., 2008, ApJ, 681, 428

Chapin E. L., Hughes D. H., Aretxaga I., 2009, MNRAS, 393, 653

Chapin E. L., Pope A., Scott D., Aretxaga I., Austermann J. E., Chary R., Coppin K., Halpern M., Hughes D. H., Lowenthal J. D., Morrison G. E., Perera T. A., Scott K. S., Wilson G. W., Yun M. S., 2009, MNRAS, 398, 1793

Chapman S. C., Blain A. W., Ivison R. J., Smail I. R., 2003, Nature, 422, 695

Chapman S. C., Blain A. W., Smail I., Ivison R. J., 2005, ApJ, 622, 772

Chapman S. C., Helou G., Lewis G. F., Dale D. A., 2003, ApJ, 588, 186

Chapman S. C., Smail I., Windhorst R., Muxlow T., Ivison R. J., 2004, ApJ, 611, 732

Clements D., Eales S., Wojciechowski K., Webb T., Lilly S., Dunne L., Ivison R., McCracken H., Yun M., James A., Brodwin M., Le Fèvre O., Gear W., 2004, MNRAS, 351, 447

Coppin K., Chapin E. L., Mortier A. M. J., Scott S. E., Borys C., Dunlop J. S., Halpern M., Hughes D. H., Pope A., Scott D., Serjeant S., Wagg J., Alexander D. M., 2006, MNRAS, 372, 1621

Coppin K., Halpern M., Scott D., Borys C., Chapman S., 2005, MNRAS, 357, 1022

Coppin K., Halpern M., Scott D., Borys C., Dunlop J., Dunne L., Ivison R., Wagg J., Aretxaga I., Battistelli E., Benson A., Blain A., Chapman S., Clements D., Dye S., Farrah D., Hughes D., Jenness T., 2008, MNRAS, 384, 1597

Coppin K. E. K., Smail I., Alexander D. M., Weiss A., Walter F., Swinbank A. M., Greve T. R., Kovacs A., De Breuck C., Dickinson M., Ibar E., Ivison R. J., Reddy N., Spinrad H., Stern D., Brandt W. N., Chapman S. C., Dannerbauer H., 2009, MNRAS, 395, 1905

Cowie L. L., Barger A. J., Kneib J.-P., 2002, Astron. J., 123, 2197

Dale D. A., Helou G., Contursi A., Silbermann N. A., Kolhatkar S., 2001, ApJ, 549, 215

Dannerbauer H., Lehnert M. D., Lutz D., Tacconi L., Bertoldi F., Carilli C., Genzel R., Menten K. M., 2004, ApJ, 606, 664

Devlin M. J., Ade P. A. R., Aretxaga I., Bock J. J., Chapin E. L., Griffin M., Gundersen J. O., Halpern M., Hargrave P. C., Hughes D. H., Klein J., Marsden G., Martin P. G., Mauskopf P., Moncelsi L., Netterfield C. B., 2009, Nature, 458, 737

Dole H., Lagache G., Puget J., Caputi K. I., Fernández-Conde N., Le Floc'h E., Papovich C., Pérez-González P. G., Rieke G. H., Blaylock M., 2006, A&A, 451, 417

Downes A. J. B., Peacock J. A., Savage A., Carrie D. R., 1986, MNRAS, 218, 31

Dunlop J. S., Ade P. A. R., Bock J. J., Chapin E. L., Cirasuolo M., Coppin K. E. K., Devlin M. J., Griffin M., Greve T. R., Gundersen J. O., Halpern M., Hargrave P. C., 2009, ArXiv e-prints

Dye S., Ade P. A. R., Bock J. J., Chapin E. L., Devlin M. J., Dunlop J. S., Eales S. A., Griffin M., Gundersen J. O., Halpern M., Hargrave P. C., Hughes D. H., Klein J., 2009, ArXiv e-prints

Eales S., Chapin E. L., Devlin M. J., Dye S., Halpern M., Hughes D. H., Marsden G., Mauskopf P., Moncelsi L., Netterfield C. B., Pascale E., Patanchon G., Raymond G., Rex M., Scott D., Semisch C., Siana B., Truch M. D. P., Viero M. P., 2009, ApJ, 707, 1779

Fixsen D. J., Dwek E., Mather J. C., Bennett C. L., Shafer R. A., 1998, ApJ, 508, 123

Fox M. J., Efstathiou A., Rowan-Robinson M., Dunlop J. S., Scott S., Serjeant S., Mann R. G., Oliver S., Ivison R. J., Blain A., Almaini O., Hughes D., Willott C. J., Longair M., Lawrence A., Peacock J. A., 2002, MNRAS, 331, 839

Gawiser E., van Dokkum P. G., Herrera D., Maza J., Castander F. J., Infante L., Lira P., Quadri R., Toner R., Treister E., Urry C. M., Altmann M., Assef R., Christlein D., 2006, ApJS, 162, 1

Grazian A., Fontana A., de Santis C., Nonino M., Salimbeni S., Giallongo E., Cristiani S., Gallozzi S., Vanzella E., 2006, A&A, 449, 951

Greve T. R., Ivison R. J., Bertoldi F., Stevens J. A., Dunlop J. S., Lutz D., Carilli C. L., 2004, MNRAS, 354, 779

Güsten R., Nyman L. Å., Schilke P., Menten K., Cesarsky C., Booth R., 2006, A&A, 454, L13

Hainline L. J., Blain A. W., Smail I., Frayer D. T., Chapman S. C., Ivison R. J., Alexander D. M., 2009, ApJ, 699, 1610

Holland W. S., Robson E. I., Gear W. K., Cunningham C. R., Lightfoot J. F., Jenness T., Ivison R. J., Stevens J. A., Ade P. A. R., Griffin M. J., Duncan W. D., Murphy J. A., Naylor D. A., 1999, MNRAS, 303, 659

Hughes D. H., Serjeant S., Dunlop J., Rowan-Robinson M., Blain A., Mann R. G., Ivison R., Peacock J., Efstathiou

A., Gear W., Oliver S., Lawrence A., Longair M., Goldschmidt P., Jenness T., 1998, Nature, 394, 241
Iono D., Peck A. B., Pope A., Borys C., Scott D., Wilner D. J., Gurwell M., Ho P. T. P., Yun M. S., Matsushita S., Petitpas G. R., Dunlop J. S., Elvis M., Blain A., Le Floc'h E., 2006, ApJL, 640, L1
Ivison R. J., Alexander D. M., Biggs A. D., Brandt W. N., Chapin E. L., Coppin K. E. K., Devlin M. J., Dickinson M., Dunlop J., Dye S., Eales S. A., Frayer D. T., Halpern M., 2009, ArXiv e-prints
Ivison R. J., Greve T. R., Dunlop J. S., Peacock J. A., Egami E., Smail I., Ibar E., van Kampen E., Aretxaga I., Babbedge T., Biggs A. D., Blain A. W., Chapman S. C., Clements D. L., 2007, MNRAS, 380, 199
Ivison R. J., Greve T. R., Serjeant S., Bertoldi F., Egami E., Mortier A. M. J., Alonso-Herrero A., Barmby P., Bei L., Dole H., Engelbracht C. W., Fazio G. G., Frayer D. T., 2004, ApJS, 154, 124
Ivison R. J., Greve T. R., Smail I., Dunlop J. S., Roche N. D., Scott S. E., Page M. J., Stevens J. A., Almaini O., Blain A. W., Willott C. J., Fox M. J., Gilbank D. G., Serjeant S., Hughes D. H., 2002, MNRAS, 337, 1
Khan S. A., Shafer R. A., Serjeant S., Willner S. P., Pearson C. P., Benford D. J., Staguhn J. G., Moseley S. H., Sumner T. J., Ashby M. L. N., Borys C. K., Chanial P., Clements D. L., Dowell C. D., Dwek E., Fazio G. G., Kovács A., Le Floc'h E., Silverberg R. F., 2007, ApJ, 665, 973
Klaas U., Haas M., Müller S. A. H., Chini R., Schulz B., Coulson I., Hippelein H., Wilke K., Albrecht M., Lemke D., 2001, A&A, 379, 823
Kovács A., Chapman S. C., Dowell C. D., Blain A. W., Ivison R. J., Smail I., Phillips T. G., 2006, ApJ, 650, 592
Lagache G., Dole H., Puget J.-L., 2003, MNRAS, 338, 555
Laurent G. T., Aguirre J. E., Glenn J., Ade P. A. R., Bock J. J., Edgington S. F., Goldin A., Golwala S. R., Haig D., Lange A. E., Maloney P. R., Mauskopf P. D., Nguyen H., Rossinot P., Sayers J., Stover P., 2005, ApJ, 623, 742
Lutz D., Dunlop J. S., Almaini O., Andreani P., Blain A., Efstathiou A., Fox M., Genzel R., Hasinger G., Hughes D., 2001, A&A, 378, 70
Magnelli B., Elbaz D., Chary R. R., Dickinson M., Le Borgne D., Frayer D. T., Willmer C. N. A., 2009, A&A, 496, 57
Mann R. G., Oliver S. J., Serjeant S. B. G., Rowan-Robinson M., Baker A., Eaton N., Efstathiou A., Goldschmidt P., Mobasher B., Sumner T. J., 1997, MNRAS, 289, 482
Marsden G., Ade P. A. R., Bock J. J., Chapin E. L., Devlin M. J., Dicker S. R., Griffin M., Gundersen J. O., Halpern M., Hargrave P. C., Hughes D. H., Klein J., Mauskopf P., Magnelli B., Moncelsi L., Netterfield C. B., Ngo H., 2009, ArXiv e-prints
Menéndez-Delmestre K., Blain A. W., Smail I., Alexander D. M., Chapman S. C., Armus L., Frayer D., Ivison R. J., Teplitz H., 2009, ApJ, 699, 667
Miller N. A., Fomalont E. B., Kellermann K. I., Mainieri V., Norman C., Padovani P., Rosati P., Tozzi P., 2008, ApJS, 179, 114
Pascale E., Ade P. A. R., Bock J. J., Chapin E. L., Chung J., Devlin M. J., Dicker S., Griffin M., Gundersen J. O., Halpern M., Hargrave P. C., Hughes D. H., Klein J., MacTavish C. J., 2008, ApJ, 681, 400
Pascale E., Ade P. A. R., Bock J. J., Chapin E. L., Devlin M. J., Dye S., Eales S. A., Griffin M., Gundersen J. O., Halpern M., Hargrave P. C., Hughes D. H., Klein J., 2009, ArXiv e-prints
Patanchon G., Ade P. A. R., Bock J. J., Chapin E. L., Devlin M. J., Dicker S., Griffin M., Gundersen J. O., Halpern M., Hargrave P. C., Hughes D. H., Klein J., Marsden G., Martin P. G., 2008, ApJ, 681, 708
Patanchon G., Ade P. A. R., Bock J. J., Chapin E. L., Devlin M. J., Dicker S. R., Griffin M., Gundersen J. O., Halpern M., Hargrave P. C., Hughes D. H., Klein J., Marsden G., Mauskopf P., 2009, ApJ, 707, 1750
Perera T. A., Chapin E. L., Austermann J. E., Scott K. S., Wilson G. W., Halpern M., Pope A., Scott D., Yun M. S., Lowenthal J. D., Morrison G., Aretxaga I., Bock J. J., Coppin K., Crowe M., Frey L., Hughes D. H., Kang Y., Kim S., Mauskopf P. D., 2008, ArXiv e-prints, 806
Pope A., Scott D., Dickinson M., Chary R.-R., Morrison G., Borys C., Sajina A., Alexander D. M., Daddi E., Frayer D., MacDonald E., Stern D., 2006, MNRAS, 370, 1185
Pope E. A., 2007, PhD thesis, The University of British Columbia (Canada
Puget J., Abergel A., Bernard J., Boulanger F., Burton W. B., Desert F., Hartmann D., 1996, A&A, 308, L5+
Roseboom I. G., Oliver S., Parkinson D., Vaccari M., 2009, MNRAS, 400, 1062
Rowan-Robinson M., 2001, ApJ, 549, 745
Rowan-Robinson M., 2009, MNRAS, 394, 117
Rowan-Robinson M., Babbedge T., Oliver S., Trichas M., Berta S., Lonsdale C., Smith G., Shupe D., Surace J., Arnouts S., 2008, MNRAS, 386, 697
Rutledge R. E., Brunner R. J., Prince T. A., Lonsdale C., 2000, ApJS, 131, 335
Sanders D. B., Mirabel I. F., 1996, ARAA, 34, 749
Sawicki M., 2002, Astron. J., 124, 3050
Scott K. S., Austermann J. E., Perera T. A., Wilson G. W., Aretxaga I., Bock J. J., Hughes D. H., Kang Y., Kim S., Mauskopf P. D., Sanders D. B., Scoville N., Yun M. S., 2008, MNRAS, 385, 2225
Scott K. S., Yun M. S., Wilson G. W., Austermann J. E., Aguilar E., Aretxaga I., Ezawa H., Ferrusca D., Hatsukade B., Hughes D. H., Iono D., 2010, ArXiv e-prints
Scott S. E., Fox M. J., Dunlop J. S., Serjeant S., Peacock J. A., Ivison R. J., Oliver S., Mann R. G., Lawrence A., Efstathiou A., Rowan-Robinson M., Hughes D. H., Archibald E. N., Blain A., Longair M., 2002, MNRAS, 331, 817
Serjeant S., Dunlop J. S., Mann R. G., Rowan-Robinson M., Hughes D., Efstathiou A., Blain A., Fox M., Ivison R. J., Jenness T., Lawrence A., Longair M., Oliver S., Peacock J. A., 2003, MNRAS, 344, 887
Serjeant S., Dye S., Mortier A., Peacock J., Egami E., Cirasuolo M., Rieke G., Borys C., Chapman S., Clements D., Coppin K., 2008, MNRAS, 386, 1907
Simpson C., Eisenhardt P., 1999, PASP, 111, 691
Siringo G., Kreysa E., Kovács A., Schuller F., Weiß A., Esch W., Gemünd H., Jethava N., Lundershausen G., Colin A., Güsten R., Menten K. M., Beelen A., Bertoldi F., Beeman J. W., Haller E. E., 2009, A&A, 497, 945
Smail I., Ivison R. J., Blain A. W., 1997, ApJL, 490, L5+
Smail I., Ivison R. J., Owen F. N., Blain A. W., Kneib J., 2000, ApJ, 528, 612

Stetson P. B., 1987, Publ. Astron. Soc. Pac., 99, 191
Sutherland W., Saunders W., 1992, MNRAS, 259, 413
Tacconi L. J., Genzel R., Smail I., Neri R., Chapman S. C., Ivison R. J., Blain A., Cox P., Omont A., Bertoldi F., Greve T., 2008, ApJ, 680, 246
Takeuchi T. T., Yoshikawa K., Ishii T. T., 2003, ApJL, 587, L89
Takeuchi T. T., Yoshikawa K., Ishii T. T., 2004, ApJL, 606, L171
Taylor E. N., Franx M., van Dokkum P. G., Quadri R. F., Gawiser E., Bell E. F., Barrientos L. F., Blanc G. A., Castander F. J., Damen M., Gonzalez-Perez V., Hall P. B., Herrera D., Hildebrandt H., 2009, ApJS, 183, 295
Tegmark M., de Oliveira-Costa A., 1998, ApJL, 500, L83+
Truch M. D. P., Ade P. A. R., Bock J. J., Chapin E. L., Devlin M. J., Dicker S. R., Griffin M., Gundersen J. O., Halpern M., Hargrave P. C., Hughes D. H., Klein J., Marsden G., 2009, ApJ, 707, 1723
Valiante E., Lutz D., Sturm E., Genzel R., Chapin E. L., 2009, ApJ, 701, 1814
Vio R., Andreani P., Wamsteker W., 2004, A&A, 414, 17
Webb T. M., Eales S. A., Lilly S. J., Clements D. L., Dunne L., Gear W. K., Ivison R. J., Flores H., Yun M., 2003, ApJ, 587, 41
Weiss A., Kovacs A., Coppin K., Greve T. R., Walter F., Smail I., Dunlop J. S., Knudsen K. K., Alexander D. M., Bertoldi F., Brandt W. N., Chapman S. C., Cox P., 2009, ArXiv e-prints
Wiebe D. V., Ade P. A. R., Bock J. J., Chapin E. L., Devlin M. J., Dicker S., Griffin M., Gundersen J. O., Halpern M., Hargrave P. C., Hughes D. H., Klein J., Marsden G., Martin P. G., 2009, ApJ, 707, 1809
Wilman R. J., Jarvis M. J., Mauch T., Rawlings S., Hickey S., 2010, ArXiv e-prints
Wilson G. W., Austermann J. E., Perera T. A., Scott K. S., Ade P. A. R., Bock J. J., Glenn J., Golwala S. R., Kim S., Kang Y., Lydon D., Mauskopf P. D., Predmore C. R., Roberts C. M., Souccar K., Yun M. S., 2008, MNRAS, 386, 807
Wolf C., Hildebrandt H., Taylor E. N., Meisenheimer K., 2008, A&A, 492, 933
Wolf C., Meisenheimer K., Kleinheinrich M., Borch A., Dye S., Gray M., Wisotzki L., Bell E. F., Rix H., Cimatti A., Hasinger G., Szokoly G., 2004, A&A, 421, 913
Younger J. D., Fazio G. G., Huang J., Yun M. S., Wilson G. W., Ashby M. L. N., Gurwell M. A., Lai K., Peck A. B., Petitpas G. R., Wilner D. J., Iono D., Kohno K., Kawabe R., 2007, ApJ, 671, 1531
Yun M. S., Aretxaga I., Ashby M. L. N., Austermann J., Fazio G. G., Giavalisco M., Huang J.-S., Hughes D. H., Kim S., Lowenthal J. D., Perera T., Scott K., Wilson G., Younger J. D., 2008, MNRAS, 389, 333

APPENDIX A: MATCHED FILTER

Here we describe a filter for identifying point sources in maps containing significant contributions of both instrumental noise and confusion due to blending of other point sources (see e.g. Tegmark & de Oliveira-Costa 1998; Barreiro et al. 2003; Vio et al. 2004, for related studies of point sources in maps of the Cosmic Microwave Background). We formulate the problem as follows: we wish to find the 'matched filter', F, that maximizes the SNR one would obtain when cross-correlating F with the signal of interest, S – in our case, a point source whose shape is identical to the PSF – in the presence of noise, N. We proceed by expressing the total SNR resulting from this operation, ϕ, in Fourier space,

$$\phi \equiv \frac{\text{Signal}}{\text{Noise}} = \frac{\sum_k \hat{F}_k^T \hat{S}_k}{\left(\sum_k |\hat{F}_k^T \hat{N}_k|^2\right)^{1/2}}. \quad \text{(A1)}$$

In this expression the carets denote discrete Fourier transforms, and the index k runs over all elements in the spatial frequency domain. The superscript 'T' indicates that we use the transpose of F in the expression.[4] Taking the partial derivatives of ϕ with respect to each mode j in the filter, $\hat{F}_j^T$, and setting them to 0, one can solve for the filter that maximizes the SNR:

$$0 = \frac{\partial \phi}{\partial \hat{F}_j^T} \quad \text{(A2)}$$

$$= \frac{\hat{S}_j}{\left(\sum_k |\hat{F}_k^T \hat{N}_k|^2\right)^{1/2}} - \hat{F}_j^T |\hat{N}_j|^2 \left(\frac{\sum_k \hat{F}_k^T \hat{S}_k}{\left(\sum_k |\hat{F}_k^T \hat{N}_k|^2\right)^{3/2}} \right)$$

$$\Rightarrow \hat{F}_j^T = \frac{\hat{S}_j}{|\hat{N}_j|^2} \left(\frac{\sum_k |\hat{F}_k^T \hat{N}_k|^2}{\sum_k \hat{F}_k^T \hat{S}_k} \right) \propto \frac{\hat{S}_j}{|\hat{N}_j|^2}. \quad \text{(A3)}$$

In other words, in Fourier space the matched filter is simply the PSF weighted by the inverse noise variance at each spatial frequency. In the case of an isolated point source in a field of white noise, this expression results in the PSF, since $\hat{N}$ is constant. This is the well-known result (e.g. Stetson 1987) that the best way to find point sources in a noisy map is to convolve with the PSF. However, this procedure is only optimal if the noise is white. For our submm maps we consider two components of noise: instrumental white noise, $N_{\rm w}$, and the confusion noise caused by other point sources, $N_{\rm c}$.

For the case at hand we estimate $N_{\rm w}$ (constant at all spatial frequencies) assuming typical noise values at the centres of each submm ECDF-S map: 32, 29, 27, and 2 mJy[5] at 250, 350, 500, and 870 μm, respectively (Devlin et al. 2009; Weiss et al. 2009). For the confusion noise, $N_{\rm c}$, we use the counts inferred using $P(D)$ analyses from Patanchon et al. (2009) and Weiss et al. (2009), and knowledge of the PSF. In the absence of noise (and assuming no spatial clustering of sources), the sky can be thought of as a random superposition of PSF shapes of different amplitude (i.e., δ functions smoothed by the PSF and scaled by the point source flux density). In Fourier space, a simulated map therefore looks like a white noise distribution multiplied by the Fourier transform of the transpose of the PSF (by the convolution theorem); in other words the power spectrum of confusion noise rolls off in the same way as the PSF, but with a different normalization. To determine how the power spectrum

[4] The cross-correlation of the filter with the signal is equivalent to convolving the signal with the complex conjugate transpose of the filter. Since we are dealing with real-valued signals this operations reduces to a transpose. The convolution is then a simple product in Fourier space between the two transformed quantities.

[5] These are the noise values in the raw *un-smoothed* maps at each wavelength.

of the PSF should be scaled we simulate maps in each band as described above, and use the ratios of the standard deviations of these noise realizations to the standard deviations of the PSFs.

As an example of this procedure, the estimated noise power spectrum at 500 μm, and resulting matched filter in real space (both azimuthally averaged) are shown in Fig. A1. One sees that the matched filter is somewhat narrower than the PSF filter (which has been used in most previous SMG studies) and has ringing at larger angular scales, giving it similar properties to the 'Mexican hat' kernel (see for example discussion and references within Barnard et al. 2004). In this particular case, the first large negative ring effectively removes a local baseline estimated at radii ~ 50 arcsec, and hence corrects the flux density slightly for other nearby blended sources. The matched filter is also qualitatively similar to the filter used to detect sources in deep AzTEC maps (e.g., Scott et al. 2008; Perera et al. 2008). However, in those cases only sources of atmospheric and instrumental noise are considered, since the spatial noise power spectrum is estimated using 'jackknife maps' (produced by differencing alternating portions of the data), which explicitly removes the contribution of astronomical sources. We emphasize that here we are using such a filter to optimally extract sources in a *confused* background. Note also that in a language familiar in other fields, our filter is essentially a Wiener filter which includes source confusion explicitly as a noise term.

In addition to the calculation we describe here, we also convolved simulated maps (containing both point sources and instrumental noise) with Gaussian filters of different widths, and determined the FWHMs that optimized the SNR of point sources. These simple tests gave results comparable to the more detailed calculation above, although the SNR was slightly lower due to the lack of ringing to compensate for the noise at larger angular scales.

It should be noted that in the development of our filter we have assumed that the instrumental noise is constant across the map. Of course, in general this is not true, and one could in principle derive a different filter at each position. For the BLAST maps under discussion, a separate filter should certainly be used to detect sources in BGS-Wide and BGS-Deep, but for the present study the noise was close to uniform across the ECDF-S, and hence we used a single filter for the whole map.

As a consequence of Eq. A3, the peak SNR for an isolated point source in a field of white noise (for which $\hat{N}_k$ is constant) is obtained by convolution with a Gaussian of the same FWHM as the instrumental PSF. In the opposite extreme, for a map of confused point sources with no instrumental noise, the optimal filter is the inverse of the PSF in Fourier space, i.e., the map is *de*-convolved by the beam. For real data in which instrumental noise and confusion are both present, the degree to which the map is actually de-convolved depends on the relative amplitudes of the two noise components (see left panel of Fig. A1). The source confusion depends on the number counts (and therefore the SEDs and redshift distribution) of galaxies in the observed band, and beam size, and the instrumental noise depends on the detector sensitivity and integration time. For the data described here, these two contributions are comparable, since the submm surveys of the ECDF-S were designed to be *just* confusion-limited. The bottom-line is that in the BLAST bands, considering both noise terms, convolving with kernels that are *smaller* than the instrumental PSFs can give approximately 15–20% improvement in the SNR — quite significant considering the majority of the sources under discussion have instrumental SNR of about 4σ (see Table 1)! The improvement is less impressive in the LESS 870 μm image, since the instrumental noise dominates the RMS resulting from confusion. Most previous studies of SMGs in the regime where confusion is important have extracted sources using the PSF, and our results show that they have smoothed away some of the point source information in the maps.

APPENDIX B: LIKELIHOOD RATIOS

Here we describe our formulation of Likelihood Ratios (LR) as a means for identifying counterparts to submm-selected sources. The matching catalogue for which we estimate priors is described in Section 2.2. To begin, we make two basic assumptions: (i) that the radial offset of a potential ID is uncorrelated with its other properties; and (ii) that the submm flux density is uncorrelated with its other properties. The first assumption is fairly standard and uncontroversial, although the latter could be considered problematic. For example, the brightest sources at 250 μm are known to be low-luminosity *IRAS* galaxies, whereas the fainter sources are thought to be a mixture of both low- and high-redshift galaxies. However, for now we take the practical route and choose not to make any distinction based on these properties so that we can estimate priors with reasonable SNR given the data. We then express the differential density *of true counterparts* to submm sources as a function of their offsets, r, flux densities, s (both at 24 μm and 1.4 GHz), and colour c (IRAC [3.6] − [4.5]):

$$n_{\rm c}(s,c,r)ds\,dc\,dr = q(s,c)f(r)ds\,dc\,dr, \qquad \text{(B1)}$$

where $q(s,c)$ is the distribution of counterpart flux densities and colours (in the matching catalogue), and $f(r)$ is the positional probability distribution as a function of radial offset r. We assume a Gaussian radial positional probability distribution

$$f(r) = \frac{r}{\sigma_{\rm r}^2} e^{-r^2/2\sigma_{\rm r}^2}, \qquad \text{(B2)}$$

which is normalized so that $\int_0^\infty f(r)dr = 1$. Following Sutherland & Saunders (1992) $q(s,c)$ is normalized so that it integrates to *the average expected number of counterparts per submm source*. However, while those authors assumed that this number is in the range 0–1 (i.e., the emission is produced by a *single* source, which may or may not be present in the matching catalogue), we consider cases in which the number of counterparts may be greater than this.

We can also estimate the differential density of background sources as a function of these same properties

$$n_{\rm b}(s,c,r)ds\,dc\,dr = 2\pi r\rho(s,c)ds\,dc\,dr, \qquad \text{(B3)}$$

where $\rho(s,c)$ is the surface density of background sources as a function of s and c, and multiplying by $2\pi r$ converts this quantity to the infinitesimal number density of sources at a distance r from the submm position.

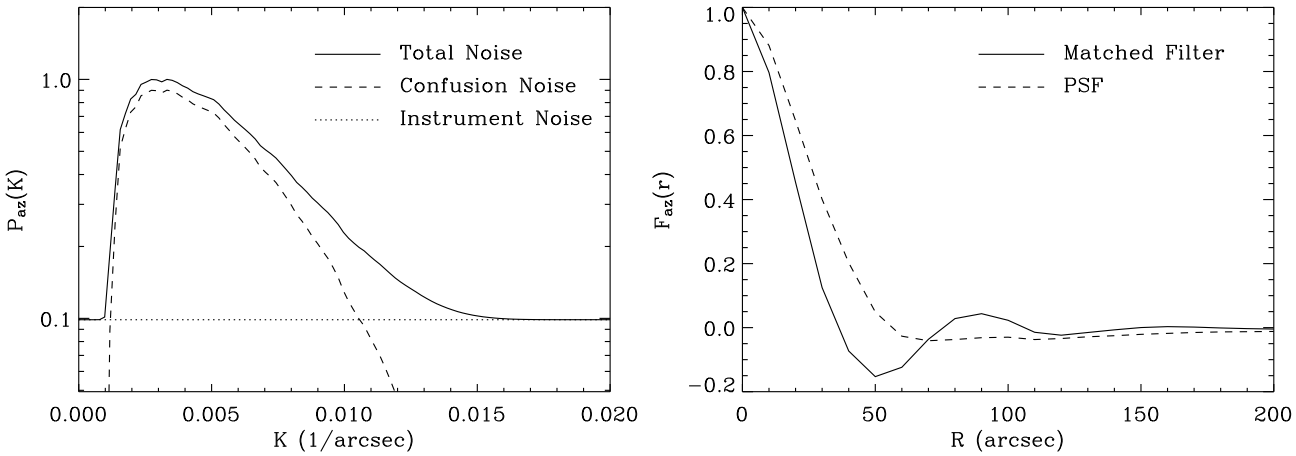

Figure A1. *left:* The peak-normalized total azimuthally averaged 500 μm angular noise power spectrum (solid line) and its two components: instrumental (white) noise (dotted line), and confusion from point sources (dashed line). The latter function has the same shape as the PSF, since point sources are modelled as a spatially unclustered collection of point sources smoothed by the PSF. The roll-off at $K < 0.003$ in the PSF is a result of the spatial whitening filter that has been applied to the BLAST maps (Devlin et al. 2009). *right:* The azimuthally averaged 500 μm matched filter (solid line) compared with the PSF (dashed line), now in angular rather than frequency space. The matched filter is obtained by dividing the power spectrum of the PSF (same shape as the dashed line in the left-hand plot) by the noise power spectrum (solid line in the left-hand plot), and taking the inverse Fourier Transform. For the noise sources considered here, this procedure augments high-frequency components of the PSF, resulting in a narrower central profile, while introducing ringing at angular scales $\gtrsim 50$ arcsec.

Therefore, given s, c and r for the jth candidate counterpart to the ith submm source, the relative number of expected true counterparts to background sources is the LR:

$$L_{i,j} = \frac{n_{\rm c}}{n_{\rm b}} = \frac{q(s_j, c_j) e^{-r_{i,j}^2/2\sigma_{\rm r}^2}}{2\pi\sigma_{\rm r}^2 \rho(s_j, c_j)}. \quad \text{(B4)}$$

Candidates with large values of $L_{i,j}$ are the most likely to be associated with the submm emission.

Note that while the LR contains all of the information about the potential identification, it is not itself a probability distribution. In the case that only a single source in the matching catalogue is believed to correspond to the submm source, and where $q(s, c)$, $\rho(s, c)$, and σ are all known precisely, it is possible to calculate the reliability R, the probability that the candidate is *the unique counterpart*, following Sutherland & Saunders (1992). However, since we consider the possibility of multiple counterparts to a single submm source, and since our estimates of the priors are ultimately quite noisy, Eq. 5 from Sutherland & Saunders (1992) does not apply. Instead we will take the approach of using Monte Carlo simulations to establish a threshold LR that will provide candidates with a desired false identification rate.

B1 Background Counts and Positional Uncertainties

We estimate priors directly from the data themselves. First, $\rho(s, c)$, the background number counts, are determined by binning the entire matching catalogue (Section 2.2) as a function of the two flux densities and colour, and dividing by the survey area. This should give a good estimate for the average properties of the background sources since the entire catalogue contains 9216 entries, whereas there are only of order ~ 60 submm sources in each band.

The positional uncertainty parameter, $\sigma_{\rm r}$, is more difficult to estimate from the data. We proceed by counting the number of catalogue sources centred over submm positions, and checking for statistically significant excesses compared to the background counts predicted by $\rho(s, c)$, as a function of search radius. The expectation, if each submm source were produced by a single source in the matching catalogue, is that the excess would grow from 0 at a search radius of 0, and converge to 1 at large radii.

This radial excess distributions (calculated in annuli of different sizes) are shown for each submm band in Fig. B1. Uncertainties for each data point are estimated from Poisson counting statistics. We fit a Gaussian positional offset distribution to the excess counts, multiplying the single-parameter expression for $f(r)$ in Eq. B2 by a second parameter, E, giving the total excess number of sources around submm positions (note that $E = \int\int q(s, c) ds dc$). The smooth models are shown as solid lines in the differential excess plots. In addition, the solid histograms show the models integrated across the same bins as the data, giving the model predictions used to calculate χ^2. Clearly, E is significantly larger than 1 in each submm band, demonstrating that the submm sources from our survey are typically blends of several sources in the matching catalogue. One could use this approach to determine a criterion which might be called 'counterpart confusion' – for a given source map and catalogue (in a different waveband) one could conclude that the source identification process will be relatively straightforward if $E < 2$ (say), but significantly complicated by confusion if $E \geqslant 2$.

B2 Flux density and colour priors

Next we estimate the joint distribution of flux density and colour for counterparts, $q(s, c)$. Since we assume that these

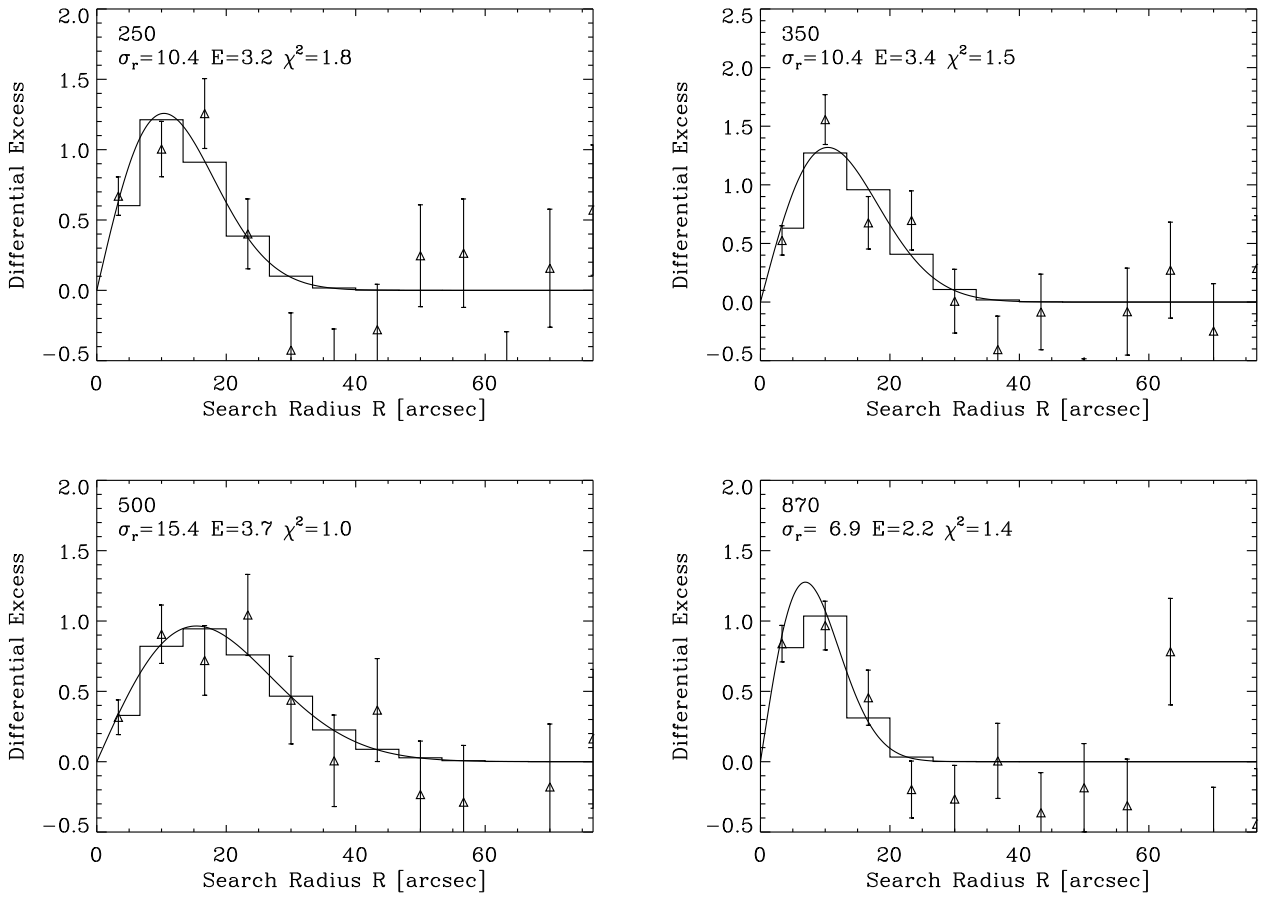

Figure B1. Excess source counts in annuli around submm positions compared to the expected background as a function of search radius. Poisson uncertainties are plotted. The solid lines are fits of a Gaussian radial probability density function $p(r) = (Er/\sigma_{\rm r})\exp(-r^2/2\sigma_{\rm r}^2)$, where the scale factor E is the total excess counts encountered on average (fit values are indicated in each panel). This function is fit to the differential excess counts (since the uncertainties are uncorrelated). The histograms in the differential plots show the smooth model integrated across each bin (giving the actual predicted model values used to calculate $\chi^2_{\rm r}$).

properties are un-correlated with their distance from the submm centroid, we first identify the search radius within which the SNR of the excess counts is highest, $r_{\rm s}$. As this radius is increased from 0, the background counts grow as $r_{\rm s}^2$, but the counts around submm positions grow even faster as the counterparts are included. The ratio of the difference (the excess), compared to the Poisson uncertainty in the difference, therefore increases until the number of new counterparts drops significantly. We find that for our matching catalogue and submm source lists the maximum excess SNR are achieved at 23, 23, 35 and 15 arcsec for 250, 350, 500 and 870 μm, respectively. Using these search radii, we then compare the normalized histogram of 24 μm and 1.4 GHz flux densities for the entire matching catalogues with the normalized histogram of excess sources around submm positions, $p(s_{24})$ and $p(s_{\rm r})$, in Figs. B2 and B3. This operation shows that the extra sources around submm positions tend to be *brighter* at 24 μm and 1.4 GHz on average than the entire populations in the BLAST bands.

In a similar way we compare the $\log_{10}(s_{3.6}/s_{4.5})$ colour of the background population to the excess around submm positions. This colour was chosen because it is the primary discriminator for redshift used in Devlin et al. (2009), Marsden et al. (2009), and Pascale et al. (2009) – with the trend that smaller ratios (i.e. redder colours) correlate with higher-redshifts. Earlier studies have also used IRAC colours as a crude redshift estimator (e.g., Pope et al. 2006; Yun et al. 2008; Wilson et al. 2008). The normalized excess colour distribution, $p(c)$ (Fig. B4) agrees with this expectation. There is a trend from bluer colours starting at 250 μm (submm excess and background colours nearly indistinguishable), to significantly redder colours at 500 and 870 micron.

Individually, $p(s_{24})$, $p(s_{\rm r})$, and $p(c)$ give normalized estimates of $q(s_{24}, s_{\rm r}, c)$ marginalized over the remaining variables. If they were completely independent of one another, we could estimate $q(s, c)$ as

$$q(s, c) = E \times p(s_{24})p(s_{\rm r})p(c), \qquad \text{(B5)}$$

where E is the total excess measured in Fig. B1. Ideally we would like to bin the excess counts in cubes of s_{24}, $s_{\rm r}$, and c simultaneously. Unfortunately, given the sample size, it is not possible to obtain a statistically significant measurement of this distribution. We therefore proceed under the assumption that these quantities are independent, but in the next section use Monte Carlo simulations to establish

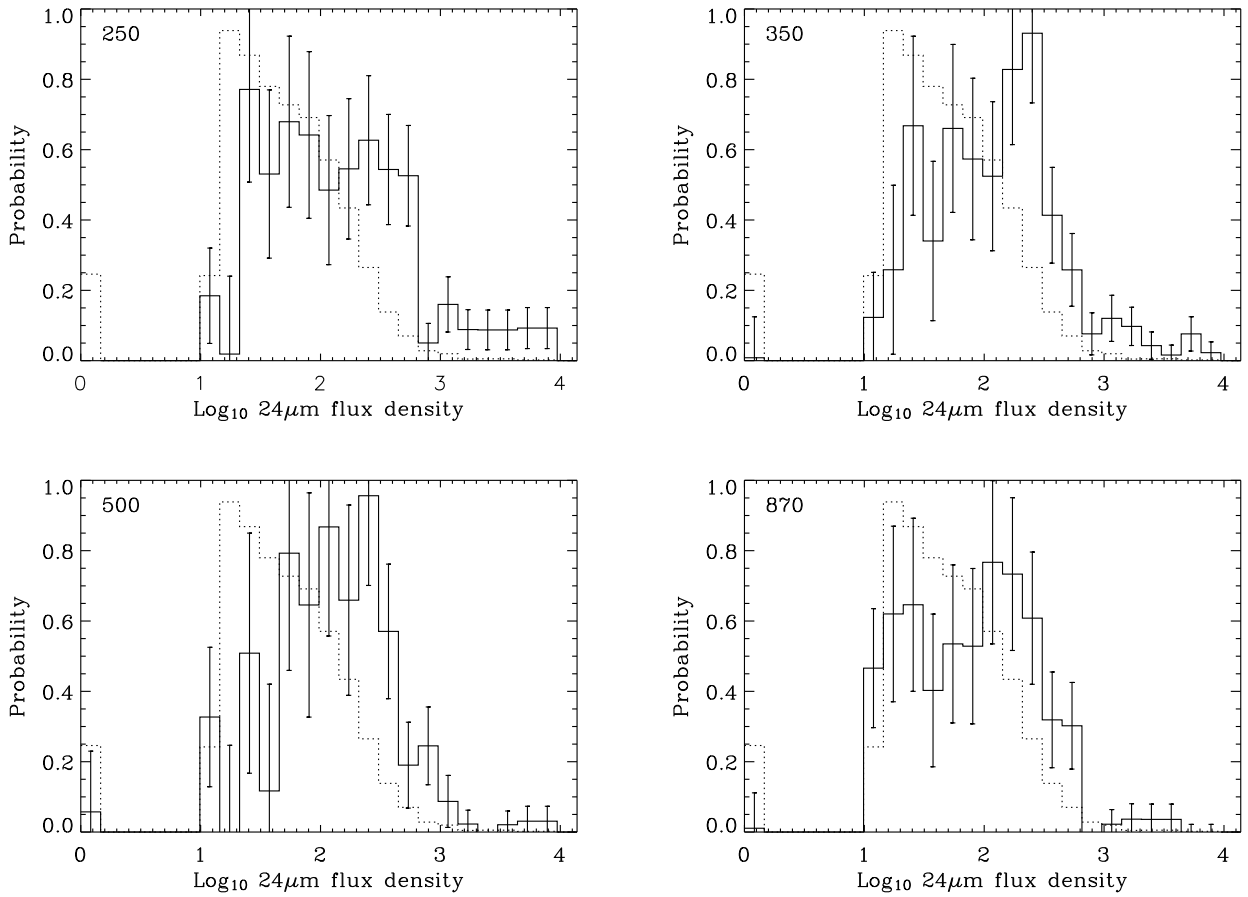

Figure B2. MIPS 24 μm flux density distributions of excess sources around submm positions in all four bands (solid histogram with Poisson uncertainties) compared to the general population (dotted histogram). The bin at 0 contains all radio sources that are not present in the FIDEL 24 μm catalogue. Galaxies selected near submm positions are on average brighter at 24 μm than galaxies selected randomly, and this is true for all four bands.

a reasonable threshold for this approximate LR to obtain counterparts.

B3 Normalized LR

Since each submm source appears to be produced by a blend of several matching catalogue sources, we cannot use the Sutherland & Saunders (1992) reliability, R, as a normalized probability that a given candidate is *the single* counterpart. Furthermore, its absolute normalization depends on precise measurements of σ_r, $\rho(s,c)$ and $q(s,c)$, all of which have moderate uncertainties for this sample (especially $q(s,c)$, as noted in the previous section).

Instead, we compare the LRs for all potential candidate matches to submm sources, with the distribution of LRs for false matches to random positions. This procedure enables us to select a threshold LR that gives an acceptable rate of false-positives, which we set to 10%. This approach to identifying the threshold LR is similar to that of Mann et al. (1997). The results of our calculation are shown in Fig. B5. The solid histogram shows the distribution of LR for all matching catalogue sources out to 60 arcsec (this maximum search radius easily contains > 99% of the true counterparts) from each submm position. The dotted histograms show the 'background' distribution obtained by searching for counterparts around random positions. As expected, for large values of the LR, there are more sources around submm positions than random positions. Also, unsurprisingly, the distinction between the two curves is greatest at 870 μm (which has the smallest positional uncertainties), and progressively worse across the BLAST bands to longer wavelengths.

A threshold in the LR is chosen such that the fraction of sources with *larger* LR for the simulation (random positions) is 10%. This cut is indicated as a vertical dashed line in Fig. B5. The results of applying this cut to potential identifications around submm positions are given in Table 2. For each band the total number of expected counterparts is the product of the number of submm positions with the average excess of matching catalogue sources around each spot. The estimated number of true IDs found is then the number of sources detected above the cut on the LR, after subtracting the 10% spurious fraction. This test shows that as many as 32% of the individual matching catalogue sources contributing to the 870 μm sources have been identified, and as few as 13% at 500 μm. The trend of this result is certainly expected, due to the increased confusion caused by larger

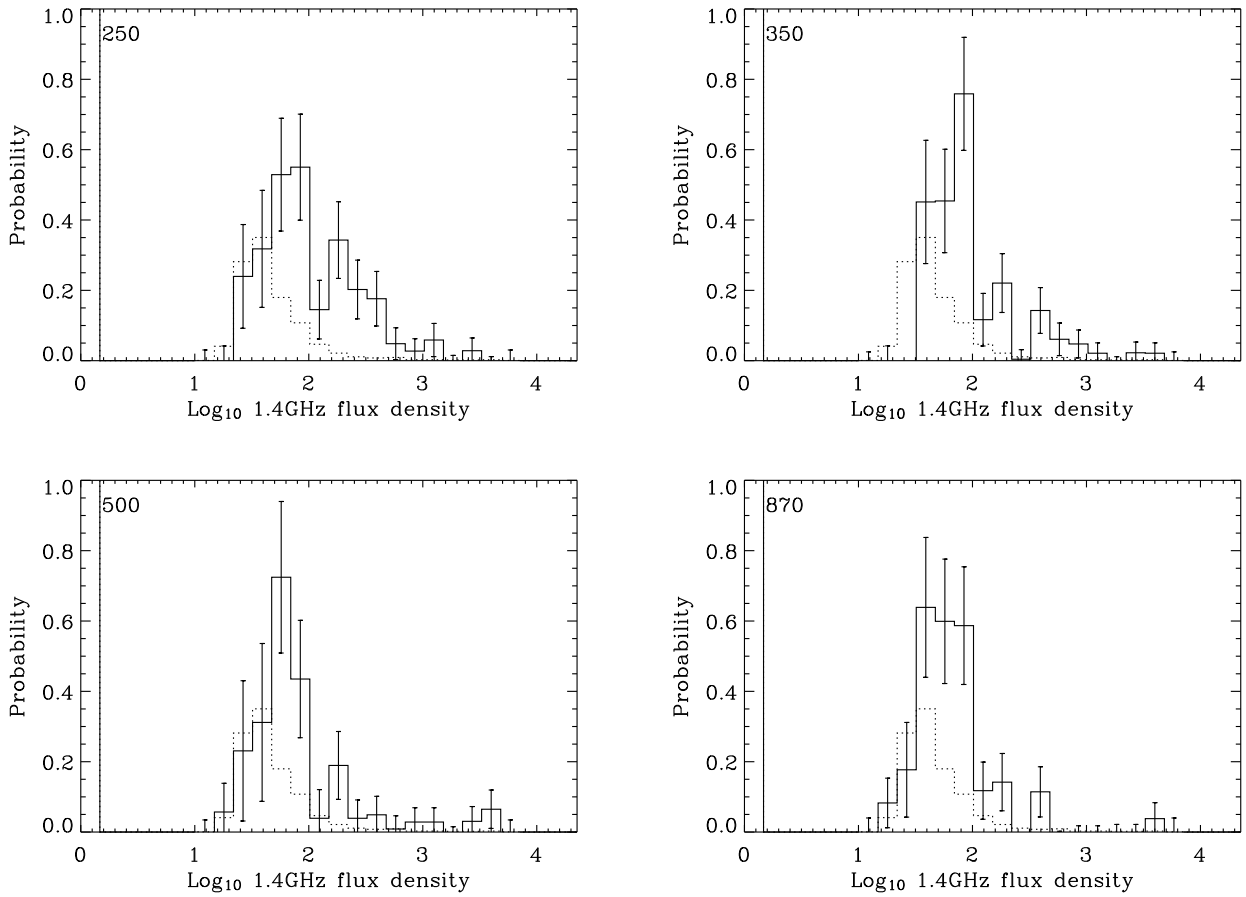

Figure B3. VLA 1.4 GHz flux density distributions of excess sources around submm positions in all four bands (solid histogram with Poisson uncertainties) compared to the general population (dotted histogram). The bin at 0 contains all 24 µm FIDEL sources that do not exhibit significant radio flux. Galaxies selected near submm positions are on average brighter at 1.4 GHz than galaxies selected randomly, and this is true for all four bands. We also note that many more of the radio sources with 24 µm emission are found near submm positions than random radio sources. Many of these radio sources without 24 µm emission could be spurious given the low signficance cut on the catalogue that has been used (see Section 2.2.2). Our prior estimation procedure will give much greater weight to potential radio identifications that also exhibit 24 µm emission.

beams. However, the extent of the problem of identifying confused sources is larger than some would have expected.

APPENDIX C: DATA TABLES

The following data tables are provided in this Appendix: the match-filtered submm source lists in the BLAST bands (Tables C1-C3), as well as the LESS sources from Weiss et al. (2009) that land within the region that was analyzed (Table C4); the correspondance between the matching catalogue and each of the submm lists (Table C5); and the properties of the matched sources (re-measured submm flux densities, SED fits and redshifts, Table C6).

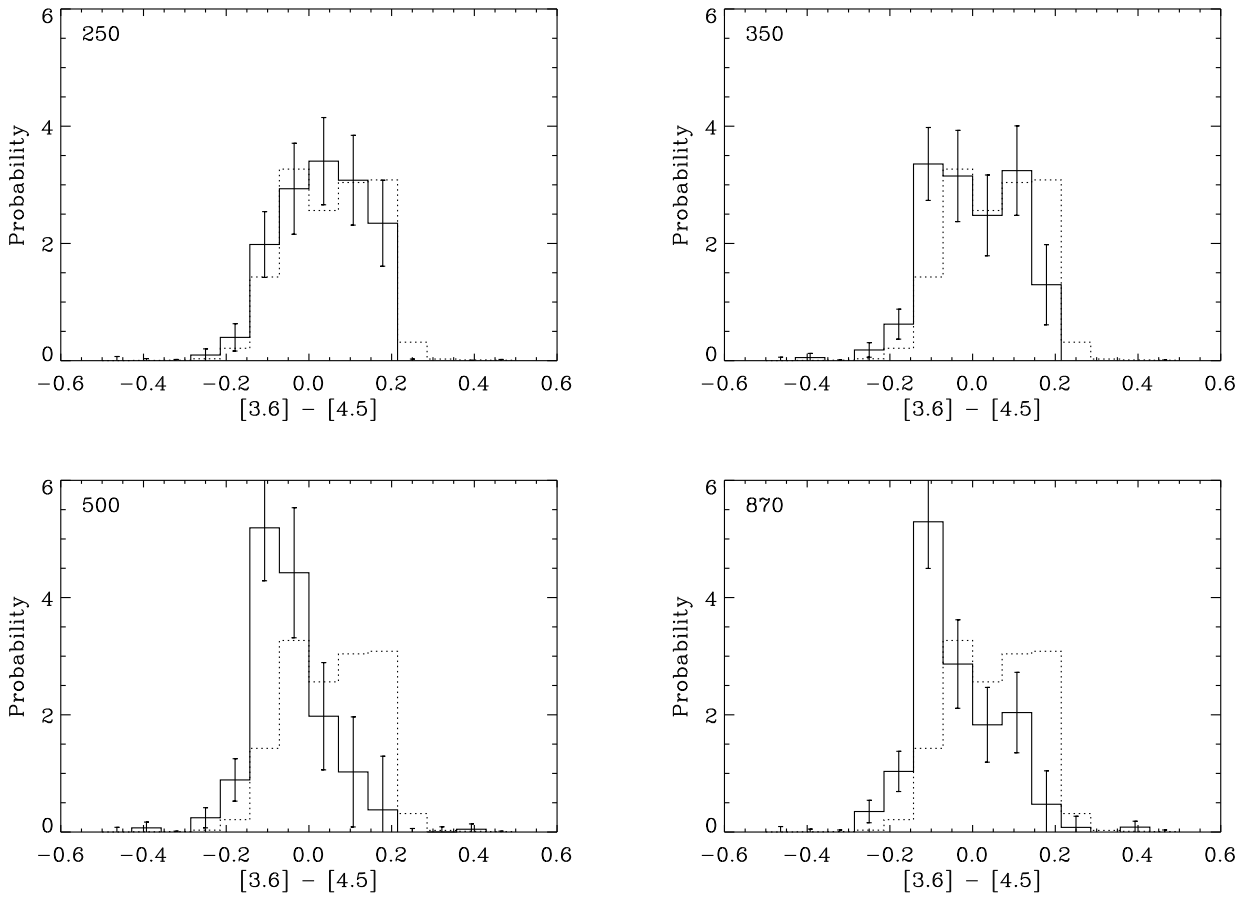

Figure B4. IRAC $\log_{10}(s_{3.6}/s_{4.5})$ colour distributions of excess matching catalogue sources around submm positions in all four bands (solid histogram with Poisson uncertainties) compared to the general population (dotted histogram). There is a clear trend of redder colours in the IRAC bands for galaxies selected at longer submm wavelengths.

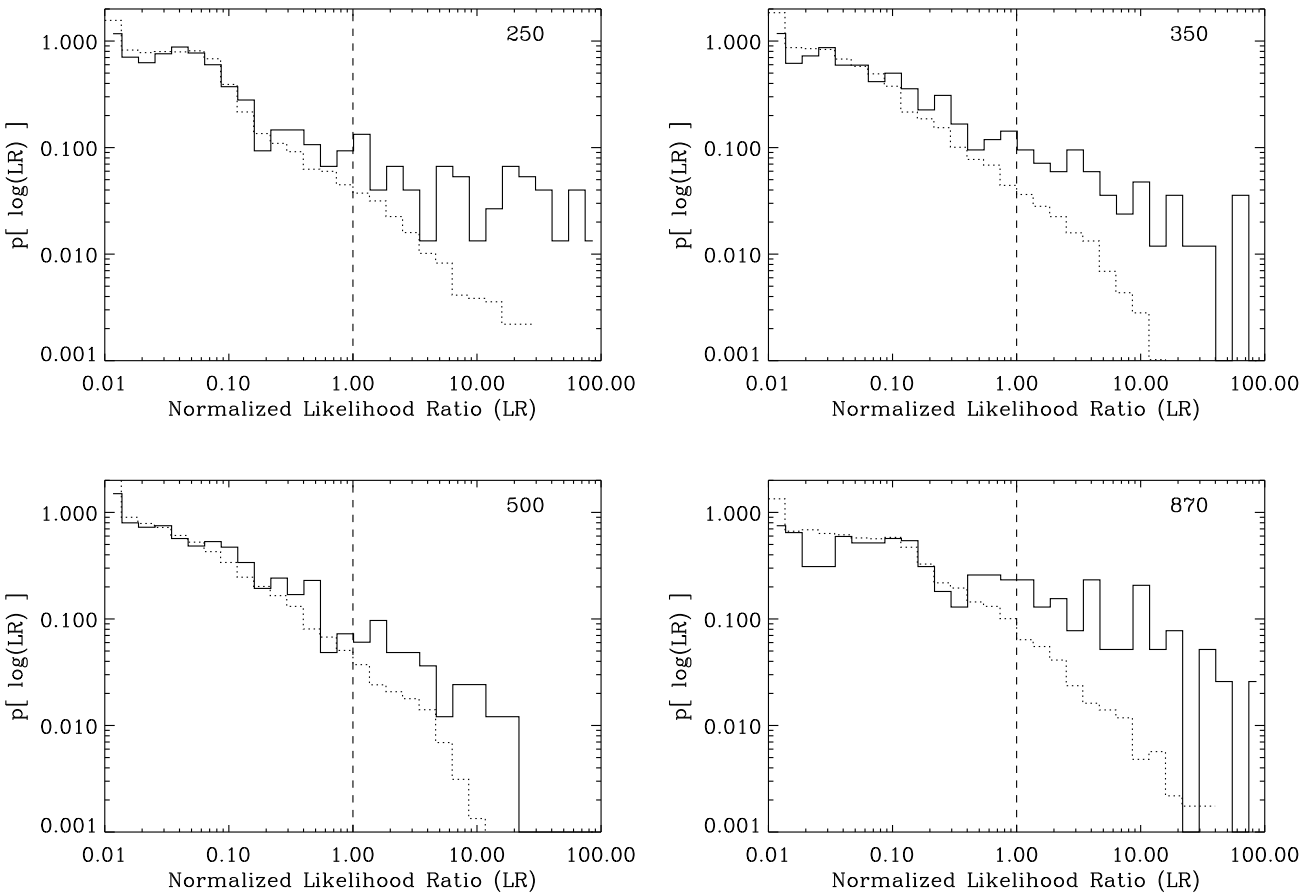

Figure B5. Distribution of likelihood ratios (LR) for potential counterparts in the matching catalogue out to 60 arcsec from submm source positions (solid histograms) compared to random positions (dotted histograms). Thresholds for identifying potential counterparts are given by the vertical dashed lines, such that the integrated tail of the distribution for random positions gives a false positive rate of 10%. All LRs are normalized to this value (i.e., potential IDs with LR > 1.00 have less than a 10% chance of being false).

Table C1. 250 μm source list produced from matched-filtered maps that land within the coverage of the matching catalogue (Figure 2). The 'Previously Published Name' is taken from the supplement to Devlin et al. (2009) when available (new sources have no entry in this column), but the short submm 'SID' is used throughout this paper. The 'Match' column refers to IDs in Table C5. The positions are centroids of the submm sources. The flux densities are raw values from the maps (with no correction for flux boosting), and the noises and SNR refer to instrumental noise only (excluding source confusion).

SID 250	Previously Published Name	Match ID	R.A. (^{h} ^{m} ^{s})	Dec. ($^\circ$ $'$ $''$)	Flux Density (mJy)	SNR
3	BLAST J033235−275530 (250μm)	69	03 32 34.99	−27 55 31.1	196 ± 14	13.93
5	BLAST J033229−274414 (250μm)	64,65	03 32 29.66	−27 44 16.3	162 ± 13	11.62
16	BLAST J033129−275722 (250μm)	10,11	03 31 29.94	−27 57 24.1	112 ± 14	7.93
17	BLAST J033249−275842 (250μm)	89	03 32 49.32	−27 58 41.5	104 ± 14	7.41
24	BLAST J033246−275744 (250μm)	84	03 32 46.05	−27 57 45.0	99 ± 14	7.11
27	BLAST J033258−274322 (250μm)	95	03 32 58.31	−27 43 24.9	97 ± 14	6.79
32	BLAST J033145−274635 (250μm)	26	03 31 45.37	−27 46 36.6	87 ± 14	6.21
36	BLAST J033145−275730 (250μm)	27	03 31 45.86	−27 57 29.0	84 ± 14	5.96
38	BLAST J033217−275905 (250μm)	55,56	03 32 17.07	−27 59 06.9	83 ± 14	5.91
45	BLAST J033221−275630 (250μm)	60	03 32 21.77	−27 56 26.0	79 ± 14	5.65
51	BLAST J033152−273931 (250μm)	34,35	03 31 52.57	−27 39 33.1	76 ± 14	5.40
52	BLAST J033308−274805 (250μm)	104,105,106,107,108	03 33 08.62	−27 48 04.5	74 ± 13	5.37
54	BLAST J033318−274610 (250μm)	118,119	03 33 17.83	−27 46 08.5	74 ± 14	5.32
57	BLAST J033145−274205 (250μm)	25	03 31 44.99	−27 42 06.4	74 ± 14	5.19
58	BLAST J033218−275216 (250μm)	58,59	03 32 18.01	−27 52 18.7	72 ± 14	5.16
59	BLAST J033149−274335 (250μm)	30	03 31 49.74	−27 43 34.7	72 ± 14	5.14
60	BLAST J033241−273818 (250μm)	76,77,78	03 32 41.87	−27 38 17.9	72 ± 14	5.06
67	BLAST J033319−275423 (250μm)	123	03 33 19.03	−27 54 23.7	70 ± 14	4.98
69	BLAST J033237−273527 (250μm)	73,74	03 32 37.78	−27 35 43.6	69 ± 14	4.95
70	BLAST J033135−273933 (250μm)	12	03 31 35.75	−27 39 44.2	70 ± 14	4.94
72	BLAST J033316−275043 (250μm)	115	03 33 16.20	−27 50 39.6	68 ± 13	4.94
75	BLAST J033205−274645 (250μm)	45	03 32 05.14	−27 46 45.6	68 ± 14	4.91
78		1	03 31 27.89	−27 44 49.5	68 ± 14	4.86
80	BLAST J033128−273916 (250μm)	2,4,5	03 31 29.06	−27 39 05.2	68 ± 14	4.81
82	BLAST J033243−273919 (250μm)	81	03 32 43.61	−27 39 20.5	67 ± 14	4.79
85	BLAST J033141−274439 (250μm)	19,20	03 31 41.15	−27 44 38.0	67 ± 14	4.75
91	BLAST J033223−273642 (250μm)	62	03 32 22.81	−27 36 43.4	66 ± 14	4.72
92	BLAST J033140−275633 (250μm)	18	03 31 40.33	−27 56 36.3	66 ± 14	4.70
93	BLAST J033211−275859 (250μm)		03 32 11.86	−27 59 00.8	66 ± 14	4.70
97	BLAST J033222−280019 (250μm)	61	03 32 22.14	−28 00 21.1	65 ± 13	4.66
99	BLAST J033129−275910 (250μm)	9	03 31 29.19	−27 59 11.1	66 ± 14	4.64
111	BLAST J033130−275604 (250μm)	7,8	03 31 29.99	−27 56 02.1	63 ± 14	4.53
112		66	03 32 29.95	−27 43 14.4	64 ± 14	4.52
113	BLAST J033235−274932 (250μm)	70	03 32 35.24	−27 49 28.2	62 ± 13	4.51
121	BLAST J033230−275905 (250μm)	67,68	03 32 30.17	−27 59 05.9	63 ± 14	4.44
130	BLAST J033259−273535 (250μm)	97	03 32 59.71	−27 35 33.4	61 ± 14	4.37
146	BLAST J033151−274431 (250μm)	31,32	03 31 51.13	−27 44 38.1	60 ± 13	4.29
151	BLAST J033147−274147 (250μm)		03 31 47.89	−27 41 41.2	60 ± 14	4.27
154			03 32 06.88	−27 38 00.7	60 ± 14	4.25
178	BLAST J033232−275304 (250μm)		03 32 33.03	−27 53 04.8	59 ± 14	4.18
185	BLAST J033317−274118 (250μm)	116	03 33 17.38	−27 41 12.5	59 ± 14	4.15
188	BLAST J033154−274406 (250μm)	41	03 31 54.28	−27 44 04.2	58 ± 14	4.15

SID 250	Previously Published Name	Match ID	R.A. (^{h} ^{m} ^{s})	Dec. ($^\circ$ $'$ $''$)	Flux Density (mJy)	SNR
210	BLAST J033135−274705 (250μm)		03 31 35.03	−27 47 09.1	57 ± 14	4.09
222	BLAST J033200−280234 (250μm)		03 32 00.67	−28 02 32.1	57 ± 14	4.06
226	BLAST J033128−273916 (250μm)	3,4	03 31 29.94	−27 39 41.9	58 ± 14	4.05
235	BLAST J033156−280306 (250μm)		03 31 56.85	−28 03 09.4	57 ± 14	4.03
244		17	03 31 39.58	−27 41 29.5	56 ± 14	4.00
246	BLAST J033211−280242 (250μm)	48	03 32 11.14	−28 02 42.6	56 ± 14	4.00
250	BLAST J033251−274530 (250μm)		03 32 51.55	−27 45 33.3	56 ± 14	3.99
255	BLAST J033144−275521 (250μm)	24	03 31 44.76	−27 55 19.5	55 ± 13	3.98
279	BLAST J033311−274313 (250μm)		03 33 11.13	−27 43 12.0	56 ± 14	3.93
289	BLAST J033217−275054 (250μm)	57	03 32 17.43	−27 50 55.7	54 ± 13	3.91
298	BLAST J033243−275146 (250μm)	82,83	03 32 43.50	−27 51 45.6	54 ± 14	3.89
312	BLAST J033228−273545 (250μm)		03 32 28.66	−27 35 53.0	54 ± 14	3.86
316	BLAST J033238−275651 (250μm)	75	03 32 37.99	−27 56 57.6	53 ± 13	3.86
325	BLAST J033225−273822 (250μm)	63	03 32 24.97	−27 38 22.2	54 ± 14	3.84
328	BLAST J033205−280054 (250μm)	44	03 32 05.54	−28 00 54.2	53 ± 13	3.84
348	BLAST J033150−275100 (250μm)		03 31 50.24	−27 51 11.0	53 ± 13	3.81
354	BLAST J033248−274443 (250μm)		03 32 47.55	−27 44 58.3	53 ± 14	3.80
358	BLAST J033210−274253 (250μm)	50,51	03 32 10.51	−27 42 55.3	53 ± 14	3.80
369		90	03 32 49.09	−27 36 19.7	53 ± 14	3.78
378	BLAST J033131−274601 (250μm)		03 31 31.77	−27 46 05.1	52 ± 14	3.76
381	BLAST J033311−275226 (250μm)		03 33 11.65	−27 52 27.0	52 ± 13	3.76
389	BLAST J033251−275936 (250μm)	91	03 32 51.85	−27 59 40.9	53 ± 14	3.75

Table C2. 350 μm source list produced from matched-filtered maps. Columns have the same meaning as in Table C1.

SID 350	Previously Published Name	Match ID	R.A. (h m s)	Dec. (° ′ ″)	Flux Density (mJy)	SNR
3	BLAST J033234−275531 (350μm)	69	03 32 34.88	−27 55 31.3	89 ± 10	8.24
7	BLAST J033249−275833 (350μm)	89	03 32 49.49	−27 58 33.8	79 ± 10	7.36
8	BLAST J033229−274414 (350μm)	64,65	03 32 29.37	−27 44 16.4	74 ± 10	6.95
10	BLAST J033220−275647 (350μm)	60	03 32 20.15	−27 56 45.4	73 ± 10	6.82
11	BLAST J033258−274328 (350μm)	95	03 32 58.39	−27 43 25.0	72 ± 10	6.73
12	BLAST J033229−274305 (350μm)	66	03 32 29.49	−27 43 03.4	71 ± 10	6.72
14	BLAST J033328−275700 (350μm)	125	03 33 27.65	−27 57 03.4	72 ± 10	6.66
16	BLAST J033129−275722 (350μm)	10,11	03 31 29.61	−27 57 22.6	70 ± 11	6.41
19	BLAST J033204−274650 (350μm)	45	03 32 04.59	−27 46 51.7	67 ± 10	6.35
20	BLAST J033207−275815 (350μm)	47	03 32 07.34	−27 58 18.1	68 ± 10	6.30
22	BLAST J033128−273927 (350μm)	2,3,4,5	03 31 28.02	−27 39 32.2	71 ± 11	6.25
31	BLAST J033311−274135 (350μm)	111	03 33 11.16	−27 41 32.5	64 ± 10	5.95
34	BLAST J033247−274224 (350μm)	86,87,88	03 32 47.24	−27 42 31.9	62 ± 10	5.86
35	BLAST J033150−274333 (350μm)	30	03 31 49.77	−27 43 28.2	63 ± 10	5.84
37	BLAST J033140−274435 (350μm)	19,20	03 31 40.71	−27 44 36.9	62 ± 10	5.76
42	BLAST J033138−274122 (350μm)	17	03 31 39.04	−27 41 22.3	60 ± 10	5.67
43	BLAST J033318−274606 (350μm)	118,119	03 33 18.39	−27 46 13.4	60 ± 10	5.64
45	BLAST J033210−275206 (350μm)	49	03 32 11.53	−27 52 03.8	61 ± 10	5.62
47	BLAST J033151−274428 (350μm)	31,32	03 31 51.20	−27 44 33.4	59 ± 10	5.56
49	BLAST J033135−275448 (350μm)	13,14,15,16	03 31 35.44	−27 54 47.5	60 ± 10	5.56
52	BLAST J033252−273756 (350μm)	93	03 32 52.12	−27 37 47.9	58 ± 10	5.36
58	BLAST J033321−275513 (350μm)	124	03 33 21.74	−27 55 13.1	56 ± 10	5.19
64	BLAST J033302−275640 (350μm)	98	03 33 02.20	−27 56 43.7	54 ± 10	5.05
65	BLAST J033218−275207 (350μm)	58,59	03 32 18.12	−27 52 12.5	54 ± 10	5.03
69	BLAST J033237−273541 (350μm)	73,74	03 32 37.62	−27 35 42.4	54 ± 11	4.96
79	BLAST J033307−275833 (350μm)	101	03 33 06.98	−27 58 35.5	52 ± 10	4.84
80	BLAST J033217−275906 (350μm)	56	03 32 17.78	−27 59 20.2	52 ± 10	4.83
84	BLAST J033318−274131 (350μm)		03 33 19.72	−27 41 38.7	52 ± 10	4.79
85	BLAST J033230−275905 (350μm)	67,68	03 32 30.00	−27 59 02.4	51 ± 10	4.79
88	BLAST J033211−273731 (350μm)	52	03 32 11.34	−27 37 24.1	51 ± 10	4.76
90	BLAST J033253−280107 (350μm)	92	03 32 53.05	−28 01 11.3	51 ± 10	4.76
91	BLAST J033321−273908 (350μm)		03 33 21.00	−27 39 10.0	51 ± 10	4.75
92	BLAST J033308−275130 (350μm)	109	03 33 08.61	−27 51 29.3	50 ± 10	4.74
93	BLAST J033153−274952 (350μm)	40	03 31 54.84	−27 49 37.7	51 ± 10	4.73
95	BLAST J033152−280325 (350μm)	33	03 31 53.14	−28 03 35.7	51 ± 10	4.72
98		114	03 33 15.41	−27 45 32.9	50 ± 10	4.69
108	BLAST J033215−273929 (350μm)	54	03 32 15.25	−27 39 31.8	50 ± 10	4.62
112	BLAST J033316−275056 (350μm)	115	03 33 17.16	−27 50 55.7	48 ± 10	4.60
115	BLAST J033305−274414 (350μm)	99,100	03 33 06.26	−27 44 14.1	49 ± 10	4.59
116	BLAST J033245−275739 (350μm)	84	03 32 46.04	−27 57 35.2	49 ± 10	4.59
117	BLAST J033134−274629 (350μm)		03 31 34.56	−27 46 25.9	49 ± 10	4.57
124	BLAST J033153−273931 (350μm)	34,35	03 31 52.62	−27 39 29.9	49 ± 10	4.54

SID 350	Previously Published Name	Match ID	R.A. (^{h} ^{m} ^{s})	Dec. ($^\circ$ $'$ $''$)	Flux Density (mJy)	SNR
128	BLAST J033243−275509 (350μm)	79,80	03 32 42.86	−27 55 13.1	48 ± 10	4.51
137	BLAST J033217−275906 (350μm)	55,56	03 32 17.89	−27 58 46.5	47 ± 10	4.44
144	BLAST J033152−275035 (350μm)		03 31 51.22	−27 50 41.8	46 ± 10	4.40
145	BLAST J033308−274813 (350μm)	104,105,106,107,108	03 33 08.49	−27 48 16.5	47 ± 10	4.40
152	BLAST J033145−274153 (350μm)	25	03 31 44.98	−27 41 50.5	46 ± 10	4.32
154	BLAST J033238−274620 (350μm)		03 32 38.52	−27 46 18.5	46 ± 10	4.32
161	BLAST J033212−275459 (350μm)		03 32 12.74	−27 54 59.1	45 ± 10	4.29
169	BLAST J033225−273810 (350μm)	63	03 32 24.93	−27 38 17.3	46 ± 10	4.25
170	BLAST J033201−274142 (350μm)	43	03 32 02.02	−27 41 38.0	45 ± 10	4.25
177	BLAST J033129−275911 (350μm)	9	03 31 29.63	−27 59 09.1	46 ± 10	4.22
184			03 32 10.66	−27 58 56.9	45 ± 10	4.21
187	BLAST J033141−275529 (350μm)	23,24	03 31 41.76	−27 55 28.4	44 ± 10	4.18
188	BLAST J033147−274755 (350μm)	28	03 31 47.60	−27 47 52.9	45 ± 10	4.18
199	BLAST J033217−275407 (350μm)		03 32 17.92	−27 54 08.0	44 ± 10	4.13
235	BLAST J033127−274430 (350μm)	1	03 31 27.90	−27 44 32.8	43 ± 10	4.04
259	BLAST J033235−280135 (350μm)	71,72	03 32 35.90	−28 01 48.7	42 ± 10	3.97
264	BLAST J033210−275612 (350μm)		03 32 11.27	−27 56 12.1	42 ± 10	3.96
273	BLAST J033234−280043 (350μm)		03 32 34.46	−28 00 36.3	42 ± 10	3.94
276	BLAST J033313−273709 (350μm)		03 33 13.26	−27 37 14.9	43 ± 10	3.93
291	BLAST J033136−274933 (350μm)		03 31 36.08	−27 49 40.9	41 ± 10	3.89
298	BLAST J033312−275611 (350μm)	112,113	03 33 13.37	−27 56 04.2	41 ± 10	3.88
317			03 32 29.08	−28 01 53.8	41 ± 10	3.84
322	BLAST J033148−280212 (350μm)	29	03 31 48.41	−28 02 20.9	41 ± 10	3.83
340	BLAST J033132−274314 (350μm)		03 31 32.37	−27 43 16.5	41 ± 10	3.80
362			03 33 04.96	−27 37 26.0	40 ± 10	3.76

Table C3. 500 μm source list produced from matched-filtered maps. Columns have the same meaning as in Table C1.

SID 500	Previously Published Name	Match ID	R.A. (h m s)	Dec. (° ′ ″)	Flux Density (mJy)	SNR
5	BLAST J033328−275659 (500μm)	125	03 33 28.17	−27 56 57.0	62 ± 8	7.43
7	BLAST J033311−275610 (500μm)	110,112,113	03 33 11.77	−27 56 11.2	56 ± 8	6.81
8	BLAST J033207−275811 (500μm)	47	03 32 08.12	−27 58 05.0	53 ± 8	6.51
9	BLAST J033129−275545 (500μm)	6,7,8	03 31 29.24	−27 55 49.0	53 ± 8	6.41
11	BLAST J033128−275713 (500μm)	10,11	03 31 29.51	−27 57 22.0	53 ± 8	6.28
12	BLAST J033258−274325 (500μm)	95	03 32 58.68	−27 43 27.9	52 ± 8	6.26
13	BLAST J033215−275027 (500μm)	57	03 32 15.44	−27 50 30.6	49 ± 8	6.08
14	BLAST J033153−273921 (500μm)	34,35	03 31 52.05	−27 39 21.8	50 ± 8	6.08
17	BLAST J033128−273942 (500μm)	2,3,4,5	03 31 28.18	−27 39 42.3	53 ± 8	6.01
20	BLAST J033256−280102 (500μm)	94	03 32 56.40	−28 01 05.4	48 ± 8	5.84
21	BLAST J033217−275212 (500μm)	58,59	03 32 18.29	−27 52 12.7	47 ± 8	5.74
23	BLAST J033321−275510 (500μm)	124	03 33 22.24	−27 55 14.4	47 ± 8	5.70
24	BLAST J033318−274926 (500μm)	120,121,122	03 33 17.67	−27 49 26.6	46 ± 8	5.67
26		73,74	03 32 37.60	−27 35 31.5	46 ± 8	5.61
31	BLAST J033220−275631 (500μm)	60	03 32 20.86	−27 56 26.3	43 ± 8	5.27
33	BLAST J033212−275558 (500μm)	53	03 32 13.11	−27 56 03.4	43 ± 8	5.24
35	BLAST J033156−274511 (500μm)		03 31 58.33	−27 45 13.5	42 ± 8	5.20
37	BLAST J033249−274227 (500μm)	86,87,88	03 32 47.94	−27 42 25.3	43 ± 8	5.14
41	BLAST J033253−273759 (500μm)	93	03 32 52.93	−27 37 59.7	41 ± 8	5.05
43	BLAST J033301−275625 (500μm)	98	03 33 00.48	−27 56 08.5	41 ± 8	5.05
44	BLAST J033309−275125 (500μm)	109	03 33 09.35	−27 51 20.1	41 ± 8	5.05
48	BLAST J033135−275448 (500μm)	13,14,15,16	03 31 36.29	−27 54 42.9	41 ± 8	4.99
53	BLAST J033229−274426 (500μm)	64,65	03 32 29.05	−27 44 30.6	41 ± 8	4.96
56	BLAST J033235−275518 (500μm)	69	03 32 35.23	−27 55 14.6	41 ± 8	4.91
57	BLAST J033317−274558 (500μm)	114	03 33 14.92	−27 45 32.0	40 ± 8	4.90
58	BLAST J033210−273725 (500μm)	52	03 32 10.34	−27 37 20.0	40 ± 8	4.87
64	BLAST J033129−275918 (500μm)	9	03 31 29.49	−27 59 14.7	41 ± 8	4.77
68	BLAST J033211−275210 (500μm)	49	03 32 10.34	−27 51 54.0	39 ± 8	4.74
84	BLAST J033253−274459 (500μm)		03 32 54.41	−27 44 52.3	37 ± 8	4.58
88	BLAST J033153−274943 (500μm)	40	03 31 52.34	−27 49 27.5	38 ± 8	4.57
91	BLAST J033213−274302 (500μm)	50,51	03 32 13.32	−27 43 01.3	38 ± 8	4.55
103			03 32 34.40	−27 50 17.3	36 ± 8	4.43
104	BLAST J033229−274314 (500μm)	66	03 32 29.47	−27 43 08.2	36 ± 8	4.42
109	BLAST J033256−274539 (500μm)		03 32 56.26	−27 45 49.6	35 ± 8	4.37
128	BLAST J033318−274115 (500μm)	116	03 33 19.16	−27 41 15.3	35 ± 8	4.28
133	BLAST J033238−275638 (500μm)	75	03 32 38.87	−27 56 44.9	35 ± 8	4.26
137	BLAST J033323−274900 (500μm)		03 33 23.47	−27 48 53.7	35 ± 8	4.26
144		89	03 32 49.97	−27 58 33.2	35 ± 8	4.24
156	BLAST J033137−273743 (500μm)		03 31 37.89	−27 37 30.7	36 ± 8	4.16
157	BLAST J033157−275930 (500μm)	42	03 31 56.89	−27 59 26.3	34 ± 8	4.15
162	BLAST J033143−274817 (500μm)	21,22	03 31 43.92	−27 48 19.2	33 ± 8	4.14
176	BLAST J033300−274852 (500μm)	96	03 32 59.71	−27 48 53.8	32 ± 8	4.06

SID 500	Previously Published Name	Match ID	R.A. (h m s)	Dec. (° ′ ″)	Flux Density (mJy)	SNR
177		29	03 31 48.34	−28 02 03.3	34 ± 8	4.06
191	BLAST J033215−275901 (500μm)		03 32 13.32	−27 59 08.4	33 ± 8	4.03
199	BLAST J033247−275415 (500μm)	85	03 32 47.54	−27 54 14.0	33 ± 8	4.01
200		103	03 33 06.56	−28 00 46.8	33 ± 8	4.01
202	BLAST J033154−275343 (500μm)	36,37,38,39	03 31 54.94	−27 53 35.8	33 ± 8	4.00
203	BLAST J033215−275901 (500μm)	55,56	03 32 17.57	−27 58 46.5	33 ± 8	4.00
205	BLAST J033153−274943 (500μm)	40	03 31 54.51	−27 49 43.2	33 ± 8	3.99
210	BLAST J033208−280121 (500μm)	44	03 32 06.41	−28 01 07.1	32 ± 8	3.97
222	BLAST J033309−275347 (500μm)	102	03 33 09.20	−27 54 00.5	32 ± 8	3.94
223	BLAST J033222−274555 (500μm)		03 32 22.75	−27 45 52.9	31 ± 8	3.93
248	BLAST J033145−274148 (500μm)	25	03 31 46.11	−27 41 44.2	31 ± 8	3.87
250	BLAST J033235−274931 (500μm)	70	03 32 35.56	−27 49 04.7	32 ± 8	3.87
253	BLAST J033307−274001 (500μm)		03 33 07.81	−27 39 36.2	32 ± 8	3.86
261	BLAST J033148−280315 (500μm)		03 31 49.06	−28 03 13.2	31 ± 8	3.84
267	BLAST J033243−273914 (500μm)	81	03 32 43.67	−27 39 38.1	31 ± 8	3.83

Table C4. 870 μm sources from Weiss et al. (2009) that land within the coverage of the matching catalogue. The columns have the same meaning as in Table C1, although the SNR is measured with respect to the combined instrumental and confusion noise. In addition, the 33 sources marked with an asterisk in the 'Match ID' columm have no matches in any of the BLAST source catalogues (Tables C1-C3). These sources are used to measure priors, but are not otherwise analyzed in this paper.

SID 870	Previously Published Name	Match ID	R.A. (^{h} ^{m} ^{s})	Dec. ($^\circ$ $'$ $''$)	Flux Density (mJy)	SNR
1	LESS J033314.3−275611	113	03 33 14.26	−27 56 11.2	14.7 ± 1.2	12.48
2	LESS J033302.5−275643	98	03 33 02.50	−27 56 43.6	12.2 ± 1.2	10.31
3	LESS J033321.5−275520	124	03 33 21.51	−27 55 20.2	11.9 ± 1.2	10.12
4	LESS J033136.0−275439	13,14,15	03 31 36.01	−27 54 39.2	11.2 ± 1.1	9.72
5	LESS J033129.5−275907	9	03 31 29.46	−27 59 07.3	10.1 ± 1.2	8.45
6	LESS J033257.1−280102	94	03 32 57.14	−28 01 02.1	9.8 ± 1.2	8.16
7	LESS J033315.6−274523	114	03 33 15.55	−27 45 23.6	9.4 ± 1.2	7.89
9	LESS J033211.3−275210	49	03 32 11.29	−27 52 10.4	9.4 ± 1.2	7.71
10	LESS J033219.0−275219	59	03 32 19.02	−27 52 19.4	9.3 ± 1.2	7.60
11	LESS J033213.6−275602	53	03 32 13.58	−27 56 02.5	9.2 ± 1.2	7.58
12	LESS J033248.1−275414	85	03 32 48.12	−27 54 14.7	8.9 ± 1.2	7.24
13	LESS J033249.2−274246	87,88	03 32 49.23	−27 42 46.6	8.9 ± 1.2	7.21
14	LESS J033152.6−280320	33	03 31 52.64	−28 03 20.4	9.5 ± 1.3	7.19
16	LESS J033218.9−273738	*	03 32 18.89	−27 37 38.7	8.2 ± 1.2	6.87
17	LESS J033207.6−275123	46	03 32 07.59	−27 51 23.0	7.8 ± 1.2	6.36
18	LESS J033205.1−274652	45	03 32 05.12	−27 46 52.1	7.7 ± 1.2	6.30
19	LESS J033208.1−275818	47	03 32 08.10	−27 58 18.7	7.5 ± 1.2	6.19
20	LESS J033316.6−280018	*	03 33 16.56	−28 00 18.8	7.5 ± 1.2	6.15
25	LESS J033157.1−275940	42	03 31 57.05	−27 59 40.8	7.0 ± 1.2	5.83
26	LESS J033136.9−275456	14,15,16	03 31 36.90	−27 54 56.1	6.8 ± 1.2	5.80
28	LESS J033302.9−274432	*	03 33 02.92	−27 44 32.6	7.0 ± 1.2	5.62
31	LESS J033150.0−275743	*	03 31 49.96	−27 57 43.9	6.7 ± 1.2	5.51
32	LESS J033243.6−274644	*	03 32 43.57	−27 46 44.0	6.8 ± 1.2	5.46
33	LESS J033149.8−275332	*	03 31 49.78	−27 53 32.9	6.8 ± 1.2	5.46
34	LESS J033217.6−275230	58	03 32 17.64	−27 52 30.3	6.8 ± 1.2	5.40
36	LESS J033149.2−280208	29	03 31 49.15	−28 02 08.7	6.9 ± 1.3	5.36
38	LESS J033310.2−275641	110	03 33 10.20	−27 56 41.5	6.4 ± 1.2	5.22
40	LESS J033246.7−275120	*	03 32 46.74	−27 51 20.9	6.4 ± 1.2	5.18
42	LESS J033231.0−275858	67,68	03 32 31.02	−27 58 58.1	6.4 ± 1.2	5.13
43	LESS J033307.0−274801	104,105	03 33 07.00	−27 48 01.0	6.4 ± 1.3	5.12
45	LESS J033225.7−275228	*	03 32 25.71	−27 52 28.5	6.3 ± 1.2	5.10
49	LESS J033124.5−275040	*	03 31 24.45	−27 50 40.9	6.6 ± 1.3	5.05
50	LESS J033141.2−274441	19,20	03 31 41.15	−27 44 41.5	6.1 ± 1.2	5.02
51	LESS J033144.8−274425	*	03 31 44.81	−27 44 25.1	6.2 ± 1.2	5.01
52	LESS J033128.5−275601	6,7,8	03 31 28.51	−27 56 01.3	6.2 ± 1.2	4.94
53	LESS J033159.1−275435	*	03 31 59.12	−27 54 35.5	6.2 ± 1.2	4.93
55	LESS J033302.2−274033	*	03 33 02.20	−27 40 33.6	6.1 ± 1.2	4.90
56	LESS J033153.2−273936	34,35	03 31 53.17	−27 39 36.1	6.0 ± 1.2	4.89
57	LESS J033152.0−275329	36,37	03 31 51.97	−27 53 29.7	6.1 ± 1.3	4.87
59	LESS J033303.9−274412	99	03 33 03.87	−27 44 12.2	6.0 ± 1.2	4.77
60	LESS J033317.5−275121	117	03 33 17.47	−27 51 21.5	5.8 ± 1.2	4.75
61	LESS J033245.6−280025	*	03 32 45.63	−28 00 25.3	5.9 ± 1.2	4.73

SID 870	Previously Published Name	Match ID	R.A. (h m s)	Dec. (° ′ ″)	Flux Density (mJy)	SNR
63	LESS J033308.5−280044	103	03 33 08.46	−28 00 44.3	6.0 ± 1.3	4.71
64	LESS J033201.0−280025	*	03 32 01.00	−28 00 25.6	5.8 ± 1.2	4.70
65	LESS J033252.4−273527	*	03 32 52.40	−27 35 27.7	5.9 ± 1.3	4.67
67	LESS J033243.3−275517	79,80	03 32 43.28	−27 55 17.9	5.9 ± 1.3	4.67
68	LESS J033233.4−273918	*	03 32 33.44	−27 39 18.5	5.8 ± 1.2	4.65
69	LESS J033134.3−275934	*	03 31 34.26	−27 59 34.3	5.7 ± 1.2	4.65
70	LESS J033144.0−273832	*	03 31 43.97	−27 38 32.5	5.7 ± 1.2	4.64
72	LESS J033240.4−273802	76	03 32 40.40	−27 38 02.5	5.7 ± 1.2	4.63
73	LESS J033229.3−275619	*	03 32 29.33	−27 56 19.3	5.8 ± 1.2	4.63
74	LESS J033309.3−274809	106,107,108	03 33 09.34	−27 48 09.9	5.8 ± 1.3	4.62
75	LESS J033126.8−275554	6	03 31 26.83	−27 55 54.6	5.8 ± 1.3	4.61
77	LESS J033157.2−275633	*	03 31 57.23	−27 56 33.2	5.5 ± 1.2	4.42
79	LESS J033221.3−275623	60	03 32 21.25	−27 56 23.5	5.5 ± 1.2	4.40
80	LESS J033142.2−274834	21,22	03 31 42.23	−27 48 34.4	5.4 ± 1.2	4.38
81	LESS J033127.5−274440	1	03 31 27.45	−27 44 40.4	5.7 ± 1.3	4.38
82	LESS J033253.8−273810	93	03 32 53.77	−27 38 10.9	5.3 ± 1.2	4.35
84	LESS J033154.2−275109	*	03 31 54.22	−27 51 09.8	5.5 ± 1.3	4.33
88	LESS J033155.2−275345	38,39	03 31 55.19	−27 53 45.3	5.4 ± 1.3	4.28
89	LESS J033248.4−280023	*	03 32 48.44	−28 00 23.8	5.3 ± 1.2	4.25
90	LESS J033243.7−273554	*	03 32 43.65	−27 35 54.1	5.4 ± 1.3	4.23
91	LESS J033135.3−274033	*	03 31 35.25	−27 40 33.7	5.3 ± 1.3	4.22
92	LESS J033138.4−274336	*	03 31 38.36	−27 43 36.0	5.2 ± 1.2	4.22
94	LESS J033307.3−275805	101	03 33 07.27	−27 58 05.0	5.3 ± 1.2	4.20
95	LESS J033241.7−275846	*	03 32 41.74	−27 58 46.1	5.2 ± 1.2	4.18
96	LESS J033313.0−275556	112,113	03 33 13.03	−27 55 56.8	5.2 ± 1.2	4.18
97	LESS J033313.7−273803	*	03 33 13.65	−27 38 03.4	5.1 ± 1.2	4.16
98	LESS J033130.2−275726	10,11	03 31 30.22	−27 57 26.0	5.1 ± 1.2	4.11
99	LESS J033251.5−275536	*	03 32 51.45	−27 55 36.0	5.3 ± 1.3	4.11
101	LESS J033151.5−274552	*	03 31 51.47	−27 45 52.1	5.1 ± 1.3	4.08
104	LESS J033258.5−273803	*	03 32 58.46	−27 38 03.0	4.9 ± 1.2	4.05
106	LESS J033140.1−275631	18	03 31 40.09	−27 56 31.4	4.9 ± 1.2	4.03
107	LESS J033130.9−275150	*	03 31 30.85	−27 51 50.9	5.0 ± 1.2	4.02
108	LESS J033316.4−275033	115	03 33 16.42	−27 50 33.1	5.0 ± 1.2	4.02
113	LESS J033236.4−275845	*	03 32 36.42	−27 58 45.9	5.0 ± 1.3	3.94
114	LESS J033150.8−274438	31,32	03 31 50.81	−27 44 38.5	4.9 ± 1.3	3.90
116	LESS J033154.4−274525	*	03 31 54.42	−27 45 25.5	4.9 ± 1.3	3.84
117	LESS J033128.0−273925	2,3,4	03 31 28.02	−27 39 25.2	5.0 ± 1.3	3.83
120	LESS J033328.5−275655	125	03 33 28.45	−27 56 55.9	4.9 ± 1.3	3.79
122	LESS J033139.6−274120	17	03 31 39.62	−27 41 20.4	4.7 ± 1.2	3.77

Table C5. Matches between external catalogue with each of the 4 submm source lists. The first column gives a unique short ID that is used throughout this paper. Since all radio sources and the FIDEL catalogue use the SIMPLE survey (*Spitzer* IRAC/MUSYC Public Legacy in ECDF-S; Gawiser et al. 2006) as a positional prior, the SIMPLE IDs for each source are given in column two. The only exceptions are 870 µm sources with no identification in the matching catalogue; these sources have simply been added to the catalogue with the SIMPLE ID replaced by the 870 µm SID referring to Table C4 (in boldface brackets). The third and fourth columns give the IRAC J2000 coordinates of each source (or the 870 µm position when unavailable). There are then 4 blocks of 5 columns for each submm band giving: the submm SID for each respective submm source list to which the source was matched (Tables C1-C4); the radial separation in arcsec; the likelihood ratio; and finally the 24 µm and 1.4 GHz P values when available.

ID	SIMPLE	R.A.	Dec.	250 µm					350 µm					500 µm					870 µm				
		(h m s)	(° ′ ″)	SID 250	Δr (″)	LR	P_{24}	$P_{\rm r}$	SID 350	Δr (″)	LR	P_{24}	$P_{\rm r}$	SID 500	Δr (″)	LR	P_{24}	$P_{\rm r}$	SID 870	Δr (″)	LR	P_{24}	$P_{\rm r}$
1	37075	03 31 27.53	−27 44 39.5	78	11.2	14.4	0.098	0.058	235	8.2	11.2	0.061	0.035	...	...	...	...	...	81	1.5	43.1	0.003	0.002
2	45028	03 31 27.58	−27 39 27.7	...	...	...	...	...	22	7.4	1.7	0.215	0.066	...	...	...	...	...	117	6.3	2.2	0.168	0.048
3	45037	03 31 27.94	−27 39 36.4	...	...	...	...	...	22	4.4	3.7	0.076	0.038	17	6.6	1.6	0.141	0.075	117	11.3	1.2	...	...
4	45195	03 31 28.80	−27 39 16.9	...	...	...	...	...	...	...	...	...	...	...	...	...	...	...	117	13.3	1.0	...	...
5	45836	03 31 28.87	−27 39 04.0	80	2.9	1.3	0.013	0.051	...	...	...	...	...	...	...	...	...	...	...	...	...	...	...
6	18957	03 31 27.19	−27 55 50.9	...	...	...	...	...	...	...	...	...	...	9	27.4	2.5	...	...	...	...	...	...	...
7	18523	03 31 28.87	−27 56 07.8	...	...	...	...	...	...	...	...	...	...	...	...	...	...	...	52	8.1	1.7	0.206	0.492
8	17966	03 31 30.05	−27 56 02.4	111	0.8	16.9	0.001	0.001	...	...	...	...	...	...	...	...	...	...	...	...	...	...	...
9	**(5)**	03 31 29.46	−27 59 07.3	99	5.2	...	...	...	177	2.8	...	...	...	64	7.4	...	...	...	...	...	...	...	...
10	16359	03 31 29.90	−27 57 22.3	16	1.8	8.0	0.014	0.003	16	3.8	13.7	0.052	0.012	11	5.1	9.9	0.082	0.020	98	5.6	16.9	0.092	0.022
11	15753	03 31 30.74	−27 57 33.8	16	14.4	1.2	0.615	0.056	...	...	...	...	...	...	...	...	...	...	...	...	...	...	...
12	44643	03 31 36.10	−27 39 40.7	70	5.8	3.0	0.031	0.029	...	...	...	...	...	...	...	...	...	...	...	...	...	...	...
13	21125	03 31 35.50	−27 54 35.3	...	...	...	...	...	49	12.1	5.0	0.336	0.146	48	12.9	3.3	0.359	0.163	4	7.8	10.2	0.198	0.073
14	20735	03 31 35.90	−27 54 43.2	...	...	...	...	...	49	7.5	1.1	0.201	0.549	...	...	...	...	...	4	4.3	4.6	0.090	0.355
15	20560	03 31 36.14	−27 54 49.7	...	...	...	...	...	49	9.7	2.3	0.197	0.162	48	7.0	4.2	0.128	0.105	26	11.8	2.7	...	...
16	19870	03 31 36.94	−27 55 10.6	...	...	...	...	...	...	...	...	...	...	...	...	...	...	...	26	14.5	1.3	...	...
17	42263	03 31 39.53	−27 41 19.3	244	10.1	41.3	0.023	0.050	42	7.1	70.1	0.013	0.028	...	...	...	...	...	122	1.5	79.8	0.001	0.002
18	18083	03 31 40.18	−27 56 22.6	92	14.1	1.7	0.221	0.198	...	...	...	...	...	...	...	...	...	...	106	9.1	8.1	0.120	0.102
19	37304	03 31 40.97	−27 44 34.8	85	3.9	5.2	0.038	0.031	37	4.0	9.7	0.040	0.033	...	...	...	...	...	50	7.0	15.2	0.094	0.076
20	36814	03 31 41.38	−27 44 46.7	...	...	...	...	...	...	...	...	...	...	...	...	...	...	...	50	6.0	1.6	0.129	0.078
21	31008	03 31 41.64	−27 48 30.2	...	...	...	...	...	...	...	...	...	...	...	...	...	...	...	80	9.0	1.1	0.235	0.501
22	30829	03 31 42.79	−27 48 36.7	...	...	...	...	...	...	...	...	...	...	...	...	...	...	...	80	7.9	1.1	0.399	0.165
23	19031	03 31 41.76	−27 55 37.9	...	...	...	...	...	187	9.3	1.4	0.280	0.105	...	...	...	...	...	...	...	...	...	...
24	18659	03 31 43.58	−27 55 28.2	255	17.9	1.1	...	...	...	...	...	...	...	...	...	...	...	...	...	...	...	...	...
25	40970	03 31 44.45	−27 42 11.9	57	9.0	1.7	0.098	0.061	...	...	...	...	...	...	...	...	...	...	...	...	...	...	...
26	**(125)**	03 31 46.02	−27 46 21.2	32	17.6	...	...	...	...	...	...	...	...	...	...	...	...	...	125	0.0	...	...	...
27	16076	03 31 46.56	−27 57 34.9	36	10.9	21.2	0.033	0.035	...	...	...	...	...	...	...	...	...	...	...	...	...	...	...
28	31651	03 31 48.02	−27 48 01.8	...	...	...	...	...	188	10.5	6.2	0.113	0.117	...	...	...	...	...	...	...	...	...	...
29	10254	03 31 48.94	−28 02 13.6	...	...	...	...	...	322	10.2	2.7	0.211	0.183	177	13.0	3.7	0.283	0.252	36	5.6	11.1	0.090	0.074
30	38757	03 31 49.73	−27 43 26.0	59	8.6	10.5	0.030	0.042	35	2.2	4.4	0.003	0.004	...	...	...	...	...	...	...	...	...	...
31	37046	03 31 50.30	−27 44 46.7	...	...	...	...	...	...	...	...	...	...	...	...	...	...	...	114	10.7	1.5	...	...
32	36827	03 31 51.10	−27 44 37.0	146	1.3	8.1	0.003	0.003	47	4.0	9.7	0.019	0.023	...	...	...	...	...	114	3.9	30.6	0.019	0.021
33	8829	03 31 52.46	−28 03 18.7	...	...	...	...	...	95	19.2	1.0	...	...	...	...	...	...	...	14	2.8	17.4	0.112	0.012
34	45260	03 31 52.08	−27 39 26.6	51	9.3	5.9	0.109	0.013	124	8.1	16.4	0.087	0.010	14	4.8	14.1	0.038	0.004	...	...	...	...	...
35	45144	03 31 53.11	−27 39 37.4	51	8.3	1.1	0.166	0.169	124	9.8	2.3	0.208	0.211	14	21.0	1.9	0.451	0.458	56	1.4	11.5	0.010	0.010
36	22926	03 31 51.94	−27 53 26.9	...	...	...	...	...	...	...	...	...	...	...	...	...	...	...	57	2.9	10.8	0.027	0.032
37	22719	03 31 52.56	−27 53 33.0	...	...	...	...	...	...	...	...	...	...	...	...	...	...	...	57	8.4	4.3	0.372	0.165
38	22221	03 31 54.82	−27 53 40.9	...	...	...	...	...	...	...	...	...	...	...	...	...	...	...	88	6.6	5.7	0.109	0.042
39	22204	03 31 55.75	−27 53 47.4	...	...	...	...	...	...	...	...	...	...	...	...	...	...	...	88	7.9	2.5	0.207	0.224
40	28865	03 31 54.67	−27 49 44.4	...	...	...	...	...	93	7.0	1.5	0.193	0.144	205	2.5	1.9	0.040	0.029	...	...	...	...	...
41	37463	03 31 54.98	−27 44 10.3	188	11.2	1.2	0.431	0.052	...	...	...	...	...	...	...	...	...	...	...	...	...	...	...
42	13515	03 31 56.86	−27 59 39.1	...	...	...	...	...	...	...	...	...	...	157	12.7	3.4	0.317	0.196	25	3.1	17.3	0.044	0.022
43	41664	03 32 02.14	−27 41 28.7	...	...	...	...	...	170	9.6	2.6	0.220	0.132	...	...	...	...	...	...	...	...	...	...
44	11649	03 32 04.66	−28 00 57.6	328	12.1	2.0	0.375	0.071	...	...	...	...	...	...	...	...	...	...	...	...	...	...	...
45	33160	03 32 04.87	−27 46 47.3	75	3.9	4.7	0.016	0.015	19	5.8	3.2	0.032	0.028	...	...	...	...	...	18	5.8	11.8	0.032	0.028

ID	SIMPLE	R.A.	Dec.	250 μm					350 μm					500 μm					870 μm				
		(h m s)	(° ′ ″)	SID	Δr (″)	LR	P_{24}	$P_{\rm r}$	SID	Δr (″)	LR	P_{24}	$P_{\rm r}$	SID	Δr (″)	LR	P_{24}	$P_{\rm r}$	SID	Δr (″)	LR	P_{24}	$P_{\rm r}$
46	26136	03 32 07.27	−27 51 20.2	...	...	...	...	...	...	...	...	...	...	...	...	...	...	...	17	5.0	1.6	0.096	0.024
47	15657	03 32 08.23	−27 58 13.8	...	...	...	...	...	...	...	...	...	...	8	9.0	1.2	0.447	0.181	19	5.1	3.9	0.251	0.075
48	9589	03 32 10.99	−28 02 35.9	246	6.8	1.2	0.162	0.134	...	...	...	...	...	...	...	...	...	...	...	...	...	...	...
49	24758	03 32 11.35	−27 52 13.1	...	...	...	...	...	...	...	...	...	...	...	...	...	...	...	9	2.7	3.5	0.091	0.041
50	40039	03 32 10.49	−27 43 08.8	358	13.5	2.0	0.146	0.313	...	...	...	...	...	...	...	...	...	...	...	...	...	...	...
51	39690	03 32 12.55	−27 43 05.9	...	...	...	...	...	...	...	...	...	...	91	11.4	3.6	0.280	0.248	...	...	...	...	...
52	47577	03 32 11.64	−27 37 26.0	...	...	...	...	...	88	4.3	64.1	0.005	0.001	58	18.2	20.1	0.055	0.012	...	...	...	...	...
53	18807	03 32 13.85	−27 55 59.9	...	...	...	...	...	...	...	...	...	...	33	10.4	1.8	0.455	0.183	11	4.4	7.4	0.181	0.048
54	44585	03 32 16.20	−27 39 30.2	...	...	...	...	...	108	12.6	35.7	0.032	0.190	...	...	...	...	...	...	...	...	...	...
55	14672	03 32 17.04	−27 58 46.6	...	...	...	...	...	...	...	...	...	...	203	7.0	1.8	0.398	0.004	...	...	...	...	...
56	13333	03 32 17.06	−27 59 16.4	38	9.7	30.3	0.019	0.054	80	10.2	24.3	0.021	0.059	...	...	...	...	...	...	...	...	...	...
57	25701	03 32 17.86	−27 50 58.9	289	6.7	5.1	0.017	0.060	...	...	...	...	...	...	...	...	...	...	...	...	...	...	...
58	24159	03 32 17.18	−27 52 20.6	58	11.2	1.3	0.259	0.113	65	14.8	1.5	0.351	0.168	...	...	...	...	...	...	...	...	...	...
59	24739	03 32 19.06	−27 52 14.5	...	...	...	...	...	65	12.6	2.6	0.450	0.139	21	10.3	1.6	0.384	0.106	10	5.0	10.9	0.162	0.032
60	17994	03 32 21.60	−27 56 23.3	45	3.5	2.9	0.014	0.048	...	...	...	...	...	31	10.2	1.0	0.085	0.232	79	4.7	4.1	0.023	0.072
61	11555	03 32 22.58	−28 00 23.4	97	6.3	8.4	0.006	0.011	...	...	...	...	...	...	...	...	...	...	...	...	...	...	...
62	48158	03 32 23.66	−27 36 48.2	91	12.4	64.5	0.006	0.056	...	...	...	...	...	...	...	...	...	...	...	...	...	...	...
63	46695	03 32 25.03	−27 38 22.6	325	1.0	1.6	0.003	0.001	169	5.3	1.1	0.044	0.024	...	...	...	...	...	...	...	...	...	...
64	35317	03 32 29.86	−27 44 24.4	5	8.4	87.8	0.002	0.010	8	10.1	4.2	0.003	0.014	53	12.6	1.3	0.005	0.021	...	...	...	...	...
65	37400	03 32 29.98	−27 44 04.9	5	12.2	60.8	0.010	0.038	8	14.2	19.9	0.013	0.048	...	...	...	...	...	...	...	...	...	...
66	39003	03 32 29.93	−27 43 00.8	...	...	...	...	...	12	6.4	1.2	0.142	0.091	104	9.5	1.4	0.240	0.164	...	...	...	...	...
67	13126	03 32 30.55	−27 59 11.4	121	7.5	124.9	0.004	0.017	85	11.5	69.4	0.008	0.036	...	...	...	...	...	...	...	...	...	...
68	14440	03 32 31.46	−27 58 51.6	...	...	...	...	...	85	22.1	1.0	...	...	...	...	...	...	...	42	8.7	8.6	0.176	0.103
69	17925	03 32 35.06	−27 55 32.5	3	1.9	28.1	0.000	0.001	3	2.9	17.8	0.001	0.002	...	...	...	...	...	...	...	...	...	...
70	29372	03 32 35.71	−27 49 16.0	113	13.8	3.4	0.131	0.186	...	...	...	...	...	250	11.5	2.7	0.100	0.147	...	...	...	...	...
71	10608	03 32 36.05	−28 01 37.9	...	...	...	...	...	259	10.9	1.4	0.320	0.132	...	...	...	...	...	...	...	...	...	...
72	10758	03 32 36.43	−28 01 50.9	...	...	...	...	...	259	7.4	2.0	0.294	0.092	...	...	...	...	...	...	...	...	...	...
73	50164	03 32 37.46	−27 35 47.8	69	5.9	4.3	0.038	0.067	69	5.7	3.6	0.036	0.064	...	...	...	...	...	...	...	...	...	...
74	50104	03 32 37.90	−27 35 49.9	69	6.5	4.7	0.046	0.050	69	8.2	3.4	0.068	0.074	...	...	...	...	...	...	...	...	...	...
75	16640	03 32 38.90	−27 57 00.4	316	12.5	27.7	0.016	0.082	...	...	...	...	...	133	15.5	6.9	0.023	0.114	...	...	...	...	...
76	46989	03 32 40.06	−27 38 08.5	...	...	...	...	...	...	...	...	...	...	...	...	...	...	...	72	7.6	1.2	0.057	0.200
77	46485	03 32 42.58	−27 38 25.8	60	12.3	20.6	0.030	0.072	...	...	...	...	...	...	...	...	...	...	...	...	...	...	...
78	46947	03 32 42.86	−27 38 17.2	60	13.2	1.1	0.516	0.021	...	...	...	...	...	...	...	...	...	...	...	...	...	...	...
79	19784	03 32 43.20	−27 55 14.5	...	...	...	...	...	128	4.5	9.5	0.024	0.030	...	...	...	...	...	67	3.7	31.1	0.017	0.022
80	19900	03 32 43.75	−27 55 16.3	...	...	...	...	...	...	...	...	...	...	...	...	...	...	...	67	6.4	2.5	0.277	0.154
81	44806	03 32 43.49	−27 39 29.2	82	8.7	1.9	0.087	0.190	...	...	...	...	...	...	...	...	...	...	...	...	...	...	...
82	25546	03 32 44.04	−27 51 43.2	298	7.6	21.0	0.048	0.025	...	...	...	...	...	...	...	...	...	...	...	...	...	...	...
83	25673	03 32 44.26	−27 51 41.0	298	10.9	67.1	0.003	0.040	...	...	...	...	...	...	...	...	...	...	...	...	...	...	...
84	15411	03 32 45.96	−27 57 45.4	24	1.3	30.2	0.000	0.001	116	10.1	3.7	0.017	0.050	...	...	...	...	...	...	...	...	...	...
85	21056	03 32 47.95	−27 54 16.2	...	...	...	...	...	...	...	...	...	...	...	...	...	...	...	12	2.6	1.9	0.137	0.035
86	40193	03 32 47.88	−27 42 32.8	...	...	...	...	...	...	...	...	...	...	37	7.6	1.7	0.023	0.028	...	...	...	...	...
87	40147	03 32 48.94	−27 42 51.1	...	...	...	...	...	...	...	...	...	...	...	...	...	...	...	13	6.1	3.9	0.478	0.210
88	40166	03 32 49.42	−27 42 35.3	...	...	...	...	...	...	...	...	...	...	...	...	...	...	...	13	11.6	1.7	...	...
89	14647	03 32 49.32	−27 58 45.1	17	3.5	12.8	0.033	0.008	7	11.4	6.8	0.195	0.055	144	14.6	7.6	0.263	0.082	...	...	...	...	...
90	48957	03 32 49.42	−27 36 36.0	369	17.0	1.1	...	...	...	...	...	...	...	...	...	...	...	...	...	...	...	...	...

ID	SIMPLE	R.A.	Dec.	250 μm					350 μm					500 μm					870 μm				
		(h m s)	(° ′ ″)	SID	Δr (″)	LR	P_{24}	$P_{\rm r}$	SID	Δr (″)	LR	P_{24}	$P_{\rm r}$	SID	Δr (″)	LR	P_{24}	$P_{\rm r}$	SID	Δr (″)	LR	P_{24}	$P_{\rm r}$
91	12980	03 32 51.79	−27 59 56.0	389	15.2	1.2	0.145	0.165	...	...	...	...	...	...	...	...	...	...	...	...	...	...	...
92	11316	03 32 53.06	−28 01 17.8	...	...	...	...	...	90	6.5	2.9	0.102	0.106	...	...	...	...	...	...	...	...	...	...
93	**(82)**	03 32 53.77	−27 38 10.9	...	...	...	...	...	52	31.8	...	...	...	41	15.8	...	...	...	...	...	...	...	...
94	**(6)**	03 32 57.14	−28 01 02.1	...	...	...	...	...	...	...	...	...	...	20	10.3	...	...	...	...	...	...	...	...
95	38977	03 32 57.62	−27 43 18.1	27	11.4	2.4	0.100	0.136	...	...	...	...	...	...	...	...	...	...	...	...	...	...	...
96	29432	03 32 59.33	−27 48 58.7	...	...	...	...	...	...	...	...	...	...	176	7.0	10.2	0.029	0.094	...	...	...	...	...
97	50259	03 32 59.33	−27 35 34.1	130	5.3	21.0	0.030	0.019	...	...	...	...	...	...	...	...	...	...	...	...	...	...	...
98	17004	03 33 01.58	−27 56 49.6	...	...	...	...	...	64	9.9	2.5	0.240	0.142	...	...	...	...	...	...	...	...	...	...
99	**(59)**	03 33 03.87	−27 44 12.2	...	...	...	...	...	115	31.7	...	...	...	...	...	...	...	...	5	0.0	...	...	...
100	37597	03 33 06.14	−27 44 15.4	...	...	...	...	...	115	1.8	1.3	0.011	0.016	...	...	...	...	...	...	...	...	...	...
101	15661	03 33 07.58	−27 58 05.9	...	...	...	...	...	...	...	...	...	...	...	...	...	...	...	94	4.4	1.2	0.177	0.362
102	21942	03 33 07.78	−27 53 51.4	...	...	...	...	...	...	...	...	...	...	222	20.9	1.4	0.226	0.335	...	...	...	...	...
103	**(63)**	03 33 08.46	−28 00 44.3	...	...	...	...	...	...	...	...	...	...	200	25.2	...	...	...	6	0.0	...	...	...
104	31482	03 33 06.62	−27 48 02.2	...	...	...	...	...	...	...	...	...	...	...	...	...	...	...	43	5.0	2.6	0.099	0.396
105	30926	03 33 07.25	−27 48 08.3	...	...	...	...	...	...	...	...	...	...	...	...	...	...	...	43	8.1	1.1	0.074	0.189
106	31537	03 33 09.14	−27 48 16.9	...	...	...	...	...	145	8.7	1.4	0.278	0.169	...	...	...	...	...	74	7.4	4.9	0.222	0.126
107	30714	03 33 09.72	−27 48 01.4	52	14.7	27.5	0.031	0.052	145	22.0	2.6	...	...	...	...	...	...	...	74	9.7	11.3	0.015	0.025
108	30905	03 33 09.77	−27 48 20.9	...	...	...	...	...	...	...	...	...	...	...	...	...	...	...	74	12.5	2.2	...	...
109	26260	03 33 10.13	−27 51 24.8	...	...	...	...	...	...	...	...	...	...	44	11.3	1.3	0.263	0.237	...	...	...	...	...
110	**(38)**	03 33 10.20	−27 56 41.5	...	...	...	...	...	...	...	...	...	...	7	36.8	...	...	...	...	...	...	...	...
111	41860	03 33 11.78	−27 41 38.4	...	...	...	...	...	31	10.2	6.5	0.256	0.035	...	...	...	...	...	...	...	...	...	...
112	18562	03 33 12.62	−27 55 51.6	...	...	...	...	...	298	15.9	2.1	...	...	...	...	...	...	...	96	7.5	1.2	0.024	0.073
113	**(1)**	03 33 14.26	−27 56 11.2	...	...	...	...	...	298	13.8	...	...	...	7	32.9	...	...	...	1	0.0	...	...	...
114	35704	03 33 15.41	−27 45 24.1	...	...	...	...	...	98	8.8	2.4	0.113	0.113	57	10.3	1.6	0.142	0.144	7	1.8	4.4	0.009	0.009
115	26283	03 33 16.51	−27 50 39.5	72	4.2	39.5	0.002	0.007	...	...	...	...	...	...	...	...	...	...	108	6.4	4.2	0.004	0.015
116	41704	03 33 16.94	−27 41 21.5	185	10.7	27.3	0.017	0.039	...	...	...	...	...	...	...	...	...	...	...	...	...	...	...
117	25765	03 33 17.52	−27 51 27.7	...	...	...	...	...	...	...	...	...	...	...	...	...	...	...	60	6.3	3.0	0.090	0.069
118	34104	03 33 17.78	−27 46 23.5	...	...	...	...	...	43	12.9	1.8	0.294	0.150	...	...	...	...	...	...	...	...	...	...
119	34567	03 33 17.78	−27 46 05.9	54	2.6	7.9	0.012	0.011	43	11.1	5.9	0.122	0.115	...	...	...	...	...	...	...	...	...	...
120	28590	03 33 17.42	−27 49 48.7	...	...	...	...	...	...	...	...	...	...	24	22.3	2.7	0.300	0.177	...	...	...	...	...
121	29761	03 33 17.81	−27 49 10.6	...	...	...	...	...	...	...	...	...	...	24	16.3	1.1	0.538	0.375	...	...	...	...	...
122	28465	03 33 18.70	−27 49 40.1	...	...	...	...	...	...	...	...	...	...	24	19.2	2.0	0.549	0.128	...	...	...	...	...
123	20681	03 33 18.91	−27 54 33.5	67	9.9	1.9	0.129	0.141	...	...	...	...	...	...	...	...	...	...	...	...	...	...	...
124	19773	03 33 21.48	−27 55 20.3	...	...	...	...	...	...	...	...	...	...	...	...	...	...	...	3	0.4	2.4	0.010	0.015
125	17028	03 33 28.56	−27 56 54.2	...	...	...	...	...	14	15.2	1.0	0.273	0.313	5	5.9	5.0	0.075	0.093	120	2.3	11.2	0.015	0.019

Table C6. Matches between external catalogue with each of the Maximum-likelihood submm photometry, SED model fits and redshifts. Uncertainties in flux densities have the estimated confusion noise (Tables 1) added in quadrature to the instrumental noise. The temperatures, $T_{\rm obs}$ and 10-1000 μm total infrared (TIR) fluxes, $S_{\rm TIR}$ are for *observed-frame* modified blackbody fits of the form $S_\nu \propto \nu^{2.0} B_\nu(T_{\rm obs})$ (rest-frame values shown in Fig. E1). The fractional uncertainties in the TIR fluxes, $\Delta S_{\rm TIR}/S_{\rm TIR}$, are produced from the same Monte Carlo simulation used to measure uncertainties in the temperatures. SED fits are not provided for confused sources (see SEDs with 'C' indicated in Fig. E1). When redshifts are available, the TIR luminosity, $L_{\rm TIR}$, is also calculated, but integrating in the *rest-frame*, and using a more realistic SED fit from the library of Dale et al. (2001) in order to estimate emission in the mid/far-IR (fits shown in Fig. E1). Redshifts in boldface are optical spectroscopic measurements, redshifts in regular face are optical photometric estimates, and redshifts in brackets are IRAC-based photometric estimates. The superscripts indicate where the redshifts were found: 'P' from the composite catalogue of Pascale et al. (2009); 'I' from Ivison et al. (2009); 'D' from Dunlop et al. (2009); and 'C' from Casey et al. (in prep).

ID	S_{250} (mJy)	S_{350} (mJy)	S_{500} (mJy)	S_{870} (mJy)	$T_{\rm obs}$ (K)	$S_{\rm TIR}$ ($\log_{10}$ W m^{-2})	$\Delta S_{\rm TIR}/S_{\rm TIR}$	$L_{\rm TIR}$ ($\log_{10}$ L$_\odot$)	Redshift (z)
1	38±18	41±15	9±13	5.1±1.2	10.5±1.7	-15.3	0.50	12.4	(1.9)$^{\rm P}$
2	17±33	-41±30	-92±31	1.2±2.2	...	...	...	...	1.1$^{\rm P}$
3	39±31	96±29	131±30	2.3±2.1	...	...	...	...	0.8$^{\rm P}$
4	26±32	-2±30	0±31	2.1±1.5	...	...	...	...	1.7$^{\rm P}$
5	62±30	56±29	29±30	2.2±1.4	...	...	...	...	2.6$^{\rm P}$
6	14±21	29±19	42±18	3.6±1.2	9.7±1.9	-15.5	0.62	12.6	2.7$^{\rm P}$
7	-20±34	-7±33	-28±39	4.1±1.3	...	...	...	...	(1.9)$^{\rm P}$
8	93±30	29±29	49±31	-0.2±1.3	...	...	...	...	**0.677**$^{\rm I}$
9	69±18	47±15	51±13	9.6±1.2	9.9±1.0	-15.1	0.35	...	...
10	109±24	85±20	60±18	3.3±1.2	...	...	...	...	**1.482**$^{\rm C}$
11	-14±24	-25±20	-13±18	2.8±1.2	...	...	...	...	0.4$^{\rm P}$
12	68±18	40±15	22±13	-0.4±1.2	17.7±1.6	-14.8	0.33	12.4	1.2$^{\rm P}$
13	-38±47	-19±52	28±50	4.1±1.8	...	...	...	...	...
14	30±85	57±101	-4±101	2.9±2.5	...	...	...	...	(1.2)$^{\rm P}$
15	16±58	19±68	17±67	6.3±1.8	...	...	...	...	0.1$^{\rm P}$
16	24±22	-8±20	14±19	4.4±1.2	6.2±3.0	-16.2	0.90	11.6	2.1$^{\rm P}$
17	27±18	40±15	25±13	4.2±1.2	10.4±1.9	-15.3	0.47	12.4	**2.024**$^{\rm P}$
18	55±18	20±15	14±13	3.6±1.2	13.0±3.9	-15.1	0.90	13.1	3.0$^{\rm P}$
19	31±29	51±26	50±23	2.5±1.3	...	...	...	...	(0.6)$^{\rm P}$
20	28±29	-2±26	-23±23	3.9±1.3	...	...	...	...	0.4$^{\rm P}$
21	21±27	13±23	24±22	2.9±1.3	...	...	...	...	1.2$^{\rm P}$
22	-9±27	3±23	3±22	3.2±1.3	...	...	...	...	(2.2)$^{\rm P}$
23	21±19	37±16	27±15	2.5±1.2	11.4±2.3	-15.4	0.80	12.1	(1.5)$^{\rm P}$
24	29±19	26±16	0±15	1.7±1.2	21.5±3.2	-14.7	0.23	9.9	**0.095**$^{\rm P}$
25	65±18	33±15	30±13	1.4±1.2	15.7±1.1	-14.9	0.25	12.2	1.1$^{\rm I}$
26	77±18	22±15	22±13	3.9±1.2	14.4±5.8	-14.9	0.90	...	...
27	78±18	45±15	22±13	0.4±1.2	23.2±0.8	-14.3	0.09	11.6	**0.364**$^{\rm P}$
28	40±18	37±15	12±13	3.1±1.2	12.5±3.5	-15.2	0.90	11.3	0.6$^{\rm P}$
29	35±18	39±15	30±13	6.5±1.2	9.6±2.5	-15.3	0.58	12.5	(2.1)$^{\rm P}$
30	84±18	53±15	33±13	3.2±1.2	18.2±0.4	-14.5	0.10	12.0	**0.620**$^{\rm P}$
31	18±22	-10±20	25±19	1.7±1.2	9.2±4.0	-16.0	0.90	12.2	(3.0)$^{\rm P}$
32	57±23	79±20	15±19	3.4±1.2	13.5±2.1	-14.9	0.43	12.6	**1.605**$^{\rm C}$

ID	S_{250} (mJy)	S_{350} (mJy)	S_{500} (mJy)	S_{870} (mJy)	$T_{\rm obs}$ (K)	$S_{\rm TIR}$ ($\log_{10}$ W m^{-2})	$\Delta S_{\rm TIR}/S_{\rm TIR}$	$L_{\rm TIR}$ ($\log_{10}$ L$_\odot$)	Redshift (z)
33	29±18	33±15	22±13	8.1±1.3	8.4±1.3	-15.4	0.49	11.7	(1.2)$^{\rm P}$
34	41±19	29±17	26±15	1.1±1.2	14.5±1.8	-15.1	0.40	12.8	**2.342**$^{\rm C}$
35	73±20	50±17	38±15	5.2±1.2	12.3±1.4	-14.9	0.35	13.2	2.9$^{\rm P}$
36	1±25	7±22	24±24	4.0±1.6	...	...	...	...	**2.940**$^{\rm P}$
37	21±27	17±25	-19±32	2.2±1.6	...	...	...	...	(1.4)$^{\rm P}$
38	10±31	7±31	50±42	2.0±1.3	...	...	...	...	...
39	28±29	27±28	-13±34	3.6±1.3	...	...	...	...	1.8$^{\rm P}$
40	60±18	60±15	48±13	3.2±1.2	13.0±2.5	-15.0	0.72	12.8	(2.1)$^{\rm P}$
41	54±18	43±15	24±13	2.6±1.2	16.5±0.5	-14.8	0.14	11.6	0.6$^{\rm P}$
42	11±18	31±15	26±13	6.1±1.2	8.3±2.0	-15.6	0.46	11.9	(1.6)$^{\rm P}$
43	16±18	31±15	-1±13	1.3±1.2	18.5±1.3	-15.0	0.26	9.9	0.1$^{\rm P}$
44	30±18	12±15	11±13	2.0±1.2	12.8±5.3	-15.4	0.90	10.1	0.2$^{\rm P}$
45	68±18	58±15	20±13	6.3±1.2	11.7±1.6	-15.0	0.37	12.9	**2.252**$^{\rm C}$
46	14±18	28±15	19±13	7.4±1.2	7.8±1.1	-15.6	0.43	11.0	0.7$^{\rm P}$
47	55±18	60±15	65±13	6.0±1.2	10.7±1.2	-15.1	0.32	9.7	(0.1)$^{\rm P}$
48	37±18	5±15	5±13	-0.1±1.2	32.6±10.3	-14.1	0.69	12.5	0.7$^{\rm P}$
49	22±18	56±15	43±13	8.6±1.2	8.8±0.6	-15.3	0.26	12.2	(1.6)$^{\rm P}$
50	42±18	-15±16	-10±14	1.7±1.2	17.5±1.0	-15.2	0.24	11.2	0.6$^{\rm P}$
51	15±18	38±16	43±14	2.0±1.2	11.1±2.9	-15.4	0.88	12.1	1.7$^{\rm D}$
52	30±18	52±15	32±13	2.1±1.2	12.5±1.6	-15.2	0.38	12.3	**1.565**$^{\rm P}$
53	16±18	10±15	35±13	8.1±1.2	7.1±0.8	-15.7	0.38	10.7	(0.6)$^{\rm P}$
54	47±18	43±15	10±13	-0.6±1.2	17.1±0.9	-14.9	0.28	12.4	**1.324**$^{\rm P}$
55	33±19	33±16	21±14	0.2±1.2	18.1±6.4	-14.9	0.90	11.6	0.6$^{\rm P}$
56	74±19	50±16	17±14	2.1±1.2	21.0±0.7	-14.4	0.12	10.5	0.1$^{\rm P}$
57	56±18	28±15	19±13	1.5±1.2	20.4±0.9	-14.6	0.15	10.3	**0.124**$^{\rm D}$
58	47±19	25±16	31±14	3.0±1.2	12.6±1.8	-15.2	0.43	12.0	**1.097**$^{\rm D}$
59	36±19	50±17	26±15	8.2±1.2	9.2±1.0	-15.3	0.37	12.6	2.3$^{\rm D}$
60	69±18	32±15	37±13	4.4±1.2	12.6±3.0	-15.0	0.90	12.9	**2.277**$^{\rm C}$
61	51±18	18±15	-5±13	-0.3±1.2	25.2±2.2	-14.4	0.15	10.1	0.1$^{\rm P}$
62	48±18	26±15	19±13	1.0±1.2	24.4±2.0	-14.4	0.16	10.3	0.1$^{\rm P}$
63	68±18	41±15	34±13	1.8±1.2	15.8±1.6	-14.8	0.32	12.3	1.1$^{\rm P}$
64	97±20	42±18	33±16	1.9±1.2	24.8±1.2	-14.1	0.11	10.4	**0.077**$^{\rm I}$

ID	S_{250} (mJy)	S_{350} (mJy)	S_{500} (mJy)	S_{870} (mJy)	$T_{\rm obs}$ (K)	$S_{\rm TIR}$ ($\log_{10}$ W m^{-2})	$\Delta S_{\rm TIR}/S_{\rm TIR}$	$L_{\rm TIR}$ ($\log_{10}$ L$_\odot$)	Redshift (z)
65	66±21	36±18	1±16	0.1±1.2	24.8±1.8	-14.3	0.14	10.1	**0.076**$^{\rm P}$
66	64±18	73±15	43±13	4.0±1.2	12.7±1.3	-14.9	0.27	12.4	1.4$^{\rm P}$
67	51±19	26±16	6±14	2.5±1.2	...	...	...	...	**0.125**$^{\rm P}$
68	27±18	4±16	-10±14	4.2±1.2	...	...	...	...	(2.3)$^{\rm P}$
69	185±18	78±15	33±13	0.1±1.2	22.1±0.3	-14.1	0.05	9.7	**0.038**$^{\rm D}$
70	54±18	35±15	40±13	2.7±1.2	13.2±1.4	-15.1	0.32	13.1	2.8$^{\rm P}$
71	19±20	27±18	13±16	-1.3±1.2	...	...	...	...	0.6$^{\rm P}$
72	26±20	10±18	-3±16	1.6±1.2	...	...	...	...	(2.2)$^{\rm P}$
73	102±29	67±26	95±23	-1.4±1.8	...	...	...	...	(1.8)$^{\rm P}$
74	-31±29	-11±26	-53±23	2.7±1.8	...	...	...	...	0.2$^{\rm P}$
75	48±18	29±15	30±13	-1.6±1.2	22.3±0.9	-14.6	0.13	11.1	**0.297**$^{\rm P}$
76	30±18	35±15	21±13	4.4±1.2	10.3±1.2	-15.3	0.55	11.4	**0.830**$^{\rm P}$
77	13±29	64±26	59±24	3.1±1.8	...	...	...	...	**0.250**$^{\rm P}$
78	39±29	-47±26	-50±24	-1.1±1.8	...	...	...	...	0.1$^{\rm P}$
79	78±27	41±24	23±22	1.8±1.5	...	...	...	...	**2.123**$^{\rm C}$
80	-24±27	12±24	1±22	3.8±1.5	...	...	...	...	2.8$^{\rm P}$
81	56±18	32±15	21±13	1.3±1.2	17.9±5.4	-14.7	0.90	11.9	**0.733**$^{\rm P}$
82	55±27	33±23	9±22	0.4±1.9	...	...	...	...	**0.279**$^{\rm P}$
83	-10±27	0±23	-2±22	0.4±1.9	...	...	...	...	**0.279**$^{\rm P}$
84	95±18	52±15	23±13	2.3±1.2	21.1±0.5	-14.3	0.10	10.4	**0.104**$^{\rm P}$
85	45±18	23±15	27±13	7.7±1.2	9.0±1.1	-15.4	0.40	12.7	2.8$^{\rm D\dagger}$
86	67±21	69±18	31±16	2.4±1.2	...	...	...	...	**0.981**$^{\rm P}$
87	-27±21	-37±18	-22±16	7.3±1.2	...	...	...	...	(1.9)$^{\rm P}$
88	11±20	7±18	34±16	2.8±1.2	...	...	...	...	**0.981**$^{\rm P}$
89	99±18	68±15	22±13	2.3±1.2	16.4±0.5	-14.6	0.13	13.3	**2.326**$^{\rm C}$
90	9±18	-23±15	3±13	0.7±1.2	30.3±10.2	-15.6	0.38	10.3	0.4$^{\rm P}$
91	34±18	16±15	16±13	1.6±1.2	18.6±1.0	-14.9	0.21	11.6	**0.620**$^{\rm P}$
92	-6±18	42±15	8±13	1.8±1.2	9.9±1.1	-15.7	0.42	11.8	(1.6)$^{\rm P}$
93	52±18	51±15	42±13	4.6±1.2	11.6±1.0	-15.1	0.30	...	...
94	18±18	40±15	39±13	8.9±1.2	8.2±0.6	-15.4	0.27	...	...
95	90±18	55±15	38±13	2.8±1.2	15.7±1.2	-14.7	0.22	13.0	1.9$^{\rm P}$
96	44±18	13±15	29±13	1.3±1.2	16.0±5.9	-15.0	0.90	11.2	0.5$^{\rm P}$

†Source 85 has an optical photometric redshift limit $z > 2.8$ from Dunlop et al. (2009). Since this limit is significantly larger than its IRAC-based photometric redshift $z_{\rm i} = 1.6$ we use the limit as the best estimate for this source.

ID	S_{250} (mJy)	S_{350} (mJy)	S_{500} (mJy)	S_{870} (mJy)	$T_{\rm obs}$ (K)	$S_{\rm TIR}$ ($\log_{10}$ W m^{-2})	$\Delta S_{\rm TIR}/S_{\rm TIR}$	$L_{\rm TIR}$ ($\log_{10}$ L$_\odot$)	Redshift (z)
97	58±18	25±15	7±13	0.9±1.2	18.4±0.6	-14.8	0.17	10.6	$0.2^{\rm P}$
98	27±18	44±15	39±13	4.7±1.2	10.1±0.8	-15.3	0.33	11.9	$1.3^{\rm P}$
99	20±18	27±16	16±13	4.8±1.2	9.1±1.4	-15.5	0.55	...	...
100	43±18	41±16	5±13	0.4±1.2	20.6±6.4	-14.7	0.90	11.4	$0.4^{\rm P}$
101	17±18	33±15	23±13	4.7±1.2	9.3±1.2	-15.5	0.50	12.3	$(2.0)^{\rm P}$
102	37±18	10±15	29±13	1.9±1.2	13.1±3.2	-15.3	0.53	12.2	$1.5^{\rm P}$
103	-34±18	-6±15	13±13	5.2±1.2	4.4±1.5	-16.5	0.76	...	...
104	-34±29	51±28	7±34	3.0±1.3	...	...	...	...	$(3.0)^{\rm P}$
105	76±31	-30±32	31±43	3.0±1.3	...	...	...	...	$\mathbf{0.531}^{\rm P}$
106	49±30	87±31	-24±41	3.6±1.9	...	...	...	...	$(2.2)^{\rm P}$
107	24±23	-5±21	-4±20	2.0±1.2	...	...	...	...	$\mathbf{0.180}^{\rm I}$
108	-12±25	-46±22	49±25	-0.5±2.0	...	...	...	...	$(1.4)^{\rm P}$
109	54±18	36±15	35±13	0.9±1.2	16.9±4.0	-14.8	0.90	12.7	$(1.6)^{\rm P}$
110	40±18	33±15	33±13	6.1±1.2	9.9±1.2	-15.3	0.37	...	...
111	21±18	45±15	9±13	0.9±1.2	18.3±1.6	-14.9	0.33	10.8	$0.3^{\rm P}$
112	32±19	27±16	34±14	4.0±1.2	16.4±0.9	-14.8	0.27	10.9	$0.3^{\rm P}$
113	25±19	37±16	10±14	14.2±1.2	6.5±1.2	-15.6	0.57	...	...
114	19±18	46±15	32±13	8.8±1.2	8.4±0.9	-15.4	0.43	11.5	$0.9^{\rm P}$
115	70±18	23±15	-2±13	4.2±1.2	23.0±0.9	-14.3	0.11	10.3	$\mathbf{0.087}^{\rm P}$
116	48±18	49±15	23±13	1.9±1.2	22.5±1.1	-14.4	0.15	10.6	$\mathbf{0.148}^{\rm P}$
117	26±18	10±15	6±13	4.8±1.2	8.2±2.5	-15.7	0.90	11.6	$1.3^{\rm P}$
118	26±21	29±18	31±16	-0.1±1.2	18.2±3.3	-15.0	0.62	12.4	$1.4^{\rm P}$
119	63±21	44±18	13±16	3.9±1.2	13.3±2.2	-15.0	0.45	12.8	$2.1^{\rm C}$
120	-5±23	19±20	-4±20	3.3±1.2	...	...	...	...	$(1.9)^{\rm P}$
121	26±19	9±16	20±14	-0.7±1.2	...	...	...	...	$(2.0)^{\rm P}$
122	23±24	-8±21	20±21	1.8±1.2	...	...	...	...	$0.9^{\rm P}$
123	81±18	26±15	11±13	0.6±1.2	16.3±0.6	-14.8	0.24	11.4	$0.5^{\rm I}$
124	49±18	49±15	34±13	11.4±1.2	8.8±1.0	-15.2	0.37	12.2	$(1.5)^{\rm P}$
125	55±18	74±15	56±13	4.4±1.2	11.8±1.6	-15.0	0.45	...	...

APPENDIX D: POSTAGE STAMPS

This Appendix contains submm, IRAC and radio postage stamps for all 125 proposed identifications to the submm sources (Fig. D1).

APPENDIX E: SPECTRAL ENERGY DISTRIBUTIONS

This Appendix contains observed-frame radio–submm–(mid/near)-IR SEDs for all 125 proposed identifications to the submm sources (Fig. E1).

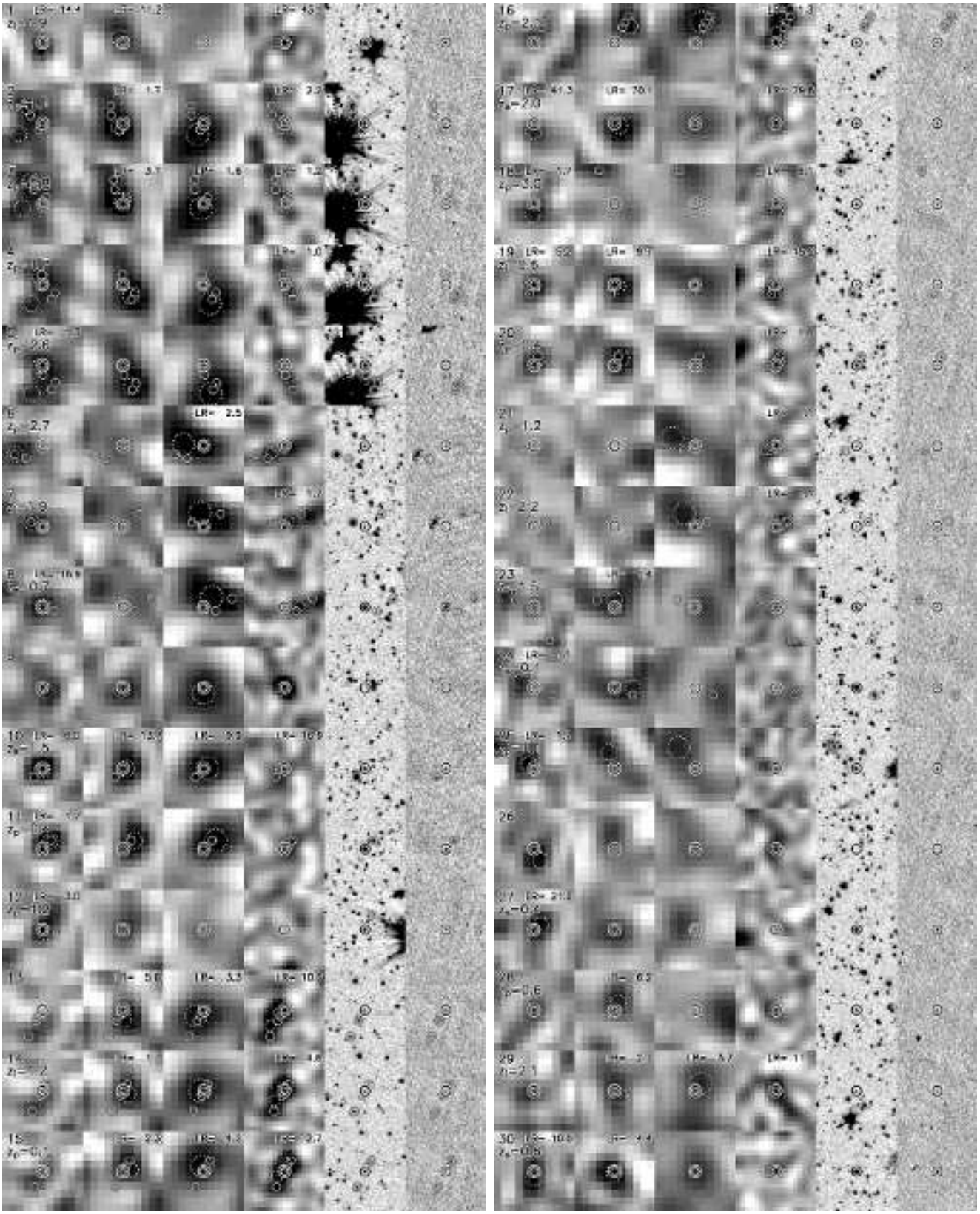

Figure D1. $1.8' \times 1.8'$ Postage stamps for each of the fitted sources. Columns from left to right: 250 μm, 350 μm, 500 μm, 870 μm(SNR maps, scaled between -3σ (white) and +5σ (black), 3.6 μm, and 1.4 GHz (-2 μJy (white), +5 μJy (black)). Small heavy circles indicate the source under consideration. Light smaller circles indicate other nearby sources that have been simultaneously fit in the submm bands. Large dashed circles on the submm images indicate input positions obtained from local maxima in the match-filtered images. Sources were matched to the external catalogue, and the reported redshifts are those that were used in Pascale et al. (2009) when available (subscript 's' indicates spectroscopic redshifts, 'p' optical photometric redshifts, and 'i' IRAC-based photometric redshifts). The likelihood ratios (LR) of the matches to each submm band are indicated in the top-right corners when available.

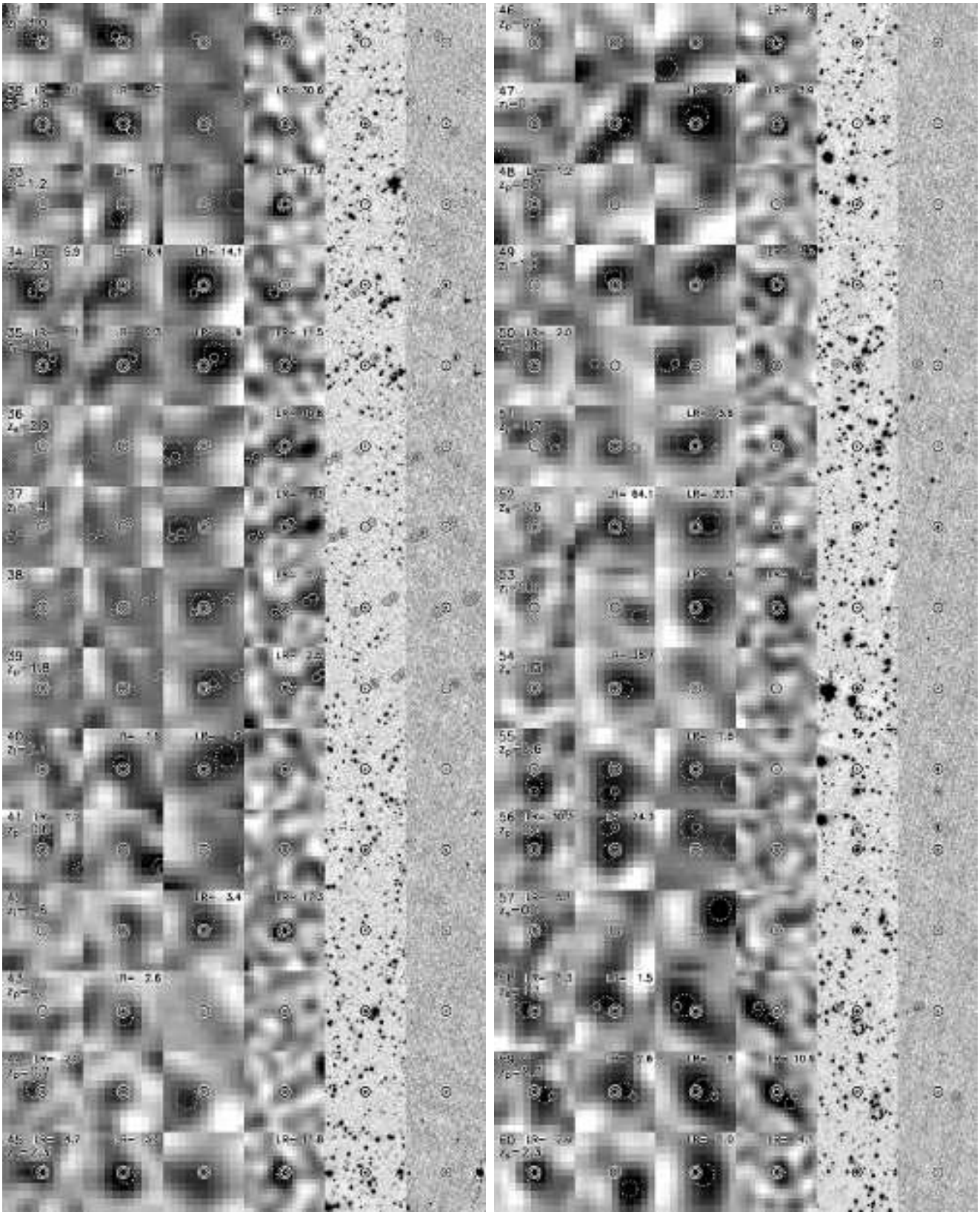

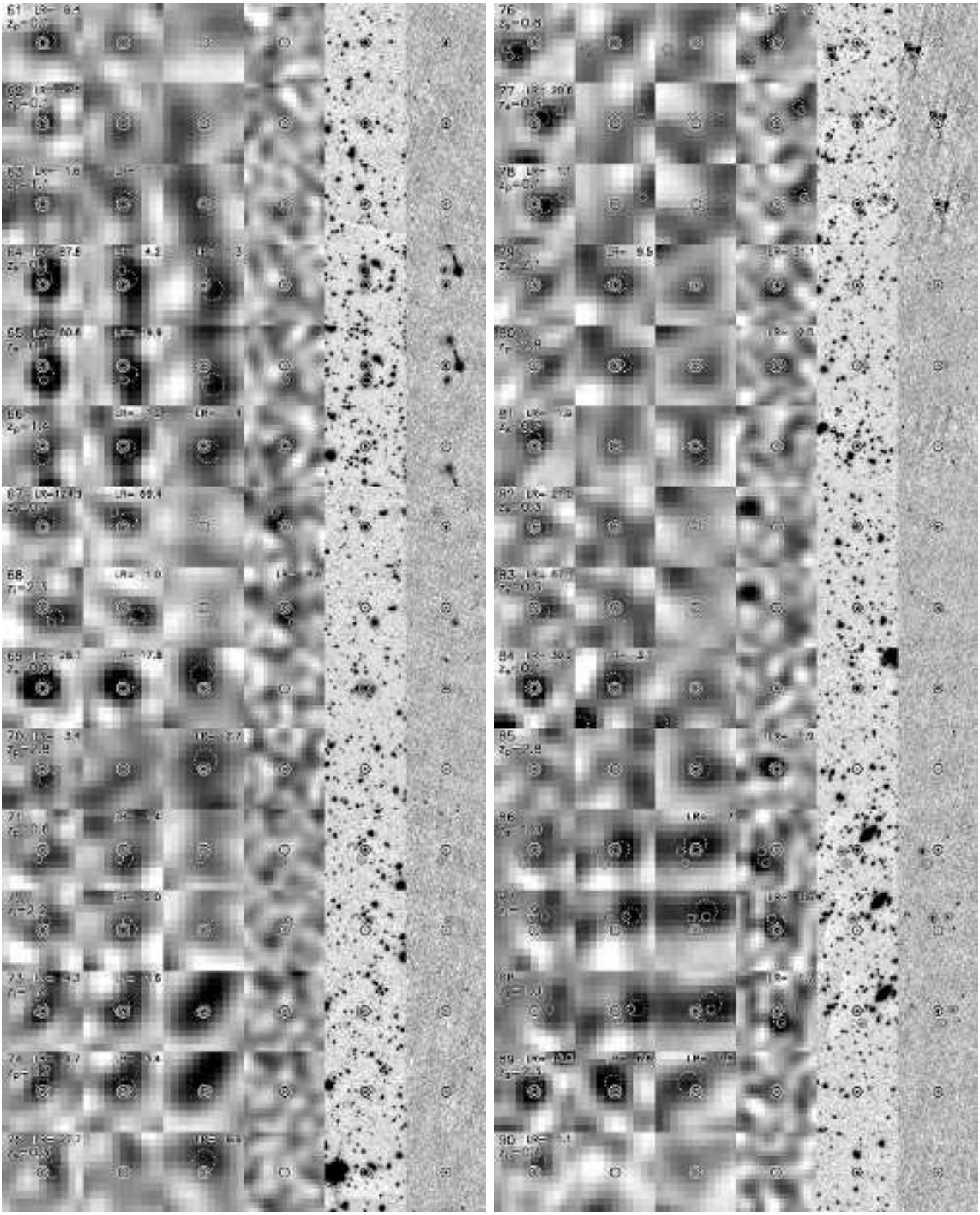

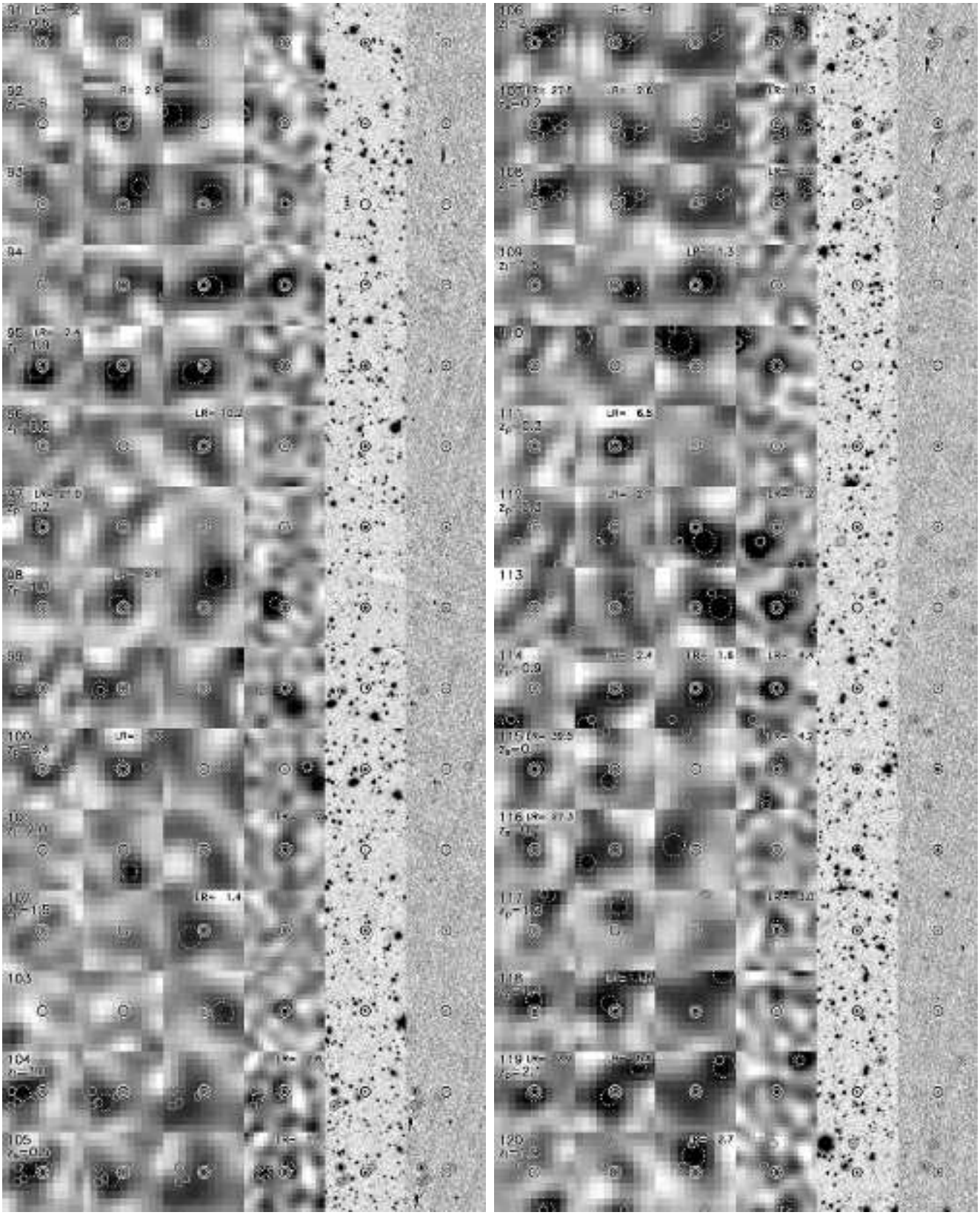

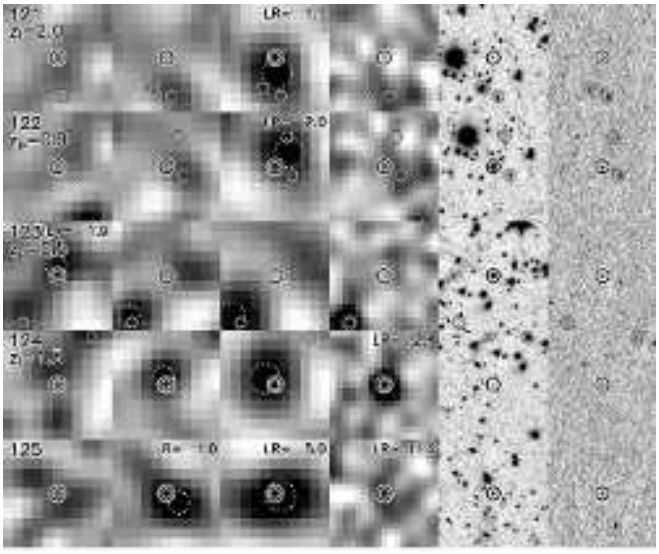

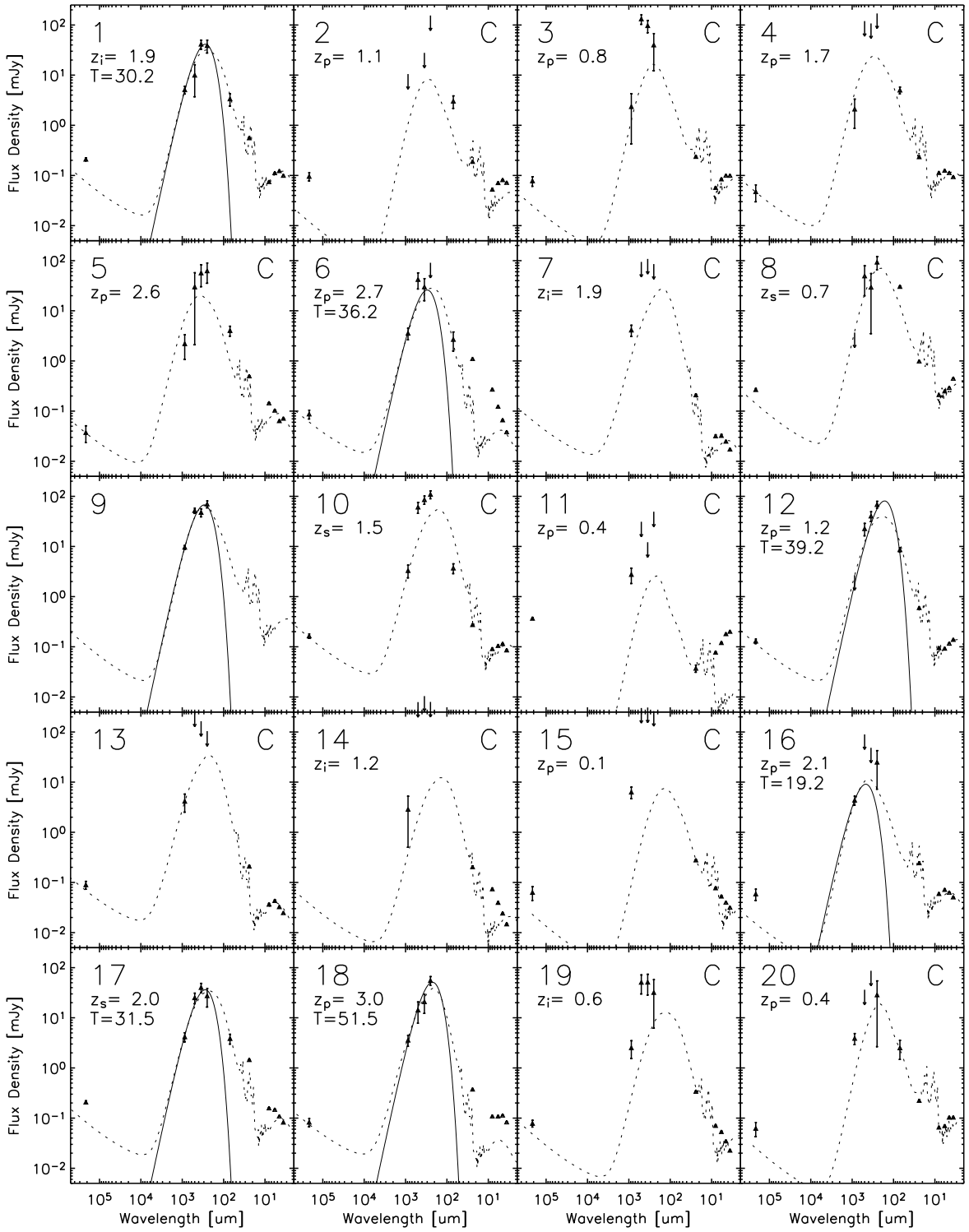

Figure E1. Observed-frame spectral energy distributions. The flux densities at all 125 positions are fit simultaneously in each submm map. In this way flux densities in blends are divided up. All matched sources have IRAC photometry from SIMPLE, and most sources also have 24 μm (and occasional 70 μm) flux densities from FIDEL. Most sources also have 1.4 GHz radio measurements. The only exceptions are sources for which the BLAST data have only been matched to an 870 μm source from LESS, whose position has been used to re-measure flux densities in the BLAST bands (no SED information given). Redshift labels have the same meaning as in Fig. E1. Dotted lines are SED fits to the submm and FIR photometry using the library of Dale et al. (2001). The 'C' indicates 42 sources that are confused to the point that the submm photometry is unusable, and only the Dale et al. (2001) SEDs are fit (to the radio and mid/near-IR photometry). For the remaining 83 sources a modified blackbody with emissivity $\beta = 2.0$ has been fit, with the maximum-likelihood *rest-frame* temperatures indicated for the 73 sources with redshifts.

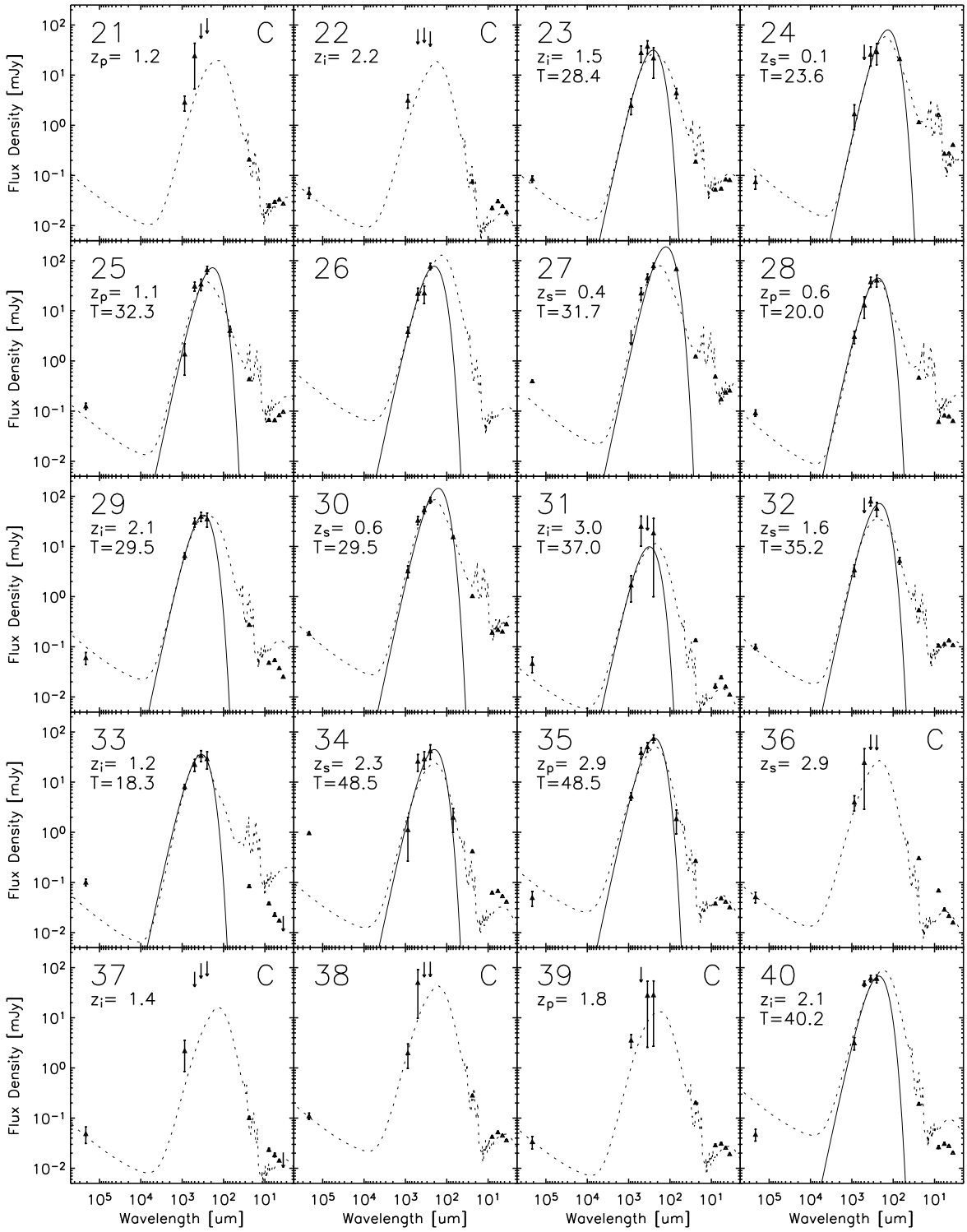
21
z_p= 1.2
C
22
z_i= 2.2
C
23
z_i= 1.5
T=28.4
24
z_s= 0.1
T=23.6
25
z_p= 1.1
T=32.3
26
27
z_s= 0.4
T=31.7
28
z_p= 0.6
T=20.0
29
z_i= 2.1
T=29.5
30
z_s= 0.6
T=29.5
31
z_i= 3.0
T=37.0
32
z_s= 1.6
T=35.2
33
z_i= 1.2
T=18.3
34
z_s= 2.3
T=48.5
35
z_p= 2.9
T=48.5
36
z_s= 2.9
C
37
z_i= 1.4
C
38
C
39
z_p= 1.8
C
40
z_i= 2.1
T=40.2
Flux Density [mJy]
Wavelength [um]

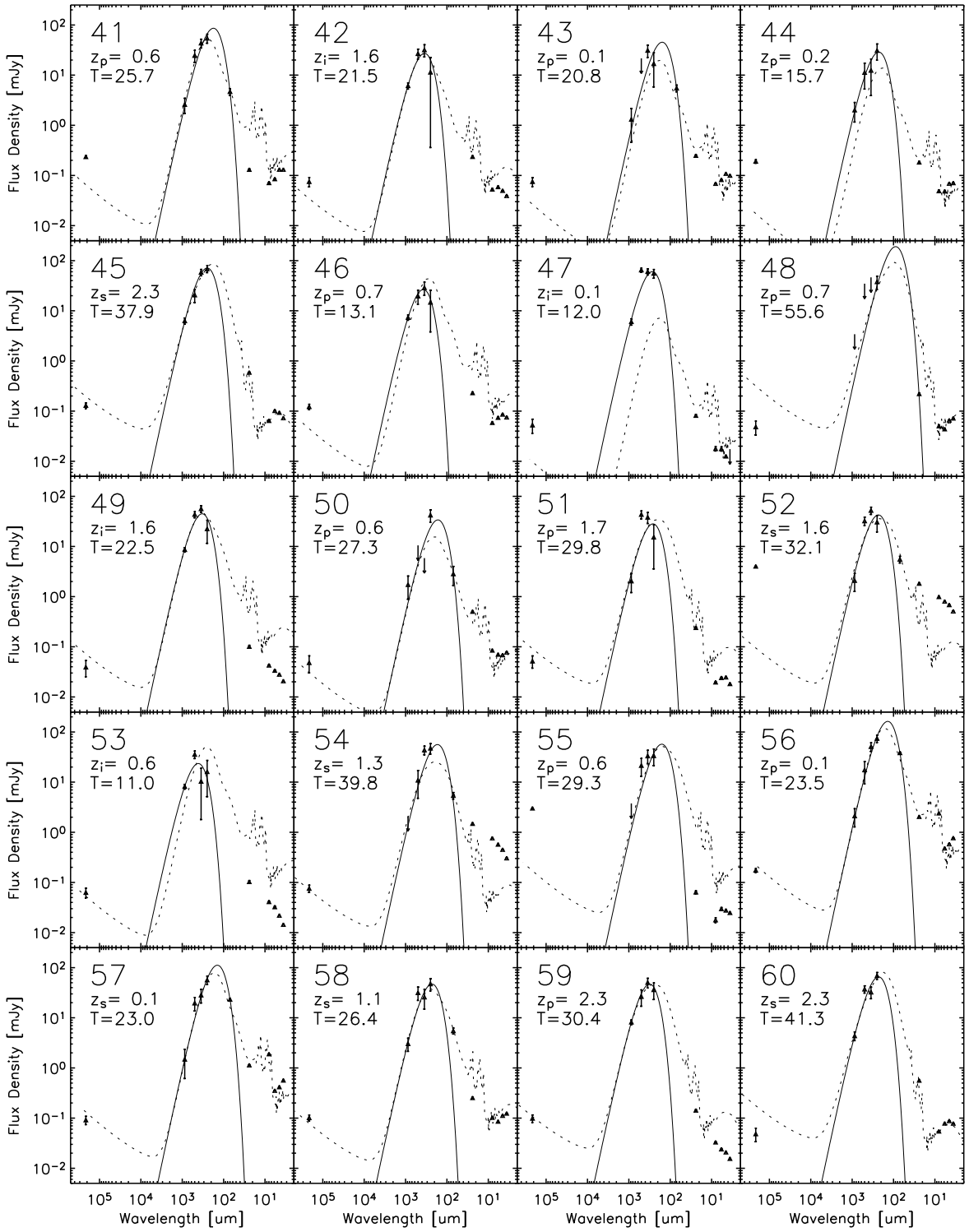
41
z_p= 0.6
T=25.7
42
z_i= 1.6
T=21.5
43
z_p= 0.1
T=20.8
44
z_p= 0.2
T=15.7
45
z_s= 2.3
T=37.9
46
z_p= 0.7
T=13.1
47
z_i= 0.1
T=12.0
48
z_p= 0.7
T=55.6
49
z_i= 1.6
T=22.5
50
z_p= 0.6
T=27.3
51
z_p= 1.7
T=29.8
52
z_s= 1.6
T=32.1
53
z_i= 0.6
T=11.0
54
z_s= 1.3
T=39.8
55
z_p= 0.6
T=29.3
56
z_p= 0.1
T=23.5
57
z_s= 0.1
T=23.0
58
z_s= 1.1
T=26.4
59
z_p= 2.3
T=30.4
60
z_s= 2.3
T=41.3
Flux Density [mJy]
Wavelength [um]

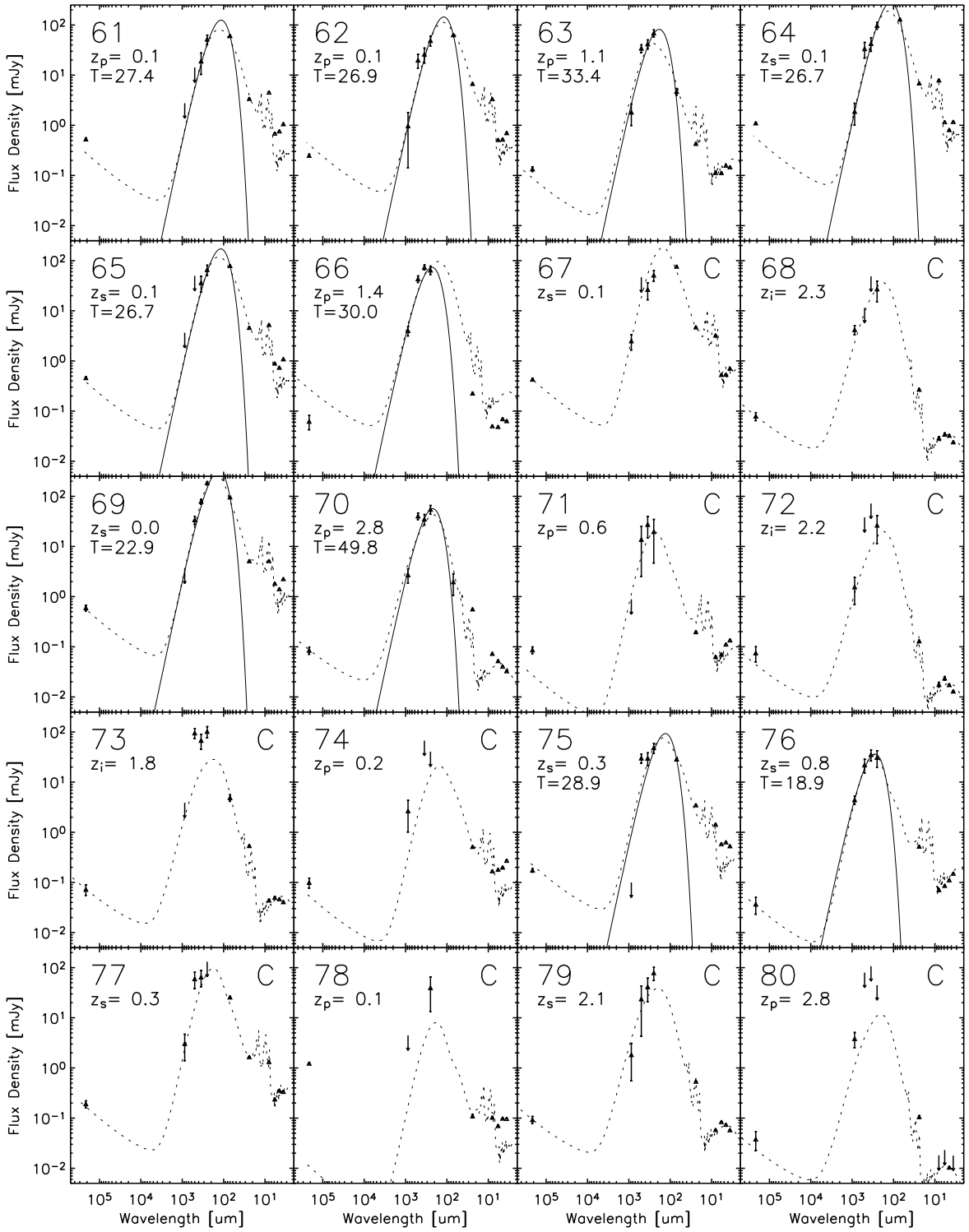
61
z_p= 0.1
T=27.4
62
z_p= 0.1
T=26.9
63
z_p= 1.1
T=33.4
64
z_s= 0.1
T=26.7
65
z_s= 0.1
T=26.7
66
z_p= 1.4
T=30.0
67 C
z_s= 0.1
68 C
z_i= 2.3
69
z_s= 0.0
T=22.9
70
z_p= 2.8
T=49.8
71 C
z_p= 0.6
72 C
z_i= 2.2
73 C
z_i= 1.8
74 C
z_p= 0.2
75
z_s= 0.3
T=28.9
76
z_s= 0.8
T=18.9
77 C
z_s= 0.3
78 C
z_p= 0.1
79 C
z_s= 2.1
80 C
z_p= 2.8
Flux Density [mJy]
Wavelength [um]

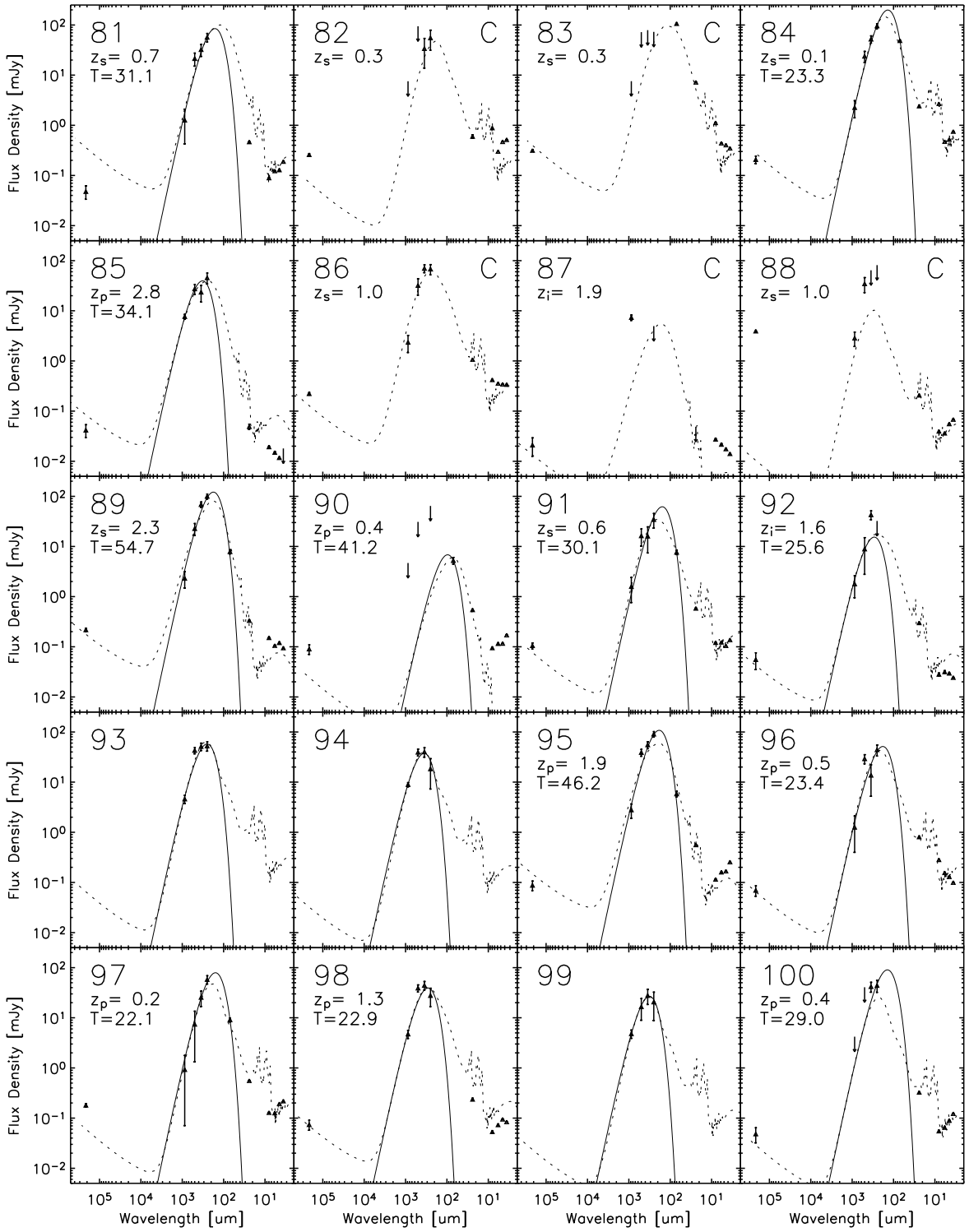
81
z_s= 0.7
T=31.1
82
z_s= 0.3
C
83
z_s= 0.3
C
84
z_s= 0.1
T=23.3
85
z_p= 2.8
T=34.1
86
z_s= 1.0
C
87
z_i= 1.9
C
88
z_s= 1.0
C
89
z_s= 2.3
T=54.7
90
z_p= 0.4
T=41.2
91
z_s= 0.6
T=30.1
92
z_i= 1.6
T=25.6
93
94
95
z_p= 1.9
T=46.2
96
z_p= 0.5
T=23.4
97
z_p= 0.2
T=22.1
98
z_p= 1.3
T=22.9
99
100
z_p= 0.4
T=29.0
Flux Density [mJy]
Wavelength [um]

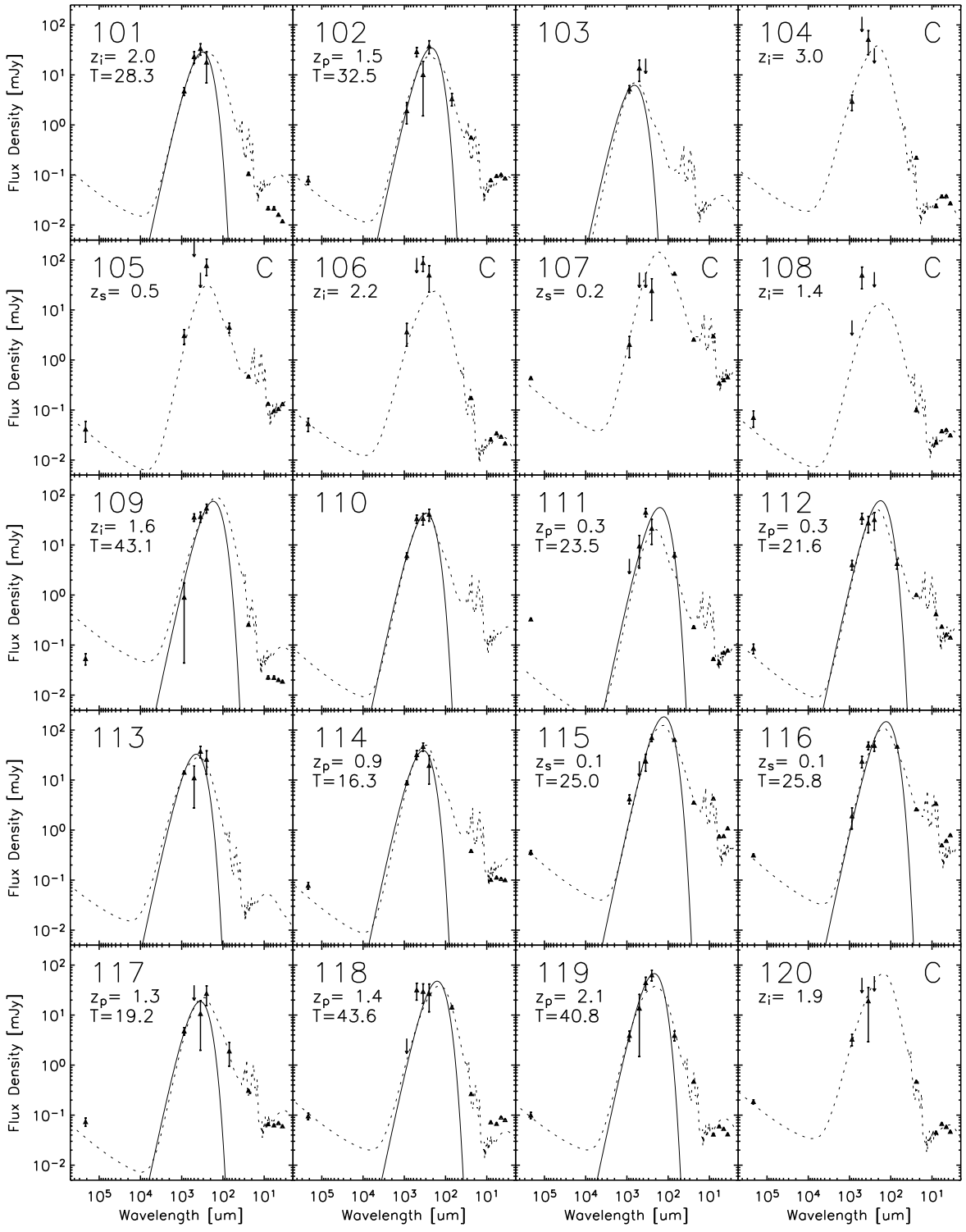
101
z_i= 2.0
T=28.3
102
z_p= 1.5
T=32.5
103
104
C
z_i= 3.0
105
C
z_s= 0.5
106
C
z_i= 2.2
107
C
z_s= 0.2
108
C
z_i= 1.4
109
z_i= 1.6
T=43.1
110
111
z_p= 0.3
T=23.5
112
z_p= 0.3
T=21.6
113
114
z_p= 0.9
T=16.3
115
z_s= 0.1
T=25.0
116
z_s= 0.1
T=25.8
117
z_p= 1.3
T=19.2
118
z_p= 1.4
T=43.6
119
z_p= 2.1
T=40.8
120
C
z_i= 1.9
Flux Density [mJy]
Wavelength [um]

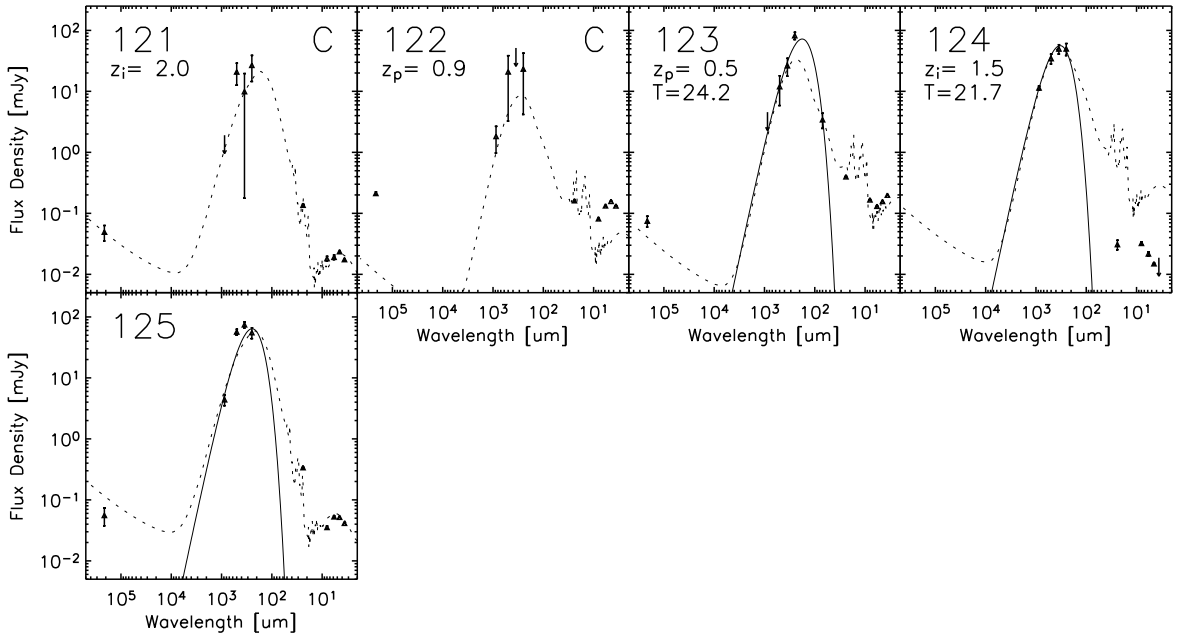
121
C
z_i= 2.0
122
C
z_p= 0.9
123
z_p= 0.5
T=24.2
124
z_i= 1.5
T=21.7
125
Flux Density [mJy]
Wavelength [um]